Stability of Planetary Rotation

Stability of Planetary Rotation

A dissertation presented
by

Ngai Ham Chan

to

The Department of Earth and Planetary Sciences

in partial fulfillment of the requirements
for the degree of

Doctor of Philosophy

in the subject of

Earth and Planetary Sciences

Harvard University
Cambridge, Massachusetts
April 2014

Thesis advisor: Professor Jerry X. Mitrovica Ngai Ham Chan

Stability of Planetary Rotation

Abstract

This thesis focuses on the long-term rotational stability of the Earth and terrestrial planets. One important class of perturbation is a reorientation of the solid planet with respect to a rotation pole that remains fixed in an inertial frame. These motions are driven by mass redistribution within or on the surface of the planet (e.g. glaciation, mantle convective flow). Long-term changes in the orientation of the rotation pole are called True Polar Wander (TPW).

In the traditional framework for computing TPW, the rotation pole is assumed to be inherently unstable since the force resisting TPW ultimately decays to zero as the planet's rotational bulge viscoelastically adjusts to any new orientation. However, there have been indications that this traditional theory significantly underestimates the stability of the pole by ignoring the impacts of an elastic lithosphere and any long-lived excess ellipticity of the planet's shape. This thesis develops linearised and non-linear rotational stability theories that incorporate both effects. These new formulations significantly extend earlier work by treating the time dependence of TPW rather than only the final (equilibrium) pole position.

The linearised theory is applied to reassess conclusions from studies of the Earth's palaeomagnetic field that have important implications for the evolution of the Earth system: (i) the rotation axis underwent cyclical displacements of amplitude $\sim 10^\circ$ with period of ~ 1 Myr in the Cretaceous; and (ii) the axis has moved less than $\sim 10^\circ$ over the last 150 Myr. It is demonstrated that the cyclical TPW inferred for the Cretaceous are physically improbable, and that the Earth's excess flattening and (possibly) elastic lithosphere were responsible for stabilising TPW over the last 100 Myr. Moreover, an application of the non-linear theory demonstrates that departures from the equilibrium orientation of the pole in response to forcings with timescale > 1 Myr are significant for Earth but negligible for Mars.

Finally, a database of ancient valley networks on Mars is used to demonstrate that the topography of these networks supports the argument that TPW deformed surface features (e.g. putative shorelines) associated with an ancient Martian ocean.

Contents

To the wandering stars.

Acknowledgments

As I WALK PAST another junction in life marked by the completion of this dissertation, I ought to credit every person I have encountered on my journey so far. Every one with whom I have interacted, whose words I have chanced to listen, and whose deeds I have observed — even those about whom I have merely learnt from others — has made me better, has improved my ways. Therefore, I should list them all here, even the names long forgotten, images long faded. Alas, practicalities always intrude into dreams, and this humble acknowledgement has to be limited in scope. But my memory and appreciation of every aforementioned 'encountered person' persists nonetheless.

I would like to thank, first and foremost, my advisor, Professor Jerry X. Mitrovica, for all the knowledge and insight he has bestowed to me throughout the years, both in science and in life. Without his guidance and advice, I would not have progressed this far nor this successfully. I must also thank Julia E. Odegova for convincing me to take, instead of 'Quantum Mechanics III' (which would have led me to a very different outcome), a course called 'Physics of the Earth' during the fourth year of my undergraduate studies. That course was taught by Jerry, then at the University of Toronto, and the rest of my academic path followed.

Another important boost for me on this path was my undergraduate research project on Blue Straggler Stars advised by Professor Natasha Ivanova, who was at that time a post-doctoral fellow at the Canadian Institute for Theoretical Astrophysics. The experience gained from working with Natasha not only prepared me well for the graduate work to come, but also gave me the confidence needed to embark on this endeavour.

I would also like to thank my group, peers, and officemates, both in Toronto and Harvard, for the continual support, care, and fun memories they gave me. Heather, Natalya, Girija, Snezana, Eric, Konstantin, John, Carling, Meredith, Veronika, Maria, Patrick, Helen, Glenn, JC, Justin, Phoebe, Jason, Jacky, Emmy, Pauline, Ken, Harriet, and Jade (in loose chronological order), you are all great, my family away from home! A few friends back home, William, Roca, and Alma, like siblings very dear to me, have also been pivotal throughout the years. Those basement rock jamming sessions, 4 A.M. park hangouts, and summer road trips, I will always remember fondly.

Deserving a very special mention is Kristian J. Bergen, who has taught me so much during these few short years at Harvard. From the abstracts of art and culture, to the practicalities of hiking and camping, to the views and stance on life, my horizons have been expanded. Thank you, Kristian, for being like the elder brother I never had.

I acknowledge my committee and the Graduate Student Council representatives: Professors Richard J. O'Connell, Sarah T. Stewart-Mukhopadhyay, Eli Tziperman, and Peter Huybers for their comments and input on my qualifying exam and dissertation defence, as well as at various points during my doctoral research. I also thank the staff at the Earth and Planetary Sciences department: Sarah, Marisa, Chenoweth, Maryorie, and Cindy have been amazing in making all the vital paperwork and machinery underlying a Ph.D. degree work flawlessly.

Last but not least, I would like to thank my parents for providing me a unique experience growing up, including supporting my classical piano training (finding me only the best teachers), sending me to the best schools (e.g. St. Paul's College, Hong Kong), and bringing me to the amazing nation of Canada. I owe much to this unique upbringing and trajectory, without which I would be a much, much lesser person. My parents are also responsible for buying me my first science book, in which there was a double-page spread showing an artist's impression of our Solar System. I remember, as a little boy, staring at that picture for long stretches of time, dreaming about visiting the planets, and memorising all their names, appearances, and orbital periods (yes, you read that correctly). There, I suppose, is where my story began.

Foreword

THE CENTRAL THEME of this thesis is True Polar Wander — long-term, secular reorientations of a planet's rotation axis with respect to its solid body or surface. An introduction to this subject is given in Chapter 1.

Chapter 2, which is included in this thesis as published in Chan et al. [2011a], outlines a new, linearised rotational stability theory for predicting the time dependence of true polar wander on a Maxwell viscoelastic body in response to mantle convective loading. The range of validity of the linearisation is established by comparing predictions with those generated from an analytic, equilibrium (i.e., infinite-time) theory. Chapter 2 compares time-dependent true polar wander computed using the traditional equilibrium stability theory adopted in most previous analyses of convection-induced true polar wander, and a new stability theory that includes two effects that have not been considered in previous geophysical analyses of long term true polar wander: (i) the so-called 'remnant rotational bulge' associated with the imperfect reorientation of the rotational bulge due to the presence of an elastic lithosphere; and (ii) a stable excess ellipticity in the planet's shape. As a first application of the new theory, Chapter 2 also explores recent inferences of rapid (order 1 Myr) true polar wander of 10°–20° during the Late Cretaceous, concluding that excursions of this amplitude over this timescale are physically implausible.

Chapter 3, which is also included as published in Chan et al. [2011b], is a companion article to Chapter 2. It uses the linear theory outlined in Chapter 2 to investigate another conclusion from the studies of the Earth's palaeomagnetic field: Palaeomagnetic records spanning the last 100 Myr indicate that the Earth's true polar wander has been confined to a range less than 6° from

its present location. This limited excursion is unexpected given that the traditional theory for the rotational stability of the Earth generally predicts that mantle convection should drive larger displacements of the pole. Chapter 3 argues that the muted true polar wander is a consequence of the stable, excess flattening of the Earth's figure driven by plate subduction and deep mantle superplumes rising beneath Africa and the Pacific. The resulting stability of the Earth's figure has important implications for our understanding of deep mantle structure and the long-term, global-scale evolution of the Earth.

In Chapter 4, we revisit the prediction, appearing in previous studies of ice-age Earth rotation [e.g. Sabadini et al., 1982], of a slow true polar wander of order of several degrees over the Plio-Pleistocene. It has been argued that this drift, and its implied change in the geographic distribution of solar insolation, was responsible for the climate transition that led the Earth System out of the ice age. We use a revised rotational stability theory that incorporates a more accurate treatment of the Earth's background ellipticity [Mitrovica et al., 2005; Cambiotti et al., 2010; Mitrovica & Wahr, 2011] to reconsider this issue. Chapter 4 demonstrates, using the revised theory, that the net displacement of the pole predicted in earlier studies disappears over timescales as long as 25 Myr. The results indicate that the cause(s) of the Earth's transition out of the ice age must be sought elsewhere.

Returning to convection-driven true polar wander, analyses of long-timescale, large-amplitude true polar wander often adopt a non-linear formulation that assumes a slow evolution of the forcing. As with the traditional linearised theory, earlier non-linear treatments of true polar wander [Ricard et al., 1993] do not take into account the effects of the remnant rotational bulge and any excess ellipticity. Chapter 5 [as published in Chan et al., 2014] extends the work of Ricard et al. [1993] to derive a nonlinear, time-dependent theory of true polar wander that incorporates stabilisation by both the remnant bulge and viscous readjustment of the rotational bulge, as well as any excess ellipticity of the planet. This theory was first used in Creveling et al. [2012] without derivation. We illustrate the new, non-linear theory using idealised surface loading scenarios applied

to models of both Earth and Mars, demonstrating that the inclusion of stabilisation by a remnant bulge or excess ellipticity reduces both the amplitude and the timescale of true polar wander relative to calculations in which this stabilisation is omitted. The calculations also indicate that in the case of loadings of timescale shorter than 1 Myr, the departure of the pole position from the orientation expected on the basis of an equilibrium (infinite-time) theory is significant for the Earth, but negligible for Mars.

Finally, Chapter 6 re-examines the connection between true polar wander and the hypothesis that an ancient ocean existed on Mars. Previous studies have investigated the plausibility of an ancient Martian ocean by examining the topography of ancient sea-level markers on the planet's surface. A previous study has argued that topographic benches, or contacts, are ancient shorelines, and that these contacts display long-wavelength topographic variations consistent with post-depositional true polar wander [Perron et al., 2007]. In contrast, a second study has argued that the topography of ancient deltaic deposits associated with an ocean on early Mars are not consistent with the true polar wander hypothesis [di Achille & Hynek, 2010]. Chapter 6 revisits this issue by examining another marker of ancient shorelines — the fluvial valley networks observed on the surface of Mars. The results provide further evidence that a true polar wander event drove significant post-depositional deflection of surface features related to an ancient Martian ocean.

They who dance are thought mad by those
who hear not the music.

Anonymous

1

Introduction to True Polar Wander

The Earth's rotation axis is subject to a broad class of perturbations that extend over timescales ranging from sub-second to billions of years. Perturbations in which the rotation axis remains fixed to the solid body and moves relative to an (inertial) observer in space, are termed nutation or (on long timescales) precession. These motions are driven by external torques acting on the equatorial bulge of the Earth, and give rise, for example, to the variations in solar insolation (associated with precession and obliquity) that define Milankovitch ice age theory.

Perturbations to the Earth's rotation axis are also characterised by a reorientation relative to the surface geography, or, as seen by an inertial observer, motion of the solid Earth relative to a stationary rotation axis. This reorientation, which changes the latitude of a fixed surface point, is a response to mass redistributions within or on the surface of the Earth, which perturb the planet's inertia tensor.

To visualise the basic physics behind TPW (i.e., conservation of angular momentum), imagine a spinning ball. If there arises any misbalance in mass, inside or outside the ball, any mass excess would tend to be 'thrown' outwards so as to move as far from the rotation axis as possible (i.e., towards the equator). To an observer standing on the ball, the rotation pole would appear to be shifting away from the 'loaded' side. On Earth, this load might consist of ice sheets, density variations related to convection in the mantle, or mass flux within the oceans and atmosphere. At relatively short timescales, cyclical reorientation of the axis is called a wobble. This includes, for example, the 14-month Chandler wobble, a periodic motion of amplitude $\sim$ 10 m of the rotation axis relative to the solid Earth, and a seasonal wobble. The combination of the two processes leads to a 7-year beating of the pole's position relative to the surface. Secular (long-term) changes in the orientation of the rotation pole relative to the surface geography are, in contrast, termed True Polar Wander (TPW). This term distinguishes these real changes in the pole's position from Apparent Polar Wander (APW) — the long-term motion of the pole inferred from palaeo-inclination measurements on a specific continent under the erroneous assumption that the position of the continent remains fixed in time.

TPW is a classic field of geophysical study (see Munk & MacDonald, 1960 for a lengthy review of early literature). Efforts to distinguish between TPW and APW, particularly in the context of the quantification of continental drift, served as an important early motivator for interest in TPW. More recently, TPW has been used as a constraint on, or target for, models of mantle convective flow [Steinberger & O'Connell, 1997; Richards et al., 1997; Greff-Lefftz, 2004; Rouby et al., 2010]. In this context, a comparison of palaeomagnetically-inferred TPW path [e.g. Besse & Courtillot, 2002] with predictions from convection models has been used to estimate the viscosity of the Earth's deep mantle [Steinberger & O'Connell, 1997] and/or the geometry of convective forcing [Richards et al., 1997].

TPW has also been identified as a potentially important control on climate. In ice-age studies, the connection to climate has been established in two different classes of study. First, geodetically

observed TPW, after correction for ongoing TPW due to Late Pleistocene glacial cycles, has been used to estimate the present-day mass balance of polar ice sheets [e.g. Mitrovica et al., 2006]. Second, traditional calculations of ice-age-induced TPW predict an irrecoverable drift of the pole, commonly called 'unidirectional TPW'; this drift has been suggested as a possible mechanism for transitioning the Earth system out of the ice-age cycles [Sabadini et al., 1982]. In addition, studies of large amplitude and rapid TPW events in deep time [Maloof et al., 2006] have been connected to dramatic perturbations in global geochemical cycles.

Outside of the Earth, TPW also provides an important lens for studying the dynamics of other terrestrial planets and moons [e.g. Melosh, 1980; Willemann, 1984; Bills & James, 1999; Schultz & Lutz, 1988; Matsuyama et al., 2006; Daradich, 2007; Hood et al., 2005; Schenk et al., 2008; Matsuyama & Nimmo, 2011; see Matsuyama et al., 2014 for a comprehensive review]. For example, in studies of Mars, TPW has been invoked to explain the topographic variations along putative shorelines [Perron et al., 2007], supporting the hypothesis that an ancient ocean existed on the surface of the red planet.

For the earth everything was simple enough. It just turned on its axis and followed its course around the sun and had nothing to worry about.

Nescio, *Amsterdam Stories*
(trans. Damion Searls)

2

The Rotational Stability of a Convecting Earth, I

Assessing Inferences of Rapid TPW in the Late Cretaceous

2.1 Introduction

The stability of the Earth's rotation vector in response to convective motions in the mantle has been, and remains, the subject of active debate within the geophysical and geological literature. In general, predictions of the convection-induced reorientation of the rotation vector relative to the surface geography, or true polar wander (henceforth TPW) [e.g. Steinberger & O'Connell, 1997] have been based on a canonical equilibrium stability theory outlined by Gold [1955], and summarised, schematically, in Figure 2.1. Consider an Earth model in steady rotation for a time long enough that all viscous stresses have relaxed to the imposed centrifugal potential (Figure 2.1A1); in this case, the equilibrium 'rotational bulge' or ellipticity of the planet will have a so-called

hydrostatic form [Nakiboglu, 1982]. If the Earth is then subject to a positive load, polar motion would act to move the load towards the equator (Figure 2.1A2); the background bulge of the planet will initially resist such an excursion. However, the Earth will deform in response to the perturbed centrifugal potential, and the bulge will eventually reorient perfectly to the new rotation vector (Figure 2.1A3); this will free the pole to wander further from the load (Figure 2.1A4). The process will continue in infinitesimal steps until the load has migrated to the equator (Figure 2.1A5) and TPW will cease. In this theory, the rotation vector is ultimately unstable in the presence of an applied load since the bulge does not provide any long-term resistance to TPW [Gold, 1955; Goldreich & Toomre, 1969]. The Earth, in this scenario, is said to have no permanent memory of its orientation. (Note that there is an assumption in this classic description that the applied load will never reach a state of isostatic compensation, and will thus continuously act as a driving force on the pole.)

The physical basis for this description of rotational stability has been highlighted by two equally canonical schematic images. For example, the continual effort by the bulge to keep up with the rotation pole is illustrated by Gold's famous donkey and carrot analogy, whereby a donkey (representing the bulge) moves inexorably towards a carrot (the pole) that is connected to the donkey by an overhead wire that dangles frustratingly in his line of sight [Gold, 1955]. A key element of the Gold stability theory is that any load, no matter what size, will drive a TPW that eventually moves the load to the equator. This key aspect of the theory was discussed by Goldreich & Toomre [1969], who characterised the load by a small beetle, or a set of such beetles. It is important to emphasise that the 'equilibrium' stability theory of Gold yields a prediction of the final orientation of the pole and says nothing about the timescale required to reach the equilibrium position.

In mathematical terms, the orientation of the rotation pole in the Gold stability theory is given by the direction of the principal axis of the non-hydrostatic inertia tensor. In this regard, under the assumption that the timescale of convection is much longer than the timescale of bulge adjustment, the TPW path in convection studies has generally been computed by diagonalising the inertia ten-

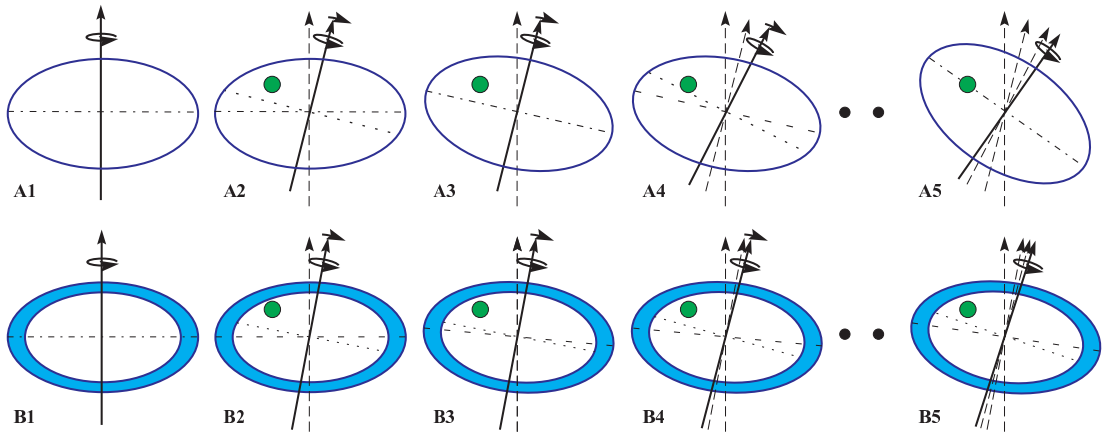

Figure 2.1: Schematic illustration of the physics of TPW as treated by (A) Gold [1955] and (B) Willemann [1984] and Matsuyama et al. [2006]. The green disk represents a positive internal density load, the blue outer shell (second row) is an elastic lithosphere, the solid arrow (with spin and TPW directions specified at the head and tip, respectively) is the rotation vector, and the long-dashed arrows are previous rotation vectors within the same series. On each frame, a dashed line denotes the plane of the rotational bulge, while the dotted line is the rotational equator. When these two lines are aligned (A1, A3, A5, B1), the bulge is perfectly relaxed. (A) TPW on an Earth model in which the rotational bulge will ultimately adjust completely to load-induced TPW, and the load will ultimately migrate to the equator (A5). (B) TPW when an initial, hydrostatic form (B1) includes an unstressed elastic lithosphere. In this case, the elastic shell will permanently resist excursions of the rotation pole and the final state (B5), in which the load has not reached the equator, will represent a balance between this resistance and the load-induced impact on the pole.

sor perturbation at each step in the simulation. This perturbation takes into account the advection of density heterogeneities and deformation of all boundaries associated with the mantle flow.

A small number of studies have extended the rotational stability theory described above to consider the time history of TPW [e.g. Ricard et al., 1993; Richards et al., 1997, 1999; Tsai & Stevenson, 2007; Schaber et al., 2009]. Tsai & Stevenson [2007], for example, used scaling arguments based on energy considerations to derive analytic expressions for the TPW of a Maxwell body with a single relaxation time. Their study highlights several important concepts that will also be apparent in the results we describe within this paper. For example, a central goal of their analysis was to quantify the 'speed limit' of TPW — how fast can the pole go in response to convective forcing?

In this regard, it is important to point out that there is, of course, no minimum speed — a load the size of the beetle may eventually get to the equator using the theory of Gold [1955], but it may take longer than the age of the Earth to do it. Tsai & Stevenson [2007] also introduced the concept of a TPW filter. In particular, they argued that TPW will most efficiently be excited by the longest timescales of the forcing, and the transition or cut-off within this low (frequency) pass filter will be governed, in large part, by the mantle viscosity. Figure 1 in Tsai & Stevenson [2007] is a particularly elegant demonstration of this physics.

Tsai & Stevenson [2007] used their model to conclude that the maximum rate of TPW is 2.4 deg Myr^{-1}, though they emphasise that this rate is sustainable for only a short period of time. They concluded that this rate appears to be too high relative to the geological record, at least in the post-Jurassic period, and they provided a suite of possible explanations for this discrepancy (see p.9 of their paper). One of these explanations is that the lower mantle viscosity may be higher than they considered; an increase in this viscosity would act to slow the convective driving force for TPW. An earlier convective simulation of polar motion [Steinberger & O'Connell, 1997], based on the rotational stability theory of Gold [1955], also required a high deep mantle viscosity to achieve TPW rates consistent with palaeomagnetic data over the last 50 Myr. Tsai & Stevenson [2007] also noted that their TPW speed limit was too low to allow the 90° shift in $\sim$ 40 Myr inferred for the early Cambrian by Kirschvink et al. [1997]. They concluded that the polar motion postulated by Kirschvink et al. [1997] was dynamically implausible.

Tsai & Stevenson [2007] did not include the possible stabilising effect of an elastic, or even high-viscosity viscoelastic lithosphere. They suggested that broken plates do not provide any resistance to changes in the centrifugal potential (since adjustments would, they argued, be taken up along plate boundaries), and that the timescale associated with the elastic adjustment of the lithosphere would be short relative to the characteristic timescale of the convective forcing. In regard to the first argument, the centrifugal force will act within the entire body of the planet, and will therefore cause flexure, and resistance to TPW, throughout the plate — not only at plate bound-

aries. It is certainly true that the effective elastic thickness of a broken plate in response to a body force with a spherical harmonic degree two potential (i.e, the centrifugal force) will be smaller than the elastic thickness of an unbroken shell, but it will not be zero. This will be particularly true in considering TPW over timescales of order several Myr or less; for instance, modelling of ice age adjustments clearly requires the incorporation of a strong lithosphere [e.g., Nakada & Lambeck, 1989]. In regard to the second argument, while the elastic response of the lithosphere will certainly have a timescale that is short relative to the convective forcing, the presence of such a lithosphere — even a broken one — will nonetheless have a potentially profound impact on rotational stability. This impact is illustrated in Figure 2.1B, which extends the stability arguments in Figure 2.1A [Gold, 1955] to include an elastic lithospheric shell.

The equilibrium rotational stability of dynamic, terrestrial planets with elastic lithospheres was first treated by Willemann [1984], and most recently by Matsuyama et al. [2006] and Daradich et al. [2008], who corrected minor errors in the original description. Consider the model planet in Figure 2.1B1, which is characterised by a hydrostatic background oblateness (i.e., the flattening in Figure 2.1B1 is identical to that in Figure 2.1A1). Let us assume the planet has an unstressed elastic lithosphere, as denoted by the light blue shell. An unstressed shell may have developed, for example, through secular cooling of the planet, or by very slow viscous relaxation within the lithosphere. If this planet is subsequently loaded (Figure 2.1B2), the pole would (as in Figure 2.1A2) move away from the load and the bulge will resist this motion. However, the important distinction between this case and Figure 2.1A is that the adjustment of the bulge in response to TPW cannot perfectly reorient the bulge (i.e, the elastic shell cannot deform to be symmetric about the new pole position; Figure 2.1B3). The deviation from scenario 2.1A arises because elastic stresses that develop in the (initially unstressed) lithosphere in response to the perturbed centrifugal potential will impose a permanent restoring force on the rotation vector. That is, in this case, the system will have a memory of its initial state, and the ultimate result is that the final equilibrium pole position (Figure 2.1B5) will reflect a balance between loading and what Willemann [1984] and Matsuyama

et al. [2006] called the 'remnant rotational bulge'. Most notably, TPW will cease before the load makes it to the equator.

The stabilisation associated with the lithosphere is significant. As an example, taken from the results of Matsuyama et al. [2006], consider a load with a pre-compensated size that is 10% of the size of the equatorial bulge, where 'size' is measured by the associated geopotential perturbation at spherical harmonic degree two. If this load is placed at a colatitude of 40°, then the Gold [1955] theory predicts a total TPW of 50° (since the load will ultimately reach the equator). In contrast, if a lithosphere of thickness of 50 km is assumed, then the extended equilibrium stability theory summarised in Figure 2.1B ultimately yields a TPW of only 4°. Two caveats. First, if the 50 km lithosphere is broken, then the effective elastic thickness will be smaller than this value, but it will not be zero; it is important, in this regard, to note that the stabilisation associated with the remnant rotational bulge is relatively insensitive to the adopted lithospheric thickness [Willemann, 1984; Matsuyama et al., 2006]. For example, if we repeat the calculation for an elastic lithospheric thickness of 25 km, the total TPW predicted by Matsuyama et al. [2006] would still be less than 5°. Second, if the lithosphere were treated as viscoelastic rather than elastic, then the stabilisation associated with the remnant bulge would not be permanent. Rather, it would only stabilise the rotation pole in response to forcings with timescales less than the relaxation time of the high viscosity lithosphere. In this regard, it would act, as in the terminology of Tsai & Stevenson [2007], as a low pass TPW filter. In any event, the rather dramatic damping of TPW associated with the presence of an elastic or high viscosity lithosphere suggests that the remnant bulge physics should be incorporated into the rotational stability theory.

In this paper we outline a linearised stability theory for the rotation of Earth models with a 1-D (depth-varying) linear viscoelastic rheology. The theory extends the approach described by Tsai & Stevenson [2007] in a number of ways. First, it admits as many relaxation times (or normal modes) as exist in the impulse response of the Earth model. Second, the 1-D depth variation accommodates an elastic or finite viscosity lithosphere, and thus incorporates the possibility of stabilization

from the remnant rotational bulge. The theory also allows for the possibility of an excess ellipticity in the Earth's form which might arise from a number of processes acting on timescales much longer than the convective flow considered in this manuscript (see below). The theory is based on a linearised version of the time domain Euler equation, and it follows recent developments in the theoretical treatment of ice age Earth rotation [Mitrovica et al., 2005]. The linearisation assumes 'small' motions of the rotation pole; however, we present results that indicate that the TPW can reach 20°–30° before errors exceed order 5–10%. And thus, within this range of TPW we explore the full complexity of the time dependence of the TPW.

To investigate the time dependence of TPW, we need to specify a time history of the convective forcing (i.e., a time history of perturbations to the inertia tensor). Tsai & Stevenson [2007] considered sinusoidal variations in the TPW forcing, in contrast to earlier studies that tended to explore rotational stability in response to a step-wise change in the inertia tensor [e.g., Munk & MacDonald, 1960]. The time variation in the inertia tensor driven by mantle flow almost certainly includes both classes of forcing — indeed, Goldreich & Toomre [1969] demonstrated that the timescale for inertia tensor changes can be short if there are multiple contributors to the forcing — and thus our analysis will consider both a sinusoidal time history and a history involving a gradual ramp-up or net shift in the load.

As a first application of our theory, we will investigate the plausibility, from the perspective of rotational dynamics, of evidence for a rapid TPW event in the Late Cretaceous [Sager & Koppers, 2000]. Specifically, Sager & Koppers [2000] inferred 16°–21° of TPW in 2–5 Myr beginning at $\sim$ 85 Ma on the basis of palaeomagnetic data from Pacific seamounts [see Cottrell & Tarduno, 2000 for a critique of the Sager & Koppers, 2000 data set and methodology]. More recently, there has also been a preliminary suggestion, based on magnetostratigraphic data, of rapid (order 1 Myr), quasi-cyclical 10°–20° TPW during the Late Cretaceous [Thissen et al., 2010]. With the expectation that such high resolution analyses will become more common, the overarching goal of our study will be to establish bounds on the amplitude of TPW and elucidate the physics con-

trolling rapid motions of the rotation pole — whether these motions are quasi-cyclical or unidirectional. The linearised theory we develop is particularly well suited to such problems, since the net polar wander during such events is well within the range of validity we establish for the linearisation. Moreover, the response of the Earth to such rapid forcing is certainly characterised by some degree of elastic strength in the crust-lithosphere system, and hence the remnant bulge physics may play an important role.

We begin with a summary of the linearised theory of rotational stability.

2.2 A Linearised Theory of Earth Rotation

In this section, we outline a linearised form of the equation governing conservation of angular momentum that is derived from recent treatments within the literature of ice age rotation [Mitrovica et al., 2005].

In the case where no external torques act on the system, the Euler Equation in an Earth-fixed reference frame is

$$0 = J_{ij}(t)\dot{w}_j(t) + \dot{J}_{ij}(t)w_j(t) + \varepsilon_{ijk}w_j(t)J_{kl}(t)w_l(t), \tag{2.1}$$

where $\mathbf{J}$ denotes the inertia tensor, w_i are components of angular velocity, ε_{ijk} is the Levi-Civita tensor, and the dot superscript denotes a time derivative.

If we assume that the inertia tensor is diagonal in the unperturbed state, with elements given by A, A, and C, and, in the same state, the angular velocity vector is given by $\mathbf{\Omega} = (0,\ 0,\ \Omega)$, then a perturbation from this initial state can be written as

$$\begin{aligned} w_i(t) &= \Omega[\delta_{i3} + m_i(t)] \\ J_{11}(t) &= A + I_{11}(t) \\ J_{22}(t) &= A + I_{22}(t) \\ J_{33}(t) &= C + I_{33}(t) \\ J_{ij}(t) &= I_{ij}(t) \ \text{ for } i \neq j \end{aligned} \quad , \tag{2.2}$$

where we assume that all perturbations I_{ij} are smaller than either of the principal moments in the unperturbed system (A, C), and that $m_i \ll 1$.

There are three contributions to the inertia tensor perturbations. These are: (1) the mantle or surface mass anomalies; (2) the deformation induced by the mass anomalies; and (3) the deformation in response to the perturbed centrifugal potential. In each case, a mapping exists between the perturbation in the inertia tensor and the associated perturbation in the geopotential at spherical harmonic degree 2 [e.g., Matsuyama et al., 2006]. We adopt a Maxwell viscoelastic rheology in the calculation of these geopotential perturbations and the latter two contributions may therefore be computed using viscoelastic Love number theory [Peltier, 1974; Wu, 1978; Tromp & Mitrovica, 1999].

In the time (t) domain, the load and tidal (or tidal-effective) k Love numbers at spherical harmonic degree two are, respectively, given by

$$\begin{aligned} k_2^L(LT, \nu, t) &= k_2^{L,E}\delta(t) + \sum_{j=1}^{J} r_j' e^{-s_j t} \\ k_2^T(LT, \nu, t) &= k_2^{T,E}\delta(t) + \sum_{j=1}^{J} r_j'' e^{-s_j t} \end{aligned} \quad . \tag{2.3}$$

The Love numbers are comprised of instantaneous elastic (first term on the right-hand side) and non-elastic (second term) components, where the latter are comprised of a set of J normal modes of viscoelastic decay. The two Love numbers share the same set of inverse decay times, s_j, but have distinct modal amplitudes. The viscoelastic Earth model structure is embedded within each of the parameters that define these Love numbers. In this regard, on the left-hand side of these equations, we make the dependence on the elastic thickness of the lithosphere, LT, and on the radial viscosity profile, ν, explicit. It will be useful to write these time domain expressions in terms

of their Laplace-transform, s-domain forms. These are

$$\begin{aligned} k_2^L(LT, \nu, s) &= k_2^{L,E} + \sum_{j=1}^{J} \frac{r_j'}{s + s_j} \\ k_2^T(LT, \nu, s) &= k_2^{T,E} + \sum_{j=1}^{J} \frac{r_j''}{s + s_j} \end{aligned} \quad . \tag{2.4}$$

Using equation (2.2) in (2.1), and computing the necessary inertia tensor perturbations using the viscoelastic Love numbers, yields, after some algebra, the linearised Euler Equation (i.e., the Liouville Equation) [Mitrovica et al., 2005]

$$\mathbf{m}(t) = \frac{\mathbf{I}^L(t) + k_2^L(LT, \nu, t) * \mathbf{I}^L(t)}{(C - A)} + \frac{k_2^T(LT, \nu, t)}{k_f} * \mathbf{m}(t) \ , \tag{2.5}$$

where $*$ denotes a time-convolution, $\mathbf{I}^L(t) = I_{13}^L(t) + i\, I_{23}^L(t)$, and $\mathbf{m}(t) = m_1(t) + i\, m_2(t)$. The observed fluid Love number, k_f, is

$$k_f = \frac{3G}{a^5 \Omega^2} (C - A) \ , \tag{2.6}$$

in which a and Ω are the radius and rotation rate of the Earth, and G is the universal gravitational constant. The term $\mathbf{I}^L(t)$ in equation (2.5) represents the perturbation to the inertia tensor associated with the direct effect of the load (i.e., the first of the contributions to the total inertia tensor perturbation discussed above).

The value of k_f governs the background oblateness of the Earth model upon which the perturbations associated with the loading are superimposed. In practise, we can separate this number into hydrostatic and non-hydrostatic (k_{nh}) contributions, where the former can be computed using viscoelastic Love number theory. Specifically, this separation can be written as

$$k_f = k_2^T(LT = 0, s = 0) + k_{nh} \ , \tag{2.7}$$

where the hydrostatic form has been replaced by the degree-2 k fluid Love number for a model with no elastic lithosphere at the limit of infinite time ($s = 0$); in this case, there are no purely elastic regions and all viscous regions of the model have fully relaxed — hence the dependence on ν disappears.

Applying this decomposition to equation (2.5) yields

$$\mathbf{m}(t) = \frac{\mathbf{I}^L(t) + k_2^L(LT, \nu, t) * \mathbf{I}^L(t)}{(C-A)} + \frac{k_2^T(LT, \nu, t)}{k_2^T(LT = 0, s = 0) + k_{nh}} * \mathbf{m}(t) \, . \tag{2.8}$$

In the s-domain, this equation becomes

$$\mathbf{m}(s) = \frac{\mathbf{I}^L(s)}{C-A} \cdot \frac{1 + k_2^L(LT, \nu, s)}{1 - \frac{k_2^T(LT, \nu, s)}{k_2^T(LT=0, s=0) + k_{nh}}} \, . \tag{2.9}$$

We can use this last equation to revisit the physics of both scenarios shown in Figure 2.1. In the rotational stability theory of Gold [1955], the background form is purely hydrostatic (i.e, $k_{nh} = 0$), and the model has no elastic lithosphere (i.e., $LT = 0$). If we furthermore assume that the load is never isostatically compensated (as Gold did), then the term in the numerator, $1 + k_2^L(LT = 0, \nu, s)$ is assumed to be non-zero in the limit of infinite time (or $s = 0$). However, in the same time limit, the denominator, $1 - k_2^T(LT, \nu, s)/[k_2^T(LT = 0, s = 0) + k_{nh}]$ will go to zero, and the linearised solution for $\mathbf{m}(s \to 0)$ becomes unbounded. Of course, in a non-linear theory, this instability continues until the load reaches the equator.

In the scenario shown in Figure 2.1B (where we also assume $k_{nh} = 0$), the Earth model has an elastic lithosphere. In this case, neither the numerator nor the denominator in equation (2.9) will go to zero at infinite time, and the system remains stable. In this scenario, the final position of the load is governed by a balance between the force driving polar motion, which is proportional to the term $1 + k_2^L(LT, \nu, s)$ in the numerator, and the resistance associated with the bulge, the term $1 - k_2^T(LT, \nu, s)/k_2^T(LT = 0, s = 0)$.

It is clear from these examples that the stability of the system is ultimately governed by the ratio $k_2^T(LT, \nu, s)/[k_2^T(LT = 0, s = 0) + k_{nh}]$ that appears in the denominator of equation (2.9). In the absence of a non-hydrostatic contribution to the background bulge, this means that the system will remain stable as long as $k_2^T(LT, \nu, s) \neq k_2^T(LT = 0, s = 0)$; that is, the system will remain stable as long as the Love number that governs the response of the model to the changing centrifugal potential, $k_2^T(LT, \nu, s)$, does not take on a hydrostatic form. When the lithosphere has a purely elastic component, i.e., when $LT \neq 0$, this stability requirement is guaranteed, and the difference between $k_2^T(LT, s = 0)$ and $k_2^T(LT = 0, s = 0)$ represents the remnant bulge stabilisation described in the § 2.1 [Willemann, 1984; Matsuyama et al., 2006]. Notice that if the Earth model has a high viscosity viscoelastic lithosphere, then the ratio $k_2^T(LT, s = 0)/k_2^T(LT = 0, s = 0)$ will approach 1.0, and the system (with $k_{nh} = 0$) will become unstable (as in Figure 2.1A) for times longer than the decay time of the viscoelastic lithosphere. In contrast, for times less than this characteristic relaxation time, the system will behave according to Figure 2.1B. In other words, once the viscoelastic lithosphere relaxes, the bulge is free to adjust perfectly to the new position of the rotation vector, and the system loses memory of its original rotational state. This high-viscosity lithosphere case thus serves as a bridge between the stable state described in the theory of Willemann [1984] and Matsuyama et al. [2006], and the unstable state described by Gold [1955].

Finally, we note that any excess ellipticity will guarantee that the rotation remains stable, regardless of the relationship between $k_2^T(LT, \nu, s)$ and $k_2^T(LT = 0, s = 0)$ as $s \to 0$. Thus, an excess ellipticity will contribute a stabilisation to the rotation. The Earth's current background form has an excess ellipticity equal to about 1% of the hydrostatic value [Nakiboglu, 1982], and this extra flattening is generally taken to be due to upwelling megaplumes below southern Africa and the Pacific [e.g. Lithgow-Bertelloni & Silver, 1998]. This raises a subtle point. If we were to use our theory to consider short timescale TPW (i.e., TPW of timescale 1 Myr or less) driven by mantle convection, then, since these megaplumes are unlikely to adjust non-negligibly over this time period, it would be appropriate to retain the term k_{nh} as it appears in the Liouville Equation (2.8).

The convection induced changes in the inertia tensor over such timescales would thus be considered perturbations on the long-wavelength form associated with the more stable megaplumes. However, for long timescales, the excess ellipticity term should be interpreted as being part of the load-induced perturbation in the inertia tensor (i.e., part of $1 + k_2^L(LT, \nu, s)$), and it would not be appropriate to retain it in the Liouville Equation (2.8). In this case, we would set $k_{nh} = 0$ in this equation. The latter would also be the case for a realistic simulation of mantle convection that captured both the short and long-term perturbations to the inertia tensor.

2.2.1 Establishing a Range of Validity for the Liouville Equation

The question arises: how much TPW can occur before the linearisation adopted to derive the Liouville Equation (2.8) breaks down? To quantify this issue, we will consider the final state of the scenario shown in Figure 2.1B5, where a surface mass load is applied and retained for all time on a rotating Earth model with a hydrostatic form and an initially unstressed elastic lithosphere. In particular, we will compare the $t \to \infty$ response predicted using the Liouville Equation (2.8) (with k_{nh} set to 0) with the result based on the equilibrium, non-linear theory described by Matsuyama et al. [2006], following Willemann [1984]. We begin with the latter.

Let us assume that an axisymmetric disk load is placed on the Greenwich meridian at some colatitude θ_L at time $t = 0$. Let us furthermore assume that the load can be represented in terms of a spherical harmonic decomposition

$$L(\theta, \psi, t) = H(t) \sum_{\ell=0}^{\infty} \sum_{m=-\ell}^{\ell} L_{\ell m} Y_{\ell m}(\theta, \psi) \,, \tag{2.10}$$

where $H(t)$ is the Heaviside function, θ is the colatitude, ψ is the east longitude, and ℓ and m are the spherical harmonic degree and order, respectively. We assume that the spherical harmonic

basis functions are normalised such that

$$\int_S Y^{\dagger}_{\ell' m'}(\theta, \psi) Y_{\ell m}(\theta, \psi) dS = 4\pi \delta_{\ell \ell'} \delta_{m m'} \ , \tag{2.11}$$

where † denotes a complex conjugation, and S represents an integration over the unit sphere.

If the same axisymmetric load was rotated to be centred on the north pole, then the spherical harmonic coefficients of this load (which we will denote by a superscript prime) would be related to the original harmonic components by

$$L_{2m} = L'_{20} \frac{Y^{\dagger}_{2m}(\theta_L, \psi_L = 0)}{\sqrt{5}} \ . \tag{2.12}$$

The spherical harmonic $\ell = 2, m = 0$ coefficient of the geopotential due to the direct gravitational effect of the surface mass (polar) load is given by [Matsuyama et al., 2006]

$$G^L_{20} = \frac{4\pi a^3 g}{5M} L'_{20} \ , \tag{2.13}$$

while the same harmonic coefficient of the geopotential associated with the background hydrostatic form of the model Earth is

$$G^H_{20} = -\frac{1}{3\sqrt{5}} a^2 \Omega^2 k^T_2 (LT = 0, s = 0) \ . \tag{2.14}$$

Following Willemann [1984] and Matsuyama et al. [2006], we thus define a normalised load size, Q', by the ratio

$$Q' = -\frac{G^L_{20}}{G^H_{20}} = \frac{\frac{4\pi a^3 g}{5M} L'_{20}}{\frac{1}{3\sqrt{5}} a^2 \Omega^2 k^T_2 (LT = 0, s = 0)} \ . \tag{2.15}$$

With this definition in hand, the TPW angle δ for a load of normalised size Q' placed at a colat-

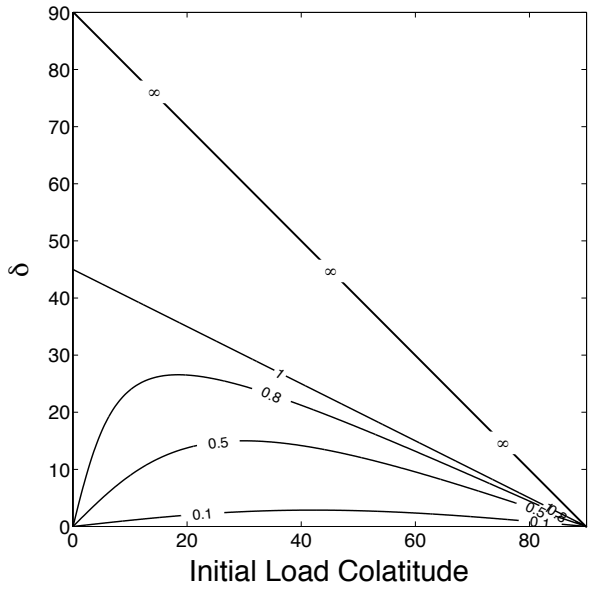

Figure 2.2: Predictions of TPW angle (δ) versus the initial colatitude of the loading for a suite of different $Q'\alpha$, as labelled on the contours. The calculations are based on equation (2.16) derived using the equilibrium, non-linear theory of Matsuyama et al. [2006], after Willemann [1984].

itude of θ_L is given by [Matsuyama et al., 2006]

$$\delta = \frac{1}{2}\arctan\left[\frac{Q'\alpha\sin(2\theta_L)}{1-Q'\alpha\cos(2\theta_L)}\right], \tag{2.16}$$

where α is given by

$$\alpha = \frac{1+k_2^L(LT, s=0)}{1-\frac{k_2^T(LT,s=0)}{k_2^T(LT=0,s=0)}}. \tag{2.17}$$

The parameter α is a function of the fluid ($s = 0$) state of the Earth model. For realistic Earth models, α is of order 1, and is only weakly sensitive to the choice of LT.

In Figure 2.2, we plot the TPW angle δ as a function of the initial load colatitude for 5 different values of $Q'\alpha$, ranging from 0.1 to ∞. The physics of this solution space is discussed in detail in Matsuyama et al. [2006]. For loads of very large size, the TPW angle is $90^\circ - \theta_L$, and thus the final load position is always the equator. In this case, the load is so large that, despite the resistance

of the remnant rotational bulge, the reorientation is governed by the stability theory described by Gold [1955] (Figure 2.1A). However, for loads equal to 10% of the size of the bulge, the TPW angle is less than a few degrees, no matter where the load is initially placed.

Next, we solve for the TPW using the Liouville equation (2.8). In this case, the $I^L_{13}(t)$ inertia perturbation due to the load can be written as $I^L_{13}H(t)$. Moreover, with no loss of generality, we can express the time dependence in the m_1 component of the perturbation in the rotation vector as a series of N Heaviside load increments

$$m_1(t) = \sum_{n=0}^{N} \delta m_1^n H(t - t_n) \, . \tag{2.18}$$

Applying this expression in (2.8) and performing the time convolution yields, using equation (2.3),

$$\left(1 - \frac{k_2^{T,E}}{k_2^T(LT = 0, s = 0)}\right) \sum_{n=0}^{N} \delta m_1^n H(t - t_n) = \frac{{I_{13}}^L}{C - A} H(t) \left[1 + k_2^{L,E} + \sum_{j=1}^{J} \frac{r'_j}{s_j} \left(1 - e^{-s_j t}\right)\right]$$
$$+ \frac{1}{k_2^T(LT = 0, s = 0)} \sum_{n=0}^{N} \delta m_1^n H(t - t_n) \sum_{j=1}^{J} \frac{r''_j}{s_j} \left(1 - e^{-s_j (t - t_n)}\right) \, . \tag{2.19}$$

Taking the $t \to \infty$ limit in this equation, and using equation (2.4), yields, after some simplification

$$m_1(t = \infty) = \frac{I^L_{13}}{C - A} \frac{1 + k_2^L(LT, s = 0)}{1 - \frac{k_2^T(LT, s=0)}{k_2^T(LT=0, s=0)}} = \frac{I^L_{13}}{C - A} \alpha \, . \tag{2.20}$$

We could have arrived at the same result by using the $s \to 0$ limit in equation (2.9).

One can show, using the definition in equation (2.15) that

$$I_{13} = -\frac{1}{2}(C - A) Q' \sin(2\theta_L). \tag{2.21}$$

Using this expression in equation (2.20) yields

$$m_1(t = \infty) = -\frac{1}{2} Q' \alpha \sin(2\theta_L), \tag{2.22}$$

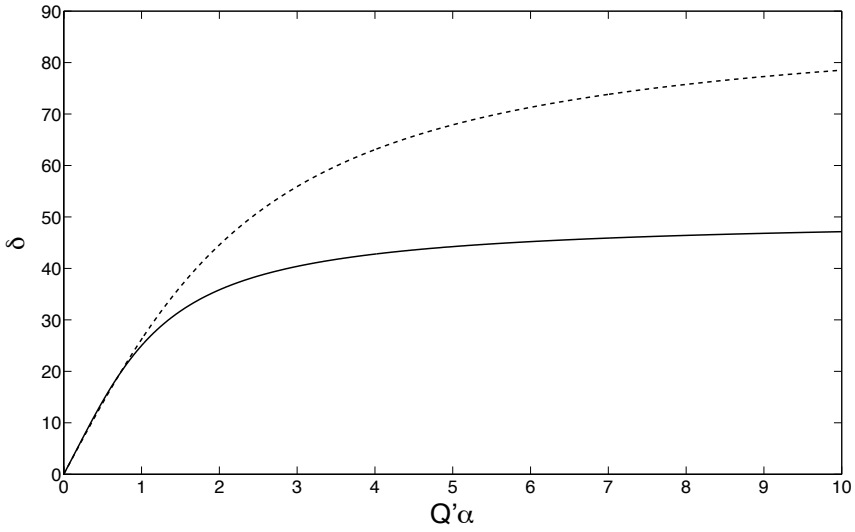

Figure 2.3: Predictions of the TPW angle (δ) versus $Q'\alpha$ generated using the (solid line) equilibrium, non-linear theory of Matsuyama et al. [2006], following Willemann [1984] (equation 2.16) and the (dashed line) linearised theory (equation 2.23).

and therefore, the predicted amplitude of TPW based on the linearised theory is

$$\delta = \tan^{-1}\left(\frac{1}{2}Q'\alpha\sin(2\theta_L)\right). \tag{2.23}$$

We now have two expressions for the TPW associated with the scenario in Figure 2.1B: equation (2.23), based on the asymptotic value of our linearised rotation theory in response to a Heaviside loading; and a value computed using an equilibrium (i.e., no time-dependence) non-linear stability theory, equation (2.16). In both cases, the required Earth model structure in the fluid limit is embedded in the parameter α (equation 2.17). A comparison of the results generated using the linearised and non-linear theories will provide a quantitative measure of the accuracy of the former in predictions of TPW.

As an illustration of this accuracy, Figure 2.3 shows predictions of TPW versus $Q'\alpha$ predicted using the non-linear (solid line) and the linearised (dashed line) stability theories for a load placed

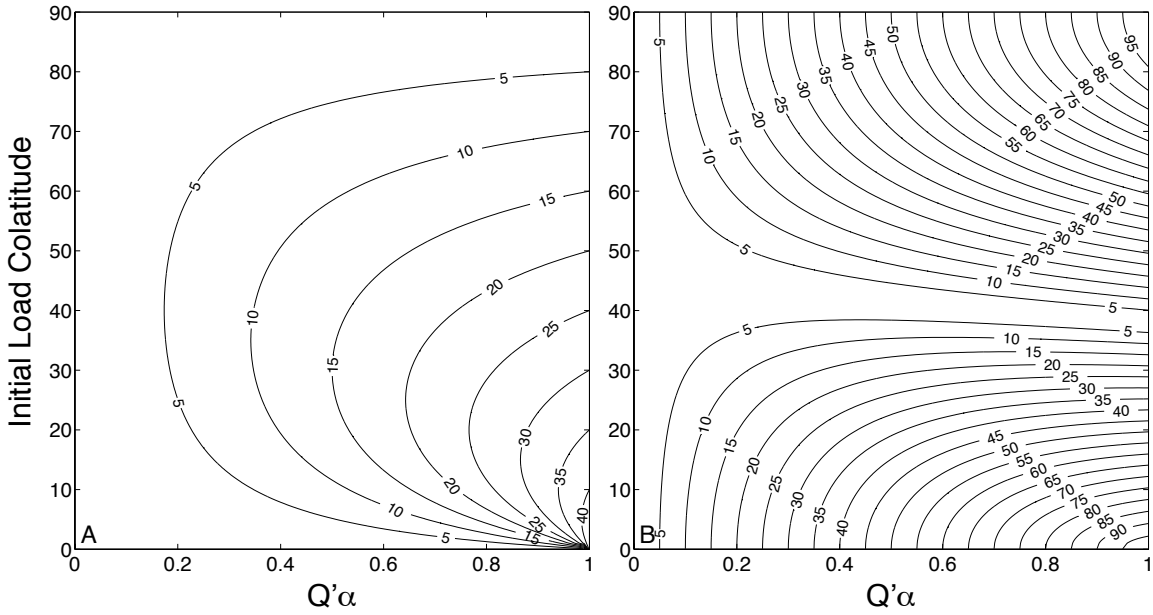

Figure 2.4: (A) Predictions of the TPW angle (δ), as labelled on the contours, in a solution space that varies the initial colatitude of the load, θ_L, and $Q'\alpha$. Calculations are based on equation (2.23). (B) Percent error in the predictions generated using the linearised rotational stability theory (frame A) computed via a comparison with the expression (2.16).

on the Earth at an initial colatitude of 40°. At $\delta = 20°$ ($Q'\alpha \sim 1$), the prediction based on the linearised theory has an error of less than 5%. This error increases to about 10% for a TPW of 30° ($Q'\alpha \sim 1.5$). The accuracy of the linearised theory degrades monotonically for higher $Q'\alpha$ values.

We next generalise this analysis to consider a range of θ_L values in Figure 2.4. Figure 2.4A shows contours of TPW (δ) for $0° < \theta_L < 90°$ and $Q'\alpha < 1$, predicted using the linearised theory. Figure 2.4B plots the associated error in these predictions. It is clear from the figure that the accuracy of the linearised theory is greatest when the load is placed at mid-latitudes. For $40° < \theta_L < 50°$, predictions of $\delta \sim 20°$ that are obtained for $Q'\alpha \sim 1$ have an error less than 30%. In reference to Figure 2.2, we note that this preferred range of θ_L samples the region where $\partial(\delta)/\partial\theta_L$ is smallest, at least for $Q'\alpha < 0.1$.

We conclude from this section that by applying a load to the Earth model at mid-latitudes, the

linearised stability theory will be accurate to order 10% for TPW predictions up to 20°. This will serve as a guideline for the numerical tests described in the next section.

2.3 Results and Discussion

In this section we turn to an examination of the rotational stability of the Earth in response to a time varying perturbation in its inertia tensor. The term $\mathbf{I}^L(t) + k_2^L(LT, \nu, t) * \mathbf{I}^L(t)$ in the governing equation (2.8) incorporates both the load and its isostatic compensation. In considering loads associated with mantle convection, we will impose this total 'effective' load, and we can thus rewrite this equation as

$$\mathbf{m}(t) = \frac{\mathbf{I}_{\mathit{eff}}(t)}{(C-A)} + \frac{k_2^T(LT, \nu, t)}{k_2^T(LT=0, s=0) + k_{nh}} * \mathbf{m}(t). \tag{2.24}$$

As discussed above, this form incorporates the stabilising influence of the remnant rotational bulge and, for $k_{nh} \neq 0$, any excess ellipticity in the Earth's form. As discussed below equation (2.9), the special case of time-domain equation (2.8) consistent with the physics first described by Gold [1955] is obtained by setting k_{nh} to 0, and using an Earth model with no purely elastic component of the lithosphere:

$$\mathbf{m}(t) = \frac{\mathbf{I}_{\mathit{eff}}(t)}{(C-A)} + \frac{k_2^T(LT=0, \nu, t)}{k_2^T(LT=0, s=0)} * \mathbf{m}(t). \tag{2.25}$$

In this case, an uncompensated load will ultimately reach the equator, as in the scenario depicted in Figure 2.1A, although in our linearised theory this instability will be manifest in an unbounded TPW. In the following discussion we will use the terms 'new theory' and 'traditional theory' when referring to solutions based on equations (2.24) and (2.25), respectively. We emphasise, however, that our equation (2.25) provides the time-dependence of the system in Figure 2.1A, in contrast to the usual equilibrium form of the traditional theory [Gold, 1955] adopted in most previous mantle convection studies, which specifies only the final state of the pole.

The Maxwell viscoelastic Earth we adopt is spherically symmetric and self-gravitating. The

elastic and density structure of the model is given by the seismically inferred model Preliminary Reference Earth Model [Dziewonski & Anderson, 1981]. The viscosity structure is discretised into three layers: an elastic (i.e., infinite viscosity) lithosphere of thickness LT, an upper mantle viscosity set to 10^{21} Pa s, and a lower mantle viscosity that will vary in the simulations.

Finally, we need to prescribe the effective inertia tensor perturbation or, using equation (2.21), the normalised load size Q' and load colatitude θ_L. Following the arguments of the last section, we will adopt $\theta_L = 40^\circ$ to optimise the accuracy of the linearised theory, and this yields

$$Q' = \frac{2\bar{\mathbf{I}}_{eff}}{(C-A)\sin 80^\circ}, \tag{2.26}$$

where $\bar{\mathbf{I}}_{eff}$ is the maximum value in the time variation of $\mathbf{I}_{eff}(t)$.

What is an appropriate value of Q'? That is, what is the expected normalised load associated with mantle convection over the timescales of interest to our study ($\sim$ 1 Myr)? To estimate this load, we begin by considering the total perturbation in the Earth's present-day figure due to mantle flow, which we can approximate using two lines of reasoning. First, the excess ellipticity of the Earth is recognised as being the consequence of two large scale megaplumes within the mantle [Lithgow-Bertelloni & Silver, 1998]. Hence, $k_{nh}/k_2^T(LT = 0, s = 0)$ (see equation 2.7) — i.e., the ratio of the excess and hydrostatic ellipticity — thus provides one measure of the net normalised load due to mantle flow. For the Earth models described above, $k_2^T(LT = 0, s = 0) = 0.9342$, and $k_{nh} = 0.008$ from Nakiboglu [1982], and hence this ratio is ~ 0.0086 (or 0.86%). Alternatively, the difference in the Earth's two principal equatorial moments of inertia, $(B - A)$, is also presumably due to mantle convection, and the observed ratio $(B - A)/(C - A) \sim 0.007$ [Gross, 2007]. It is reasonable to assume that this ratio would also be approximately equal to the fractional contribution of convection to the observed $C - A$, and thus it provides a second, consistent estimate of the total normalised load due to convection.

Now, the timescale for density heterogeneities to complete a circuit through a whole mantle

convection cell is, using surface plate speeds as an estimate for the characteristic flow velocity, approximately 100 Myr. This suggests that, over a timescale of 1 Myr, the variation in the normalised load due to mantle flow will be of order 1% of the total, or $\sim 8 \times 10^{-5}$. To be conservative, our 'standard test case' will be 10 times this value, $Q' = 0.0008$. While we will consider the sensitivity of the TPW predictions to a variation in the load size, it is important to emphasise that the standard test case represents a load variation equivalent to $\sim$ 10% the excess ellipticity over timescales of just ~ 1 Myr.

The standard test case will also be defined by an Earth model with LT =25 km, a lower mantle viscosity (henceforth ν_{LM}) of 10^{22} Pa s, and $k_{nh} = 0$. In regard to the convection signal, we will assume two forms of time dependence. The first is a sinusoidal forcing,

$$\frac{\mathbf{I}_{eff}(t)}{\bar{\mathbf{I}}_{eff}} = \sin(2\pi t/\tau), \tag{2.27}$$

where $\tau = 1$ Myr in the standard case. The second has the form

$$\frac{\mathbf{I}_{eff}(t)}{\bar{\mathbf{I}}_{eff}} = \big\{\tanh[A(t-B)] + 1\big\}/2, \tag{2.28}$$

where $A = 6$ Myr^{-1} and $B = 0.5$ Myr in the standard run. In this case, the right hand side of equation (2.28) increases from a value of 0 to 1 in 1 Myr. We will perform a sequence of sensitivity analyses in which ν_{LM}, LT, τ, and k_{nh} are varied.

2.3.1 Periodic Forcing

To begin, Figure 2.5 shows a prediction of TPW and TPW rate as a function of time for the standard test case. The results are generated using (solid line) the new rotation theory that accounts for the stabilisation due to the remnant bulge (equation 2.24 with $k_{nh} = 0$) and (dashed line) the theory in which this stabilisation is absent (equation 2.25). It is clear from the figure that the remnant

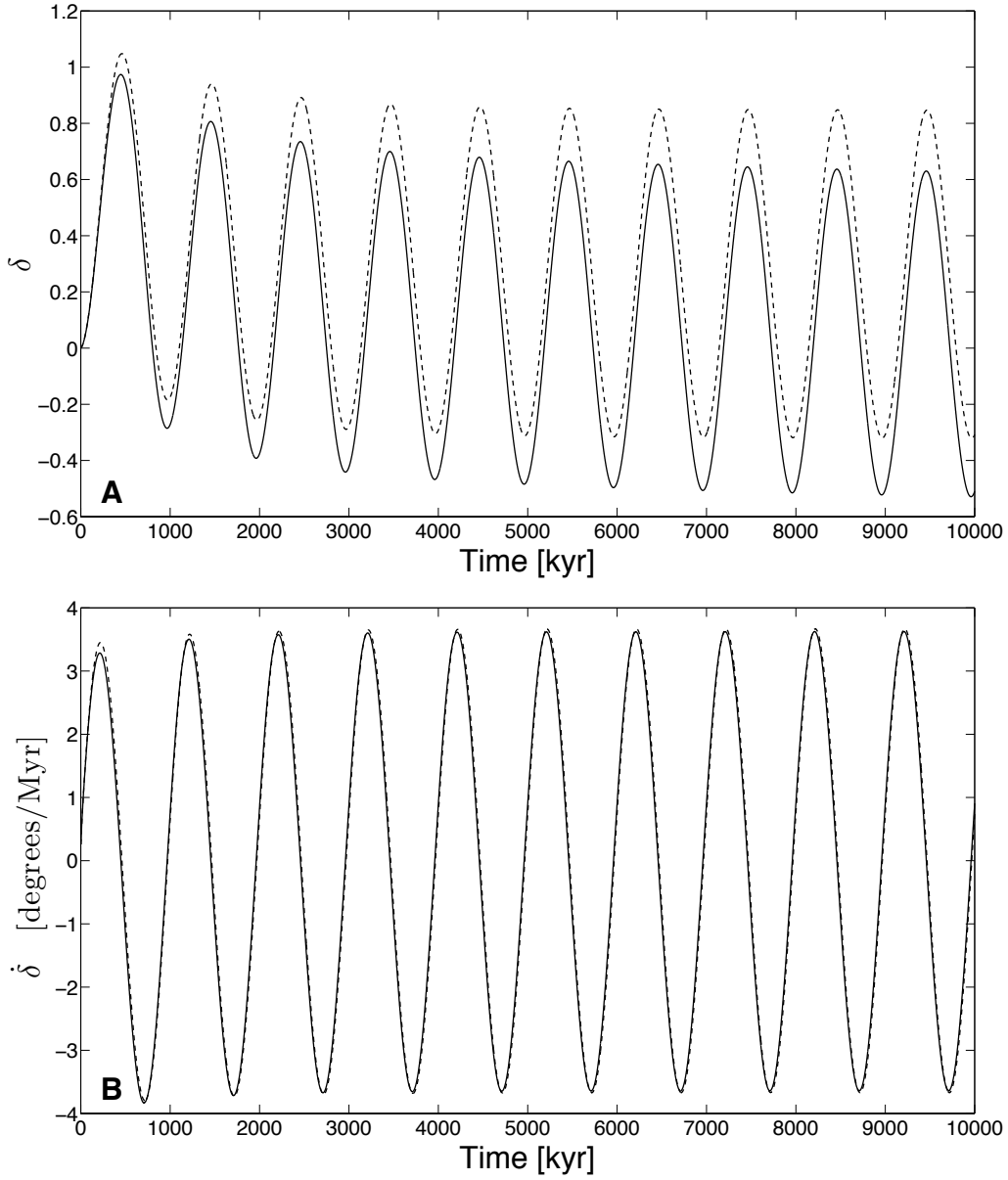

Figure 2.5: Predicted (A) TPW and (B) TPW rate versus time computed using (dotted line) our time dependent treatment of the traditional rotation physics (equation 2.25), and the (solid line) new rotation theory which includes stabilisation associated with the remnant rotational bulge (equation 2.25) with k_{nh} set to zero. All other aspects of the solution are based on the standard test case: LT = 25 km, ν_{LM} = 10^{22} Pa s, Q' = 0.0008, and τ_c = 1 Myr. The time dependence of the inertia tensor perturbation is given by equation (2.27).

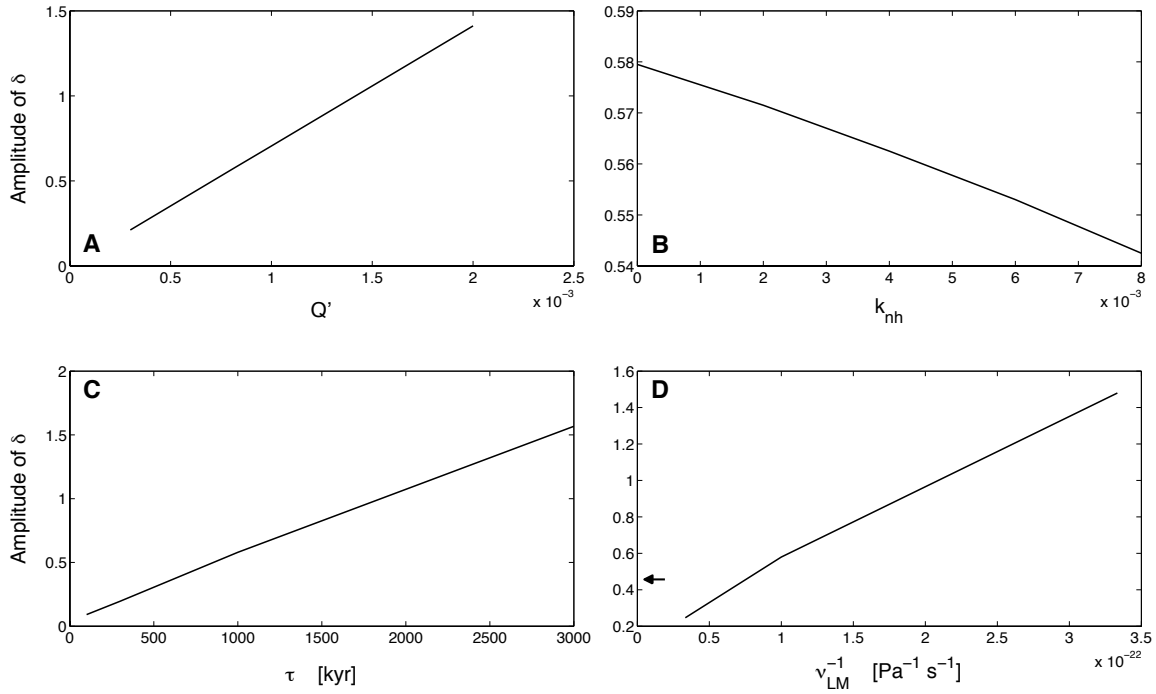

Figure 2.6: Predicted TPW amplitude (half the peak-to-peak variation) as a function of the (A) normalised load size Q', (B) the adopted background excess ellipticity k_{nh}, (C) the period τ_c of the sinusoidal perturbation to the inertia tensor (I_{eff}), and (D) the adopted lower mantle viscosity, ν_{LM}. Calculations adopt the new rotation theory (equation 2.25) and, with the exception of the parameter being varied, the solutions are based on the standard test case values: LT = 25 km, ν_{LM} = 10^{22} Pa s, Q' = 0.0008, and τ_c = 1 Myr. The arrow in frame D indicates the amplitude predicted in a calculation in which we adopt the viscosity profile inferred from a joint inversion of ice age and convection data sets (see text).

bulge stabilisation does not contribute significantly to either the TPW or its rate of change for a sinusoidal loading with period of $\tau = 1$ Myr.

In Figure 2.6, we explore the sensitivity of the TPW prediction in the standard test case solution to variations in the normalised load size Q', the excess ellipticity k_{nh}, the period τ of the forcing, and the adopted lower mantle viscosity ν_{LM}. We also performed an analysis (not shown) in which the elastic lithospheric thickness, LT, was varied from the standard value (25 km). This latter analysis, as well as the results associated with varying k_{nh} (Figure 2.6B), show relatively little sensitivity to a variation in the associated parameter, and this generalises the conclusion we reached on the basis of Figure 2.5; namely, the amplitude and TPW rate for a forcing of period $\sim$ 1 Myr are

insensitive to the stabilisation associated with either a remnant rotational bulge or a stable (on the timescale of the forcing) excess ellipticity.

The remaining results in Figure 2.6 confirm the general sensitivities identified by Tsai & Stevenson [2007]. In particular, the amplitude of the TPW, and the peak rate of change (which can be inferred, in units of deg Myr^{-1}, from Figure 2.6 by multiplying the y-axis values by a factor of ~ 4.5), are linearly sensitive to the loading amplitude and the period of the sinusoidal forcing, and they are inversely proportional to the lower mantle viscosity. The linear relationship between the predictions and Q' is, in fact, explicit in our governing equation (2.24).

So, what is the amplitude and speed limit of TPW in response to a rapid, periodic forcing? Let us consider a loading timescale of $\tau \sim 1$ Myr. In this case, the standard run yields a maximum peak-to-peak amplitude of $\sim 1^{\circ}$, and a maximum speed (which is only attained for a short period of time) of 3.5 deg Myr^{-1}. As we have discussed, the standard Q' value we have adopted represents a variation in the mantle convective loading of 10% of the total convective load over a specified timescale τ. Simulations of mantle convection extending over the past 20 Myr indicate that over a 1 Myr timescale the peak variation in the convection-induced load is a fraction of one percent of the total signal [see Forte & Mitrovica, 1997, Figure 2.3a], suggesting that our standard value for Q' is a very conservative upper bound. The standard run also adopted a lower mantle viscosity $\nu_{LM} = 10^{22}$ Pa s. Recent, joint inversions of data related to ice age sea-level adjustments and mantle convection [Mitrovica & Forte, 2004] infer a mean deep mantle viscosity in excess of this value. On Figure 2.6D, we superimpose the predicted amplitude of TPW generated using this specific inference of viscosity – this calculation yields an amplitude about 15% lower than the standard case. We note that some ice age studies have suggested a lower mantle weaker than 10^{22} Pa s [Peltier, 2004]. However, the data sets used in such analyses (e.g., relative sea-level histories) are primarily sensitive to shallow lower mantle structure. Spherical harmonic degree-2 anomalies (e.g., TPW) will be sensitive to viscosity variations in the deep mantle, a region where ice age data sets provide limited radial resolution [Mitrovica, 1996]. Therefore, the lower mantle

viscosity adopted in the standard run is also a conservative choice.

2.3.2 A Gradual Step Change in the Convective Loading

Next, we consider TPW driven by a net change in the convective forcing defined by the time history in equation (2.28). For the standard run ($A = 6.0$ Myr^{-1} and $B = 0.5$ Myr), this time history involves a ramp-up in the load from a value of 0 to Q' in 1 Myr, with the most rapid change in the middle 0.5 Myr of the loading phase. Beyond this phase, the load stays in place. The solid lines in Figure 2.7A and B are the predicted TPW and TPW rate computed using our (linearised) time-dependent form of the traditional rotational stability theory (equation 2.25) with all parameters set to the standard test run case. As discussed above, the equilibrium theory of Gold [1955] (i.e., the final frame of Figure 2.1A) will ultimately place the load on the equator, and since the load is positioned at a colatitude of 40°, this means a final TPW of 50°. In our linearised theory, the instability described in the context of Figure 2.1A leads to an unbounded TPW, although we will focus our attention on the time history well within the linear regime mapped out by Figures 2.2–2.4.

Two million years after the load is fully emplaced, the net TPW has reached 6° and the TPW rate is $\sim$ 2 deg Myr^{-1}. At 10 Myr from the onset of loading (not shown), these values are 18.2° and $\sim$ 1.65 deg Myr^{-1}, respectively. This suggests that the time required for the load to reach close to the equator, for the suite of parameters that define the standard test case, is at least 50 Myr.

The long-dashed line in each frame of Figure 2.7 represents a prediction based on the new rotation theory that incorporates the stabilisation of the rotation pole associated with the remnant bulge (equation 2.24 with $k_{nh} = 0.0$). In contrast to the case of sinusoidal loading, this stabilisation has a pronounced impact on the reorientation of the rotation pole. Two million years after the full load is established, the pole has reached $\sim$ 4.5°, and the TPW rate has dropped to 1 deg Myr^{-1}, or half the rate predicted in the absence of the stabilisation due to the remnant bulge. At 10 Myr after the onset of loading (not shown), the TPW rate has fallen to 0.3 deg Myr^{-1}, and the net TPW has reached 8.4°.

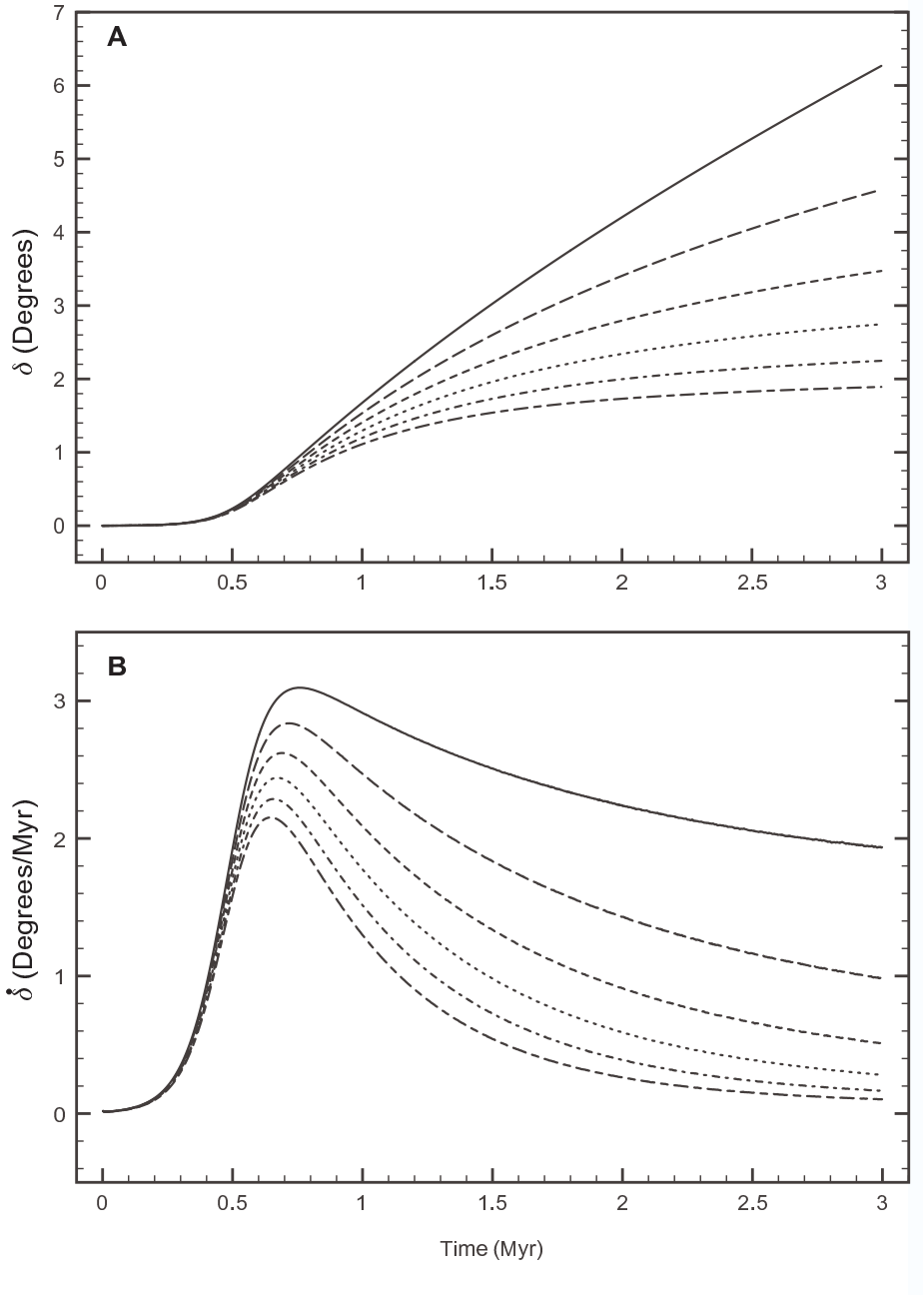

Figure 2.7: (A) TPW and (B) TPW rate versus time computed using the (solid line) time domain treatment of the traditional rotation theory (equation 2.25), and the new rotation theory (equation 2.24) with k_{nh} set to either (long-dashed line) 0.0 (the standard test case), (short-dashed line) 0.002, (dotted line) 0.004, (dashed-dotted line) 0.006, or (long-dashed-short-dashed line) 0.008. All other aspects of the solution are based on the standard test case: LT = 25 km, ν_{LM} = 10^{22} Pa s, Q' = 0.0008, and time dependence of the inertia tensor perturbation is given by equation (2.28) with A = 6 and B = 0.5.

The remaining predictions in Figure 2.7 illustrate the progressively stronger stabilisation of the rotation pole as the remnant bulge physics is augmented by successively higher amplitudes of stable (over the 3 Myr timescale covered by the plot) excess ellipticity. Indeed, in the 3 Myr since the onset of the loading, the predicted TPW for the most stable case, with an adopted excess ellipticity equal to the present-day value ($k_{nh} = 0.008$, as discussed above), has essentially ceased and the final reorientation is $\sim 2^{\circ}$. We note that the present-day, non-hydrostatic figure of the Earth is triaxial, and the excess ellipticity values in the direction of the two principal equatorial axes are actually 0.0115 and 0.0052 [Matsuyama et al., 2010] (the average of these to numbers gives the 0.008 value quoted above); thus the precise level of stabilisation would, in the case of a triaxial figure, be a function of the direction of the TPW.

We conclude from Figure 2.7 that during periods of relative hiatus in the variability of the convective loading, ongoing TPW predicted on the basis of the traditional rotational stability theory (equation 2.25) may be a significant overestimate. Stabilisation associated with both a remnant rotational bulge and an excess ellipticity which remains stable over the period of the hiatus will both strongly inhibit TPW. It is important to note that the stabilisation associated with the excess ellipticity is independent of the remnant bulge stabilisation. That is, although the 4 lower lines in each frame of Figure 2.7 consider the two effects in tandem, we could have alternatively considered the excess ellipticity stabilisation in the absence of the remnant bulge stabilisation associated with the elastic lithosphere.

In Figure 2.8 we return to the standard test case (long dashed lines in the frames of Figure 2.7) and consider the sensitivity of the predictions to (from first to last row) the normalised size of the load (Q'), the timescale of loading, the lower mantle viscosity, and the thickness of the elastic lithosphere. In all cases, we use the time-domain equation (2.24) with $k_{nh} = 0$.

In the top row we explore the impact of varying Q' from 0.0003 to 0.003. As discussed above in the context of the periodic forcing, the predictions of TPW and TPW rate for the ramp-up forcing should be linearly related to Q' (equation 2.24), and this is clearly evident in Figure 2.8. As an

example, at 700 kyr, the net TPW rate predictions for $Q' = 0.0003$ and 0.003 are $\sim$ 1 deg Myr^{-1} and $\sim$ 10 deg Myr^{-1}, respectively.

The sensitivity of TPW and TPW rate predictions to variations in the timescale over which the load is applied (second row, Figure 2.8) is relatively small once $\sim$ 3 Myr have elapsed. Peak TPW speeds are obtained in the latter part of the loading ramp-up, and the amplitude of this peak decreases as the ramp-up period increases, from 4.2 deg Myr^{-1} for the 0.1 Myr ramp-up case to 2 deg Myr^{-1} for the case of a 3 Myr ramp-up. Significantly, 5 Myr after the onset of loading, the TPW rate for all four cases treated in Figure 2.8F have converged to just under 1 deg Myr^{-1}.

The third row of Figure 2.8 considers the impact on the TPW predictions of increasing the lower mantle viscosity by an order of magnitude. During the loading ramp-up, both the TPW and TPW speed decrease monotonically with increasing ν_{LM}. However, as the ramp-up slows, and in the period after the ramp-up, the predicted TPW speeds decay at different rates and by 3 Myr they have converged to nearly the same value as in Figure 2.8F: 1 deg Myr^{-1}. What is causing this transition from the early sensitivity to viscosity to the latter insensitivity? During the initial onset of the load, TPW is limited by the ability of the bulge to readjust and this, in turn, is governed by the lower mantle viscosity – the higher the viscosity, the more sluggish the adjustment. However, after a relatively modest level of TPW has occurred, the stabilising impact of the remnant bulge associated with the elastic lithosphere, which will increase with increasing TPW, becomes dominant, and this stabilisation is insensitive to lower mantle rheology. Hence, the predicted TPW rates will converge in this interval.

This transition from a TPW response dominated by viscous bulge adjustment to remnant bulge stabilisation is evident schematically in Figure 2.1, where in the first few columns of the figure the TPW path is similar for both scenarios. As time progresses and the remnant bulge stabilisation takes over, the TPW in the second scenario is significantly more muted than in the first case. The transition also explains why, after the ramp-up in loading, TPW rates converge to a roughly similar value (1 deg Myr^{-1}); the stabilising impact of the remnant bulge is not only insensitive to the lower

Figure 2.8 ***(following page)*****:** Predicted (left column) TPW and (right column) TPW rate versus time for a suite of predictions in which individual parameters are varied from the value which defines the standard test case. All calculations are based on the time-domain equation (2.24), with k_{nh} set to zero, and the time-history of loading given by equation (2.28). (A,E) Q' varied from (solid line) 0.003, (dotted line) 0.001, (long-dashed line) 0.0008, and (short-dashed line) 0.0003. (B,F) Ramp-up timescales of (solid line) 100 kyr, (dotted line) 300 kyr, (long-dashed line) 1 Myr, and (short-dashed line) 3 Myr. (C,G) ν_{LM} varied from (solid line) 3×10^{21} Pa s, (long-dashed line) 10^{22} Pa s, and (dotted line) 3×10^{22} Pa s. (D,H) LT varied from (solid line) 10 km, (long-dashed line) 25 km, (short-dashed line) 46 km, (dotted line) 67 km, and (dashed-dotted line) 88 km. With the exception of the parameter being varied, the solutions are based on standard test case values: LT = 25 km, ν_{LM} = 10^{22} Pa s, Q' = 0.0008, and τ_c = 1 Myr.

Figure 2.8: (continued)

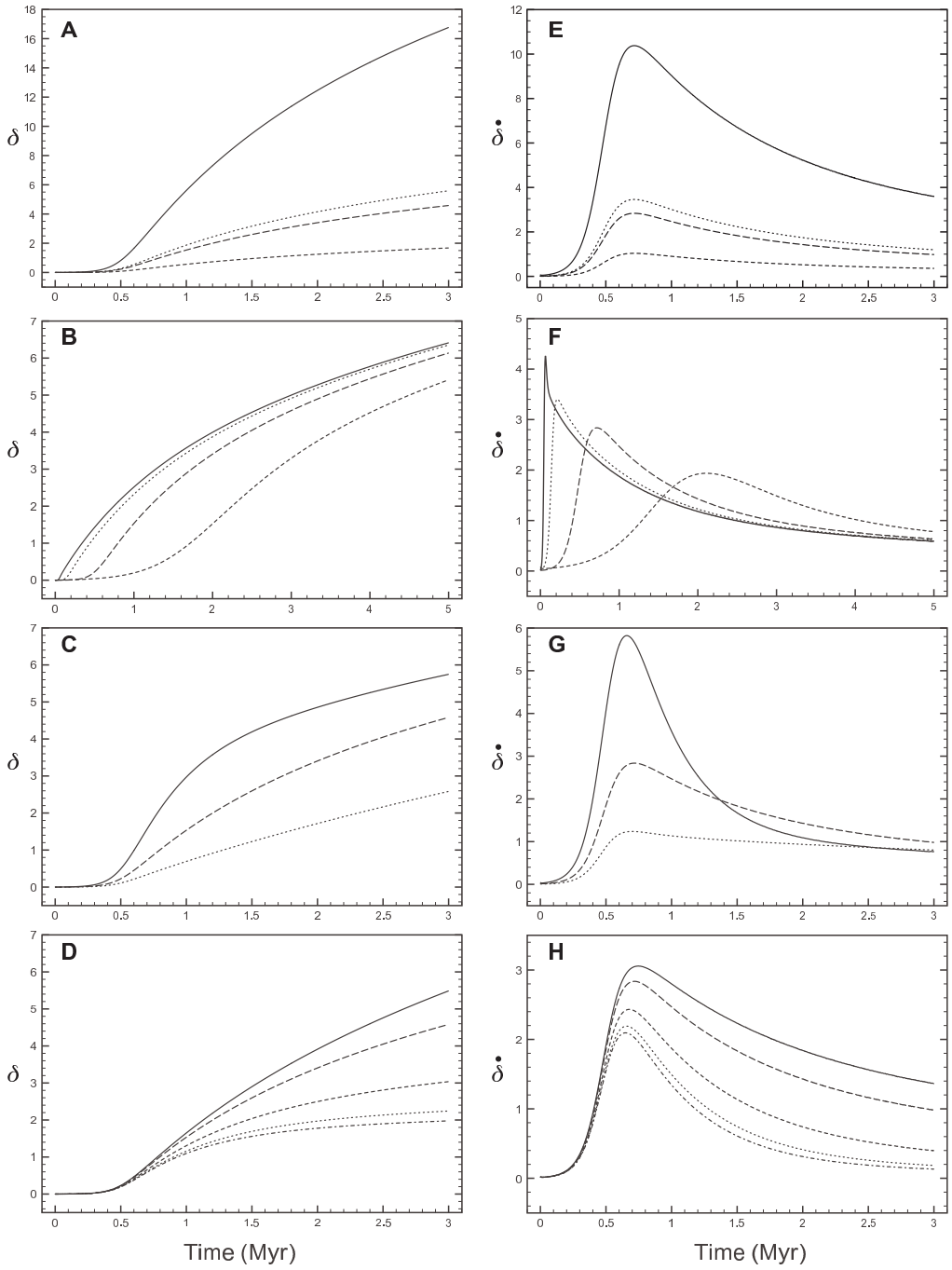

mantle viscosity, it is also insensitive to the period over which a load of normalised size Q' is built up. Of course, since the ultimate location of the pole is governed by a balance between the load size and the remnant bulge stabilisation, the curves in Figure 2.8E will exhibit more sensitivity than those in Figures 2.8F and 2.8G in the period after the load is fully in place; however, each of these curves will eventually converge to zero as the polar motion ceases (i.e., at the point where the strength of the load and the stabilisation strength become equal).

In the final row of Figure 2.8, we consider the sensitivity of the predictions to changes in the thickness of the elastic lithosphere, *LT*. As one increases *LT*, one increases the strength of the remnant bulge, and hence the predicted TPW remains a strong function of the adopted value of *LT* well after the load ramp-up; this is also reflected in the predicted TPW rates, which show significant differences 3 Myr after the onset of loading. Once again, this sensitivity contrasts with results based on the sinusoidal forcing.

The predictions in Figure 2.8 adopt $k_{nh} = 0$, and thus they do not include any stabilisation associated with a background excess ellipticity. As discussed above, the present-day excess ellipticity of the Earth along the intermediate and minimum axes of inertia are 0.0052 and 0.0115, respectively. We do not know how this convection signal has varied in the past; however, it will always be true, as discussed in the context of Figure 2.1, that the rotation vector will tend to reorient such that any excess ellipticity moves towards the equator. In any event, for the sake of illustration, and to be conservative, in Figure 2.9 we repeat the simulations in Figure 2.8 with k_{nh} set to 0.004. To facilitate comparison, Figure 2.9 is drawn using the same scales as Figure 2.8.

Introducing this relatively modest level of excess ellipticity yields a net TPW at 5 Myr that is only about half the total TPW predicted in the absence of this stabilisation. During the ramp-up in the loading, the TPW and TPW rate are less sensitive to the choice of k_{nh}; however, the discrepancies grow during the period in which the loading is complete. This is yet another manifestation of the transition from a load-dominated TPW phase to a phase in which the stabilising effects of the remnant bulge and the excess ellipticity begin to dominate.

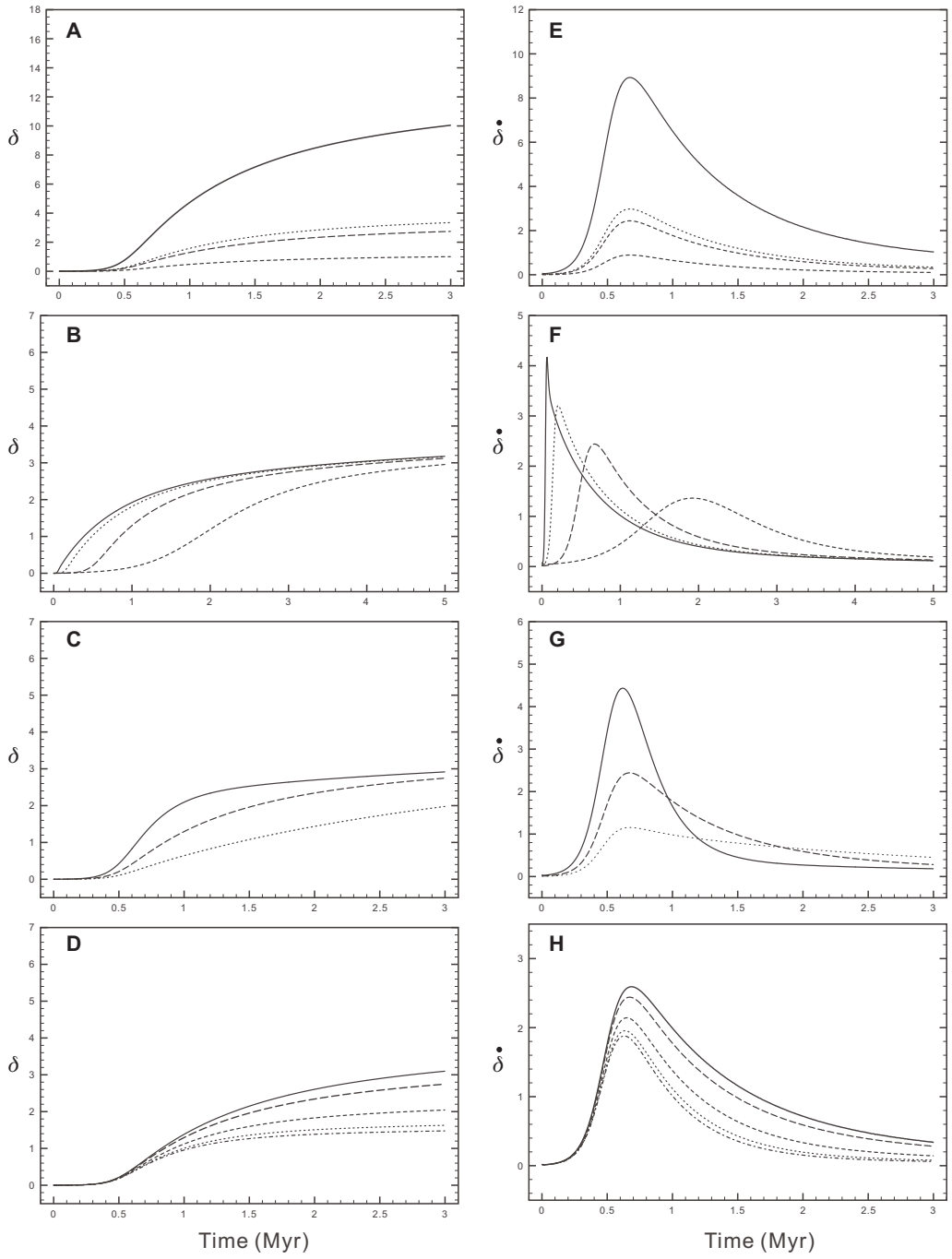

Figure 2.9: As in Figure 2.8, except all calculations adopt k_{nh} = 0.004, and thus incorporate stabilization due to excess ellipticity.

Using the results in this section, we can reassess the inference by Sager & Koppers [2000] of 16°–21° of TPW in 2–5 Myr during the Late Cretaceous. Let us assume that this reorientation was due to a net shift in the convective loading. The results in Figure 2.8B and 2.9B demonstrate that TPW over this time period would be relatively insensitive to the timescale of the ramp-up in the convective load. In the absence of any stabilisation due to excess ellipticity, the predictions in Figure 2.8A indicate that TPW of this amplitude would require a convective load of $Q' \sim 0.003$. Adopting an excess ellipticity of $k_{nh} = 0.004$ (Figure 2.9A) increases the size of the required load by about 60%, i.e., $Q' = 0.005$. (The Earth's excess ellipticity 85 Ma is unknown; however, the size of the megaplume structures below Africa and the Pacific suggest that this convectively supported contribution to the oblateness of the Earth may not have been significantly different from today's value. Therefore, in this case, adopting $k_{nh} = 0.004$ is likely an underestimate.) The required load size would be only marginally smaller if we adopted a lower mantle viscosity as low as 3×10^{21} Pa s (Figures 2.8C, 9C) or an elastic lithospheric thickness as thin as 10 km (Figure 2.8D, 2.9D). The palaeomagnetic inference of Sager & Koppers [2000] thus requires that a convective forcing on the order of the size of the current excess ellipticity of the Earth must have been applied in a timescale of a few million years. We conclude, on this basis, that the palaeomagnetic inference is physically implausible.

2.4 Final Remarks

Using recent results in ice age theory [Mitrovica et al., 2005], we have derived a linearised rotational stability theory that permits predictions of time-dependent TPW on a convectively loaded Maxwell Earth. A special case of the theory allows one to assess the time dependence of the rotation vector under assumptions consistent with the canonical equilibrium stability theory first described by Gold [1955] (Figure 2.1A) and adopted in most previous analyses of convection-induced TPW. However, in its most general form, our theory augments this canonical treatment

to include the possible stabilisation of the Earth's rotation vector due to the remnant bulge associated with an elastic lithosphere and any excess ellipticity in the Earth's shape that is stable over the timescale of interest. The linearisation is valid for small angles of TPW; however, we have demonstrated the conditions under which the error in the treatment is less than 5% for TPW reaching 20°.

As a first application of the theory, we have considered TPW in response to relatively rapid, $\sim$ 1 Myr, perturbations in the inertia tensor. In this regard, we have adopted two specific time histories: a periodic (sinusoidal) forcing, and a gradual ramp-up (hyperbolic tangent) forcing. The calculations using the periodic forcing have largely confirmed results by Tsai & Stevenson [2007], who concluded that the TPW angle and rate would be linearly proportional to the magnitude and period of the loading and inversely proportional to the adopted lower mantle viscosity. We have also demonstrated that these predictions are, within the parameter regime we have considered, insensitive to the stabilisation associated with the remnant bulge or excess ellipticity. Using our predictions, we conclude that TPW of amplitude $\sim$ 10° with $\sim$ 1 Myr periodicity would require large — and in our view unrealistic — perturbations in the inertia tensor over this timescale. Indeed, these inferences suggest changes in the inertia tensor over timescales of 1 Myr that are much larger than 10% of the perturbation implied by the Earth's present-day excess ellipticity.

Our predictions based on a step ramp-up in the convection load show far greater sensitivity to the stabilisation associated with the remnant bulge and excess ellipticity. More specifically, in the case of the load ramp-up, we note a transition from load-dominated TPW during the period of active loading to a phase, after loading is complete, in which the remnant bulge and excess ellipticity significantly limit polar motion. Indeed, these stabilising factors are sufficient to stop the rotation pole far from the equatorial position expected on the basis of the canonical stability theory of Gold [1955]. We should emphasise that this limit on TPW has been understood and applied within the literature of planetary rotation [e.g., Willemann, 1984; Matsuyama et al., 2006; Daradich et al., 2008] — in this regard, the theory described herein extends these efforts to consider the time history of the evolution of pole position in the presence of these stabilisation mechanisms. On the

basis of these predictions, we have concluded that the inference of a 16°–21° reorientation of the rotation pole over 2–5 Myr during the Late Cretaceous is also implausible.

The predictions described here assume that the elastic lithosphere of the Earth is unbroken. As we discussed in the § 2.1, an important question that needs to be addressed is to what extent the 'effective elastic thickness' of the real Earth in response to a perturbed centrifugal potential differs from response of a model Earth with an unbroken elastic lithosphere of some thickness *LT*. As a preliminary assessment of this issue, we used a finite-element numerical procedure developed for ice age geodynamic problems [Latychev et al., 2005] to compare the 1 Myr response of: (1) an Earth model with an elastic lithosphere of thickness 100 km at all locations except at plate boundaries where (by virtue of a finite viscosity) the elastic thickness is zero, and (2) a sequence of Earth models with a uniform elastic thickness that is varied from 10 km to 100 km. We found that the (spherical harmonic degree two, order one) response of the broken lithosphere model to a perturbation in the centrifugal potential arising from a 5° shift in the pole along the Greenwich meridian was the same as the response at the same degree and order of a uniform elastic lithosphere of thickness $LT \sim 60$ km. This suggests that the effective elastic thickness *LT* of the Earth in response to forcings on timescales of $\sim$ 1 Myr is a sizeable fraction of the mean lithospheric thickness, and that the standard value of $LT = 25$ km we adopted in the present study is a reasonable and conservative choice. Nevertheless, it is important to recall that the effective elastic thickness of the broken lithosphere, and hence the importance of the remnant bulge stabilisation, will be a function of the timescale of the forcing. For example, analyses of TPW over timescales of 10s–100s of Myr would have to account for the fact that the creation of oceanic lithosphere near mid-ocean ridges sets the local form of the plate to the contemporaneous hydrostatic figure. A conservative test of the effective elastic thickness of the lithosphere in this case might set the elastic strength of the oceanic component of the lithosphere to zero [see Creveling et al., 2012]. Plate motions during TPW events may also play a role in establishing the strength of the remnant bulge stabilisation over such timescales.

The normal mode treatment we have described provides a flexible methodology for investigating the impact on convection-induced TPW of a suite of other factors related to Earth structure. For example, our results have assumed that the lithosphere is characterised by infinite viscosity (i.e., that it is purely elastic). Adopting a finite viscosity lithosphere would introduce a normal mode with a relaxation time given by the Maxwell time of the lithosphere, and as we have noted this would lead to a transient remnant bulge stabilisation. In addition, alternate linear rheologies can be treated without any additional complexity in the modelling. Finally, within the range of linearisation, our theoretical methodology can be used to assess other aspects of the Earth's rotational stability in response to convective forcing. These include, for example, the relatively muted TPW inferred for the past few 100 Myr from palaeomagnetic data [Besse & Courtillot, 2002; Steinberger & Torsvik, 2008]. This is the topic of the next chapter.

But the people on it fretted out their days with troubles and cares and endless worries, as though without these troubles, these cares, and these worries, the day wouldn't turn into night.

Nescio, *Amsterdam Stories*
(trans. Damion Searls)

3

The Rotational Stability of a Convecting Earth, II

The Earth's Figure and TPW Over the Last 100 Myr

3.1 Introduction

A broad suite of geophysical processes, including atmospheric and ocean circulation, tides, glacial isostatic adjustment and mantle convection, alter mass distribution within the Earth system and drive a reorientation of the rotation axis relative to the surface geography. This reorientation is characterised by timescales ranging from seconds to hundreds of millions of years [Lambeck, 1980; Munk & MacDonald, 1960]. At the short-time end of this spectrum, the polar motion is periodic, or nearly so, and the phenomenon is known as a wobble of the rotation axis [Smith, 1977; Wahr, 1982]; an example is the Earth's Chandler wobble, a $\sim$ 8 m motion of the pole with a period of 14-months that is excited, at least in part, by ocean mass transport [Gross, 2000]. At longer

times scales, the motion of the rotation axis is known as true polar wander, or TPW. For example, surface (ice plus ocean) mass redistribution and isostatic adjustment of the Earth in consequence of the Late Pleistocene glacial cycles drove a net displacement of the pole of 1° or less, and an ongoing TPW speed of less than 1°/Myr [Nakada, 2002; Mitrovica et al., 2005]. Moreover, modern observations of TPW speed are commonly corrected for ice-age effects, and the residual signal is then used to estimate recent mass flux from ice sheets and glaciers driven by global climate change [e.g., James & Ivins, 1997; Johnston & Lambeck, 1999; Munk, 2002; Mitrovica et al., 2005; Tosi et al., 2005; Mitrovica et al., 2006]. At timescales ranging from millions to hundreds of millions of years, the reorientation of the rotation pole is driven by thermal convection in the Earth's mantle [e.g., Steinberger & O'Connell, 1997; Richards et al., 1997; Greff-Lefftz, 2004; Schaber et al., 2009; Torsvik et al., 2010; Zhang et al., 2010] — the same process that is ultimately responsible for plate tectonics.

The most extensively studied, and best-constrained example of long-term TPW is, perhaps not surprisingly, the drift of the rotation pole over the last 100 Myr. The pole path during this time span, inferred by Besse & Courtillot [2002] on the basis of updated kinematic constraints on plate motions and globally distributed palaeomagnetic records, is shown in Figure 3.1 (black line). According to their reconstruction, the rotation axis drifted 12° towards East Siberia from 97 Ma to 52 Ma, then, after remaining relatively stationary in the next 44 Myr (52 to 8 Ma), reversed direction and drifted 6° towards Greenland to reach its present-day location. It is notable that in this entire time window the rotation axis remained within 6° of its current location.

Discussions of the physics of long-term TPW driven by mantle convective flow are commonly based on a rotational stability theory that dates back to the mid-20th century [Gold, 1955]. The Gold theory, henceforth the 'standard theory', is an equilibrium theory; that is, given a surface or internal mass load, the theory predicts the final state of the rotation pole, but says nothing about the timescale of TPW towards this final state. According to the theory, TPW is driven by mass redistribution and is resisted by the rotational bulge of the planet. Under the assumption that the

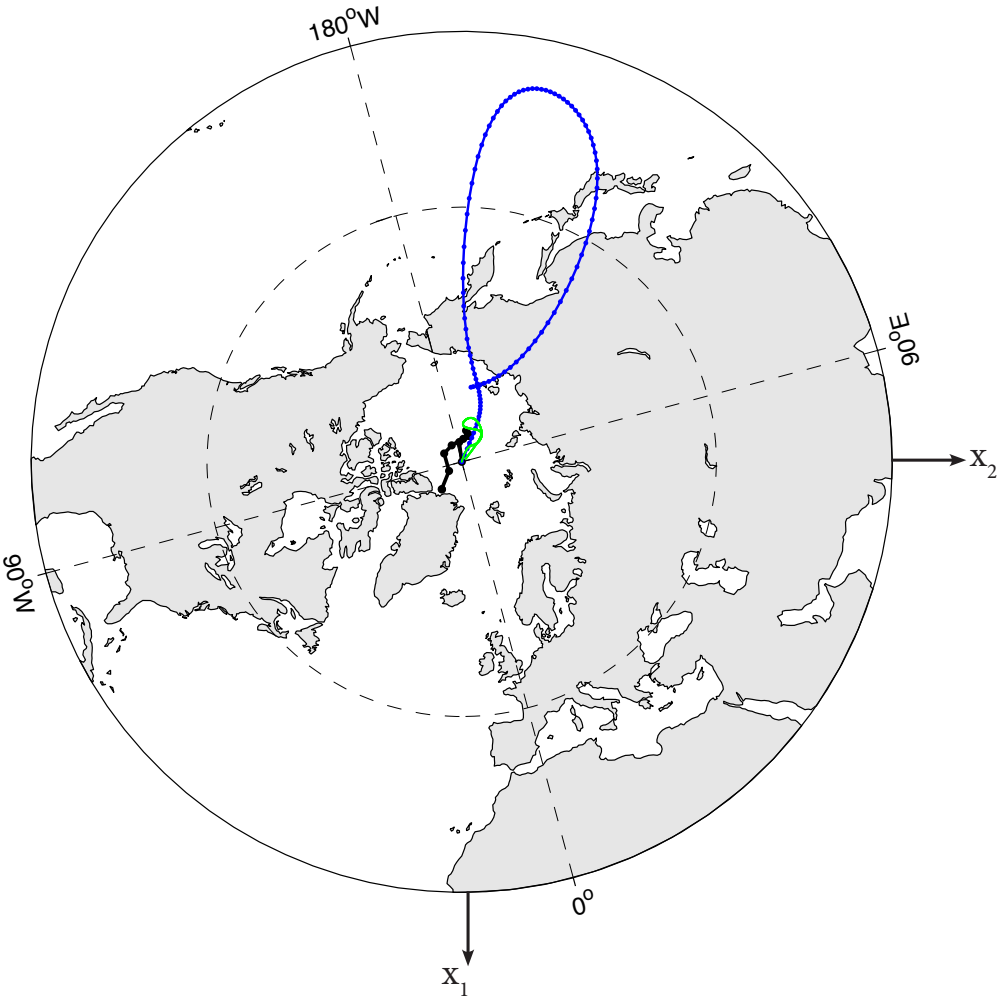

Figure 3.1: TPW over the last 100 Myr superimposed on a top-down projection of the northern hemisphere (with continents in their present location) that specifies longitude, as labelled, latitude (dashed line, 45°N; outer circle, 20°N), and the orientation of the minimum (X1) and intermediate (X2) axes of non-hydrostatic inertia. The solid black line is the TPW path inferred by Besse & Courtillot [2002] on the basis of palaeomagnetic records. The remaining lines are predictions of TPW driven by the convection-induced inertia tensor perturbations described in the text (see Figure 3.3). These predictions are: solid blue line – TPW based on the standard equilibrium rotational stability theory [Gold, 1955]; solid green line – TPW based on the revised rotational theory in the case where stabilisation of the rotation axis associated with the Earth's excess ellipticity is included (equation 3.6, with LT set to zero in the numerator). In the case of the latter, the peak inertia tensor perturbation in Figure 3.3 is scaled to be equal to 20% of the mean present-day excess ellipticity.

rotational bulge will ultimately adjust perfectly to any new pole position, the standard theory argues that any load, even one as small as the canonical beetle that Goldreich & Toomre [1969] used to illustrate the physical arguments, will reach the equator. The adoption of an equilibrium theory presumes that convective driving forces have a timescale much longer than the timescale that characterises the viscoelastic adjustment of the rotational bulge. In mathematical terms, the standard theory predicts that the rotation axis will remain aligned with the principal axis of maximum inertia associated with the convective forcing. In this case, studies of convection-induced TPW need only track the rotation axis by diagonalising the total inertia tensor perturbation associated with the convective forcing at each step in the simulation. The standard equilibrium stability theory essentially argues that the rotation axis is ultimately unstable in the presence of an isostatically uncompensated mass load, and this inherent instability generally leads to predictions of long-term TPW that are larger than observed values.

The timescale of the reorientation of the rotation axis is linearly related to the size of the load [Tsai & Stevenson, 2007; Chan et al., 2011a]; thus, even if the equilibrium position of the convective load is the equator, it may take hundreds of millions of years for TPW to move it there [Tsai & Stevenson, 2007]. Accordingly, a number of studies have extended the standard theory to incorporate the stabilising effect of a time-dependent, viscoelastic adjustment of the rotational bulge [Ricard et al., 1993; Steinberger & O'Connell, 2002; Tsai & Stevenson, 2007; Chan et al., 2011a]. The Ricard et al. [1993] methodology involves asymptotic expressions for the long-time viscoelastic adjustment of the Earth, and it has been adopted in a number of subsequent investigations of convection-induced TPW [e.g. Richards et al., 1999; Greff-Lefftz, 2004; Schaber et al., 2009].

The difficulty of reconciling the muted TPW over the last 100 Myr estimated from palaeomagnetic records (Figure 3.1) with convection simulations coupled to the standard rotational stability theory has been well documented in the literature [e.g., Steinberger & O'Connell, 1997; Richards et al., 1997; Schaber et al., 2009]. One possible route to resolving the disagreement is to increase the mantle viscosity so that the advection of density heterogeneities associated with convective

flow is slowed [Steinberger & O'Connell, 1997; Richards et al., 1999]. However, a recent mantle convection simulation [Schaber et al., 2009] predicted a TPW rate of 0.5°/Myr using Earth models with a mean lower mantle viscosity of 10^{23} Pa s. This viscosity is in excess of the value preferred on the basis of inversions of geodynamic data [Mitrovica & Forte, 2004], and the TPW rate is three times larger than the palaeomagnetically inferred speed over the last 100 Myr (Figure 3.1). Moreover, Steinberger & O'Connell [1997] demonstrated that TPW predictions based on a plausible model of mantle viscosity could yield a wide range of TPW rates, depending on the geometry of the convective forcing. In this regard, Richards et al. [1997] have argued that the stability of the rotation pole over the last 100 Myr is a consequence of a slow change in the pattern of plate tectonic motions beginning in the Late Cretaceous. Their arguments were extended by Rouby et al. [2010] in two ways; first, they concluded that the stabilisation was a function of the depth to which Pacific plates subduct under the Americas; and, second, following Greff-Lefftz [2004], they demonstrated that the level of rotational stabilisation is also controlled by the existence of two upwelling, antipodal deep-mantle superplumes, one below southern Africa and the other under the southern Pacific [Lithgow-Bertelloni & Silver, 1998; Forte & Mitrovica, 2001; Simmons et al., 2009].

A somewhat different, but related argument connects the rotational stability of the Earth to its non-hydrostatic figure. Goldreich & Toomre [1969] demonstrated that the present non-hydrostatic figure of the Earth is triaxial, and the difference between the maximum (polar) and intermediate (equatorial) moments of inertia is approximately the same as the difference between the intermediate and minimum (equatorial) moments of inertia. That is, convective flow in the Earth's mantle, comprised of the antipodal superplumes and the ring of subduction at the margins of the Pacific, is currently driving an excess (relative to hydrostatic) ellipticity along both principal equatorial axes of (non-hydrostatic) inertia. Regardless of the relative contributions from upwelling or downwelling flow, if this excess ellipticity has been stable over a timescale of, say τ_{ee}, then it will have stabilised the rotation axis in the presence of convective forcings with smaller amplitude and

timescale shorter than τ_{ee} [Goldreich & Toomre, 1969]. Indeed, a stable excess ellipticity has been cited in several studies as a possible explanation for the muted TPW since the break-up of Pangea [Evans, 1998; Zhang et al., 2010]. The timescale over which this stabilisation has persisted is a matter of debate, and it is clearly related to the stability of both the superplume and slab contributions to the equatorial excess ellipticity [Steinberger & Torsvik, 2010]. For example, Steinberger & Torsvik [2010] and Rouby et al. [2010] both assume that the superplume contribution to the excess ellipticity and rotational stability has remained constant over timescales of order 120 Myr, and they associate palaeomagnetically-inferred TPW over this time span with changes in slab subduction rate and geometry.

In this paper we revisit the question of why convection-induced TPW over the last 100 Myr has been so subdued. In particular, we follow two lines of enquiry. The first is related to the long wavelength geometry of mantle flow since the Late Cretaceous. Specifically, we provide a bound on the stability of the excess ellipticity that would be necessary to reconcile the palaeomagnetically-inferred TPW over the last 100 Myr (Figure 3.1). Second, we outline a potential stabilising effect on the Earth's rotation that is not incorporated into either the standard theory, nor a number of extensions to this theory [Ricard et al., 1993; Steinberger & O'Connell, 2002; Tsai & Stevenson, 2007]. In particular, these theories do not include the impact on TPW of a lithosphere that retains non-zero elastic strength over long timescales. Work in planetary rotation has demonstrated that an elastic lithosphere has a significant stabilising impact on the long-term rotational stability of a terrestrial planet [Willemann, 1984; Matsuyama et al., 2006; Daradich et al., 2008] because any TPW would induce an elastic restoring force on the pole. This stabilisation is known as the remnant bulge [Willemann, 1984; Matsuyama et al., 2006]. In an application to the Earth, in contrast to single-plate planets such as Mars [Daradich et al., 2008], the importance of the remnant bulge stabilisation may be diminished, perhaps significantly, by the existence of breaks in the lithosphere; however, there is ample geological evidence that the Earth's lithosphere retains elastic strength over relatively long timescales [Watts, 2001]. In any event, we explore the extent to which a rem-

nant bulge may have contributed to the observed rotational stability since the Cretaceous.

We return to these various points below, where we summarise and apply the time-dependent (i.e., non-equilibrium) and linearised rotational stability theory derived by Chan et al. [2011a] that incorporates stabilisation due to viscous adjustment of the rotational bulge, excess ellipticity and the remnant bulge. We begin, in the next section, with a summary of the basic physics of long-term rotation, as discussed by Gold [1955], and then extend this physics to include these additional sources of stabilisation.

3.2 Background

3.2.1 The Physics of Long-Term Earth Rotation

The standard rotational stability theory [Gold, 1955] described in § 3.1 is summarised, schematically, in Figure 3.2A. Consider an initially unloaded, rotating Earth with a hydrostatic form, i.e., a form in which all long-term sources of material strength within the crust and mantle material have fully relaxed as fluids to the imposed centrifugal potential (Figure 3.2A1). Next, a positive load is placed on or inside this model Earth — the internal load might represent, for example, the total density heterogeneity due to mantle convection. The load will be pulled towards the equator in inertial space, or, from the perspective of an Earth-bound observer, the pole will move away from the load (Figure 3.2A2). This reorientation of the axis will meet resistance from the rotational bulge, which has been contemporaneously pushed off its original location on the equator; however, Gold [1955] argued that this resistance is transient, since the bulge will eventually viscously readjust to align once more with the equator (Figure 3.2A3). Once it does so, this sequence repeats and the TPW will continue in incremental steps until the load finally reaches the equator (Figure 3.2A4). As discussed above, the rotation axis ultimately remains aligned with the principal axis of maximum inertia associated with the convective (i.e., non-hydrostatic) forcing. We note, once more, that the standard equilibrium theory only specifies the ultimate location of the

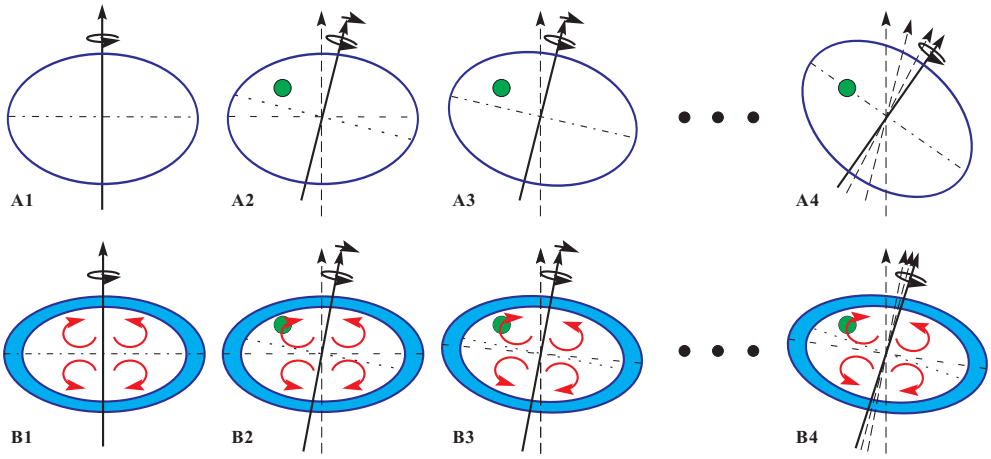

Figure 3.2: Schematic illustrating physical models of convection-induced TPW. In this figure, the green dot is a positive, convection-induced load, the red swirls represent long wavelength mantle flow that supports an excess ellipticity, and the blue shell is an elastic lithosphere. The individual figures are drawn in the frame of reference of the load. The vertical dashed line with arrow is the initial position of the rotation axis, while the solid line with arrow is the rotation axis at the time sampled by the associated frame. Any active polar motion is denoted by a small arrow above the rotation axis. Within the interior of the planet, the dashed line is the axis of the rotational bulge, while the dotted line is the equator (i.e., 90° from the contemporaneous rotation axis). Row A – the physics underlying the standard rotational stability theory of Gold [1955], and in this case A4 represents the equilibrium position predicted by this theory. Row B – the physics underlying the revised rotational stability theory described in this study, including stabilisation associated with both the remnant bulge (elastic lithosphere) and excess ellipticity.

rotation axis (Figure 3.2A4), not the timescale over which the TPW takes place. As discussed in § 3.1, a number of studies have extended the standard theory to account for the time-dependent relaxation and stabilisation associated with the rotational bulge [Ricard et al., 1993; Steinberger & O'Connell, 2002; Tsai & Stevenson, 2007; Chan et al., 2011a].

Next, we consider the potential stabilisation of the pole associated with an excess ellipticity and/or a remnant bulge. As discussed above, the observed flattening of the Earth has an excess, non-hydrostatic ellipticity due to large scale mantle flow associated with the Pacific ring of subduction and two deep mantle superplumes below southern Africa and the Pacific. This excess ellipticity is $\sim$ 1% of the hydrostatic value [Nakiboglu, 1982; Chambat et al., 2010]. In a general treatment of convection-induced TPW, the excess ellipticity would be considered part of the con-

vectively evolving, non-hydrostatic form of the Earth. However, if the large scale flow has been stable for some geologically significant period (denoted by τ_{ee} in § 3.1), then the excess ellipticity effectively serves as a significant stabilising effect on TPW driven by any smaller amplitude, shorter timescale convective flow. In the terminology of Gold [1955], the stable excess ellipticity would provide a memory of the rotational state of the Earth that will persist over the timescale τ_{ee}. Convection simulations suggest that $\tau_{ee} \sim 100$ Myr [Zhang et al., 2010], while studies of various geological and geophysical data sets have argued for a timescale in excess of 500 Myr [Dziewonski & Anderson, 1981; Torsvik et al., 2010]. In a similar vein, the remnant bulge stabilisation associated with the presence of long-term strength in the lithosphere also provides a memory of the original rotational state. In practise, the remnant bulge stabilisation will be active as long as the lithosphere does not viscously relax, a timescale we label as τ_{rb}.

The combined stabilisation associated with the remnant bulge and excess ellipticity is illustrated, schematically, in Figure 3.2B. Consider an Earth model with an unstressed elastic lithosphere and a background form that, in consequence of mantle flow, has slightly greater flattening than the hydrostatic form associated with its rotation rate (Figure 3.2B1; note the excess flattening of Figure 3.2B1 relative to 2A1). If this model is subject to a load, the pole will, as in the Gold [1955] scenario, move away from the load and the bulge will initially resist this TPW (Figure 3.2B2). As before, the latter resistance will weaken as the rotational bulge adjusts to the new orientation of the rotation axis. However, unlike the scenario in Gold [1955], the adjustment of the bulge will not be perfect, i.e., the adjustment will not bring the bulge back onto the equator (Figure 3.2B3) over timescales less than the larger of τ_{ee} and τ_{rb}, either because of the stable excess ellipticity and/or because any TPW will be resisted by elastic stresses in the (initially unstressed) lithosphere (i.e., the remnant bulge). The TPW will continue in incremental steps until a balance is achieved between the force pulling the load towards the equator and the combined stabilising effect of the excess ellipticity and resisting elastic forces associated with the lithospheric deformation (Figure 3.2B4).

Our goal is to quantify the potential stabilisation associated with these two effects in the context of TPW spanning the last 100 Myr of Earth history. We begin by summarising a revised theory that incorporates both effects within a time-dependent formulation for predicting long-term TPW.

3.2.2 A Linearised Theory of Long-Term Earth Rotation

In this section we summarise a recent, linearised treatment of convection-induced TPW valid for spherically symmetric, Maxwell viscoelastic Earth models [Chan et al., 2011a]. Our treatment of the equations governing conservation of angular momentum is valid for small motions of the pole (see Chan et al. [2011a] for a detailed analysis of the range of linearity, which can extend for tens of degrees), and it is based on recent results in ice age rotation theory [Mitrovica et al., 2005]. In this regard, we extend our earlier derivation to consider perturbations in the inertia tensor superimposed on a triaxial Earth, and we are guided in this effort by an analogous extension that has appeared in the ice age literature [Matsuyama et al., 2010].

We begin by assuming that in its unperturbed state the viscoelastic Earth model has a polar moment of inertia, C, and equatorial moments of inertia, A and B, that are equal and denoted by A (i.e., the background figure is biaxial), where $C > A$. In this same state, the angular velocity vector is given by $\mathbf{\Omega} = (0,\ 0,\ \Omega)$, where the first, second and third components of the vector are in the direction of the minimum, intermediate and maximum axes of inertia (for a biaxial Earth, the first two are any orthogonal equatorial directions), respectively. We will denote convection-induced perturbations to the inertia tensor by I_{ij} and the perturbed angular velocity vector by $w_i(t) = \Omega[\delta_{i3} + m_i(t)]$. The linearised theory requires that all the I_{ij} are smaller than the principal moments A and C, and that the $m_i \ll 1$.

The linearised theory also requires a methodology for computing perturbations in the inertia tensor associated with changes in the centrifugal potential that arise from TPW. This perturbation may be expressed in terms of the viscoelastic tidal k Love number at spherical harmonic degree

two [Matsuyama et al., 2006]. In the time domain, this Love number may be written as [Peltier, 1974; Wu, 1978]

$$k_2^T(LT, \nu, t) = k_2^{T,E}\delta(t) + \sum_{j=1}^{J} r_j e^{-s_j t}. \tag{3.1}$$

For the purpose of this summary, we have made the dependence of the Love number on both the thickness of any elastic component of the lithosphere (LT) and the radial profile of mantle viscosity (ν) explicit. It will be useful to also express the Love number in the Laplace transform (s) domain:

$$k_2^T(LT, \nu, s) = k_2^{T,E} + \sum_{j=1}^{J} \frac{r_j}{s + s_j}. \tag{3.2}$$

Using the latter, the so-called fluid Love number of the Earth model may be obtained by taking the limit $s \to 0$ in equation (3.2)

$$k_2^T(LT, s = 0) = k_2^{T,E} + \sum_{j=1}^{J} \frac{r_j}{s_j}. \tag{3.3}$$

Note that the fluid Love number does not depend on the radial viscosity profile, but will be a function of the thickness of the elastic lithosphere.

Using equation (3.1), the solution of the linearised conservation equation (the so-called Liouville Equation) can, in the time-domain, be written as [Chan et al., 2011a]

$$\mathbf{m}(t) = \frac{\mathbf{I}(t)}{C - A} + \frac{k_2^T(LT, \nu, t)}{k_2^T(LT = 0, s = 0) + k_{nh}} * \mathbf{m}(t), \tag{3.4}$$

where $\mathbf{I}(t) = I_{13}(t) + iI_{23}(t)$, and $\mathbf{m}(t) = m_1(t) + im_2(t)$. In the Laplace transform-domain, this equation is

$$\mathbf{m}(s) = \frac{\mathbf{I}(s)}{C - A} \cdot \frac{1}{1 - \frac{k_2^T(LT, \nu, s)}{k_2^T(LT=0, s=0) + k_{nh}}}. \tag{3.5}$$

In these two equations, $k_2^T(LT = 0, s = 0)$ is the fluid Love number of the same Earth model used

to compute $k_2^T(LT,\nu,t)$ or $k_2^T(LT,\nu,s)$ with the exception that the viscosity of the lithosphere is taken as finite. In this $LT=0$ case, the $s=0$ limit in equation (3.3) represents the equilibrium hydrostatic (i.e., fluid) form of the rotating Earth model as it would be predicted using Love number theory. Furthermore, k_{nh} represents any stable (over the timescale of the convective loading being considered) non-hydrostatic (excess) ellipticity in the Earth's figure. Thus, $k_2^T(LT=0,s=0)+k_{nh}$ represents the background elliptical form upon which the inertia tensor perturbations due to mantle convection are superimposed.

The extension of these equations to the case of a triaxial background form is straightforward [Matsuyama et al., 2010] and is given by

$$\begin{aligned} m_1(t) &= \frac{I_{13}(t)}{C-A} + \frac{k_2^T(LT,\nu,t)}{k_2^T(LT=0,s=0)+k_{nh1}} * m_1(t) \\ m_2(t) &= \frac{I_{23}(t)}{C-B} + \frac{k_2^T(LT,\nu,t)}{k_2^T(LT=0,s=0)+k_{nh2}} * m_2(t) \end{aligned}, \tag{3.6}$$

and

$$\begin{aligned} m_1(s) &= \frac{I_{13}(s)}{C-A} \cdot \frac{1}{1-\frac{k_2^T(LT,\nu,s)}{k_2^T(LT=0,s=0)+k_{nh1}}} \\ m_2(s) &= \frac{I_{23}(s)}{C-B} \cdot \frac{1}{1-\frac{k_2^T(LT,\nu,s)}{k_2^T(LT=0,s=0)+k_{nh2}}} \end{aligned}. \tag{3.7}$$

In these equations, the terms k_{nh1} and k_{nh2} are the non-hydrostatic components of the Earth's figure in the direction of the minimum and intermediate axes of inertia, respectively. The present-day orientation of these axes is shown in Figure 3.1; note that the minimum moment of inertia is approximately 15° west of Greenwich longitude. Comparison of the observed figure of the Earth with the hydrostatic form computed using a second-order accurate hydrostatic theory [Chambat et al., 2010] yields $k_{nh1}=0.0129$ and $k_{nh2}=0.0065$.

Note that in our linearised rotational stability theory, perturbations to the pole position are linearly related to the inertia tensor perturbation. Thus, if one doubled the latter, the vector **m** would

also be doubled.

We will consider two special cases of these equations. In the first, we isolate the stabilising influence of excess ellipticity by adopting Earth models which do not have a purely elastic (infinite viscosity) lithosphere. Thus, the Love numbers $k_2^T(LT, \nu, t)$ and $k_2^T(LT, \nu, s)$ become $k_2^T(LT = 0, \nu, t)$ and $k_2^T(LT = 0, \nu, s)$, respectively. We note that the lithospheric viscosity we adopt in these cases will be the same as the underlying upper mantle. The second special case involves the incorporation of the remnant bulge stabilisation in the absence of excess ellipticity. In this case, we return to equations (3.4) and (3.5) with k_{nh} set to zero.

The standard rotational stability theory described by Gold [1955] assumes that the pole will remain aligned with the principal axis of the inertia tensor perturbation associated with mantle convection. This equilibrium theory assumes, implicitly, that the timescale of the adjustment of the rotational bulge in Figure 3.2A is faster than the characteristic timescale of mantle flow. We can relax this assumption and investigate how the actual timescale of bulge adjustment can stabilise the TPW by considering a special case of equations (3.4). (This special case of our theory is analogous to extensions from the standard theory treated by Ricard et al. [1993], Steinberger & O'Connell [2002] and Tsai & Stevenson [2007].) In particular, we set $k_{nh} = 0$ in these equations, and adopt an Earth model with no purely elastic component of the lithosphere. In this case, the equations governing time-dependent TPW become

$$\mathbf{m}(t) = \frac{\mathbf{I}(t)}{C - A} + \frac{k_2^T(LT = 0, \nu, t)}{k_2^T(LT = 0, s = 0)} * \mathbf{m}(t) \tag{3.8}$$

and

$$\mathbf{m}(s) = \frac{\mathbf{I}(s)}{C - A} \cdot \frac{1}{1 - \frac{k_2^T(LT=0,\nu,s)}{k_2^T(LT=0,s=0)}}. \tag{3.9}$$

Note that as $s \rightarrow 0$ in equation (3.9), the linearised system becomes unstable — this instability arises because in the equilibrium theory of Gold [1955] the system loses all memory of its original

rotational state. In the case of a single load applied and retained for all time, the TPW predicted using our linearised system becomes unbounded; of course, in a non-linear equilibrium theory, the load, no matter how small it is, will be on the equator.

3.3 Results and Discussion

To quantify the standard and revised rotational stability theories described above, we follow an approach described in a second canonical treatment of Earth rotation [Goldreich & Toomre, 1969] and compute a synthetic time series of the convection-induced perturbation in the inertia tensor. Specifically, to simulate the inertia tensor perturbation, we adopt the model of a randomly evolving planet considered by Goldreich & Toomre [1969]. We generate a sequence of $N = 10^3$ random points on the surface of the planet and we assign to the nth point a mass $m_n(t = 0)$ chosen from a Gaussian distribution with zero mean and magnitude M. The growth and decay of the mass anomalies is modelled assuming the following time dependence:

$$m_n(t) = m_n(t = 0) \exp\left[-\pi\left(\frac{t}{\tau_{conv}} - \frac{n}{10}\right)^2\right], \tag{3.10}$$

where τ_{conv} is the characteristic timescale for convection (which we choose as 20 Myr). The constants were chosen such that a different set of mass anomalies grow after the characteristic convection time has elapsed, and roughly 10 mass anomalies are at least half-grown at any given time.

Figure 3.3 shows the I_{13} and I_{23} inertia tensor perturbations from one realisation of this simulation. In applying the equilibrium rotational stability theory of Gold [1955], the orientation of the rotation axis is determined by diagonalising the full convection-induced inertia tensor and, in this case, scaling the mass anomalies by an arbitrary constant will not impact the computed orientation of the pole. The resulting orientation of the rotation axis at each step in the numerical simulation is shown in Figure 3.1 (blue line). The TPW path predicted using the standard equilibrium rotation

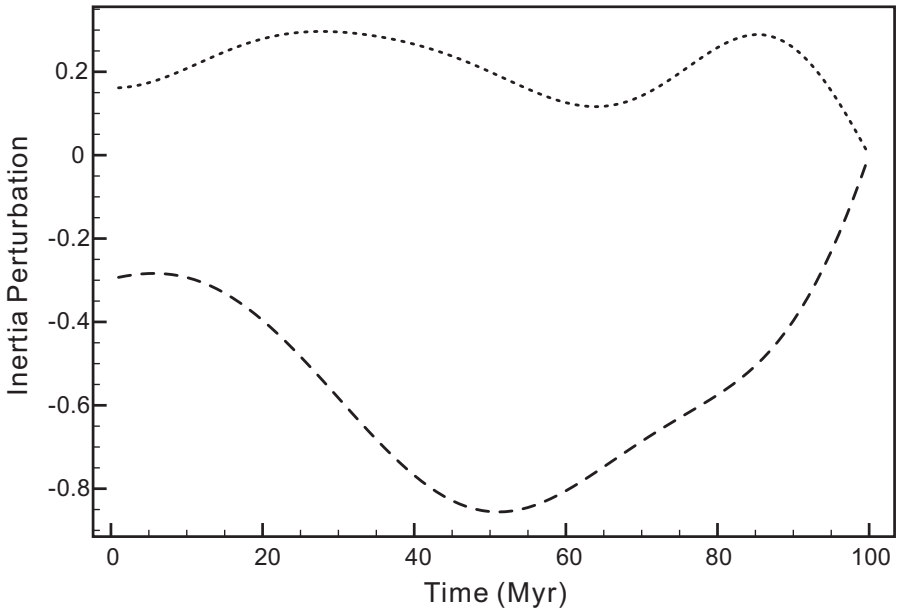

Figure 3.3: Time-dependent inertia tensor perturbations computed from one realization of randomly evolving mass anomalies (see text). Dashed line represents the I_{13} component of the perturbations, and the dotted line represents I_{23}.

theory grossly misfits the amplitude of the observed polar wander throughout the 100 Myr time window of the simulation.

As a further illustration of this misfit, both frames of Figure 3.4 shows the total, along-path displacement of the pole over the last 100 Myr computed for the palaeomagnetically-inferred TPW path (black lines) and predicted using the standard rotation theory (blue lines). We note that the integrated displacement that characterises the latter is 6 times greater than the observed value of $\sim 20^{\circ}$.

In applying the revised theory of rotational stability, and incorporating the potential stabilisation of the pole associated with excess ellipticity and a remnant bulge, our calculations will adopt a depth-dependent mantle viscosity profile characterised by constant upper and lower mantle values of 5×10^{20} Pa s and 10^{22} Pa s, respectively. This viscosity profile is in accord with average values inferred for each of these regions on the basis of a simultaneous joint inversion of an ex-

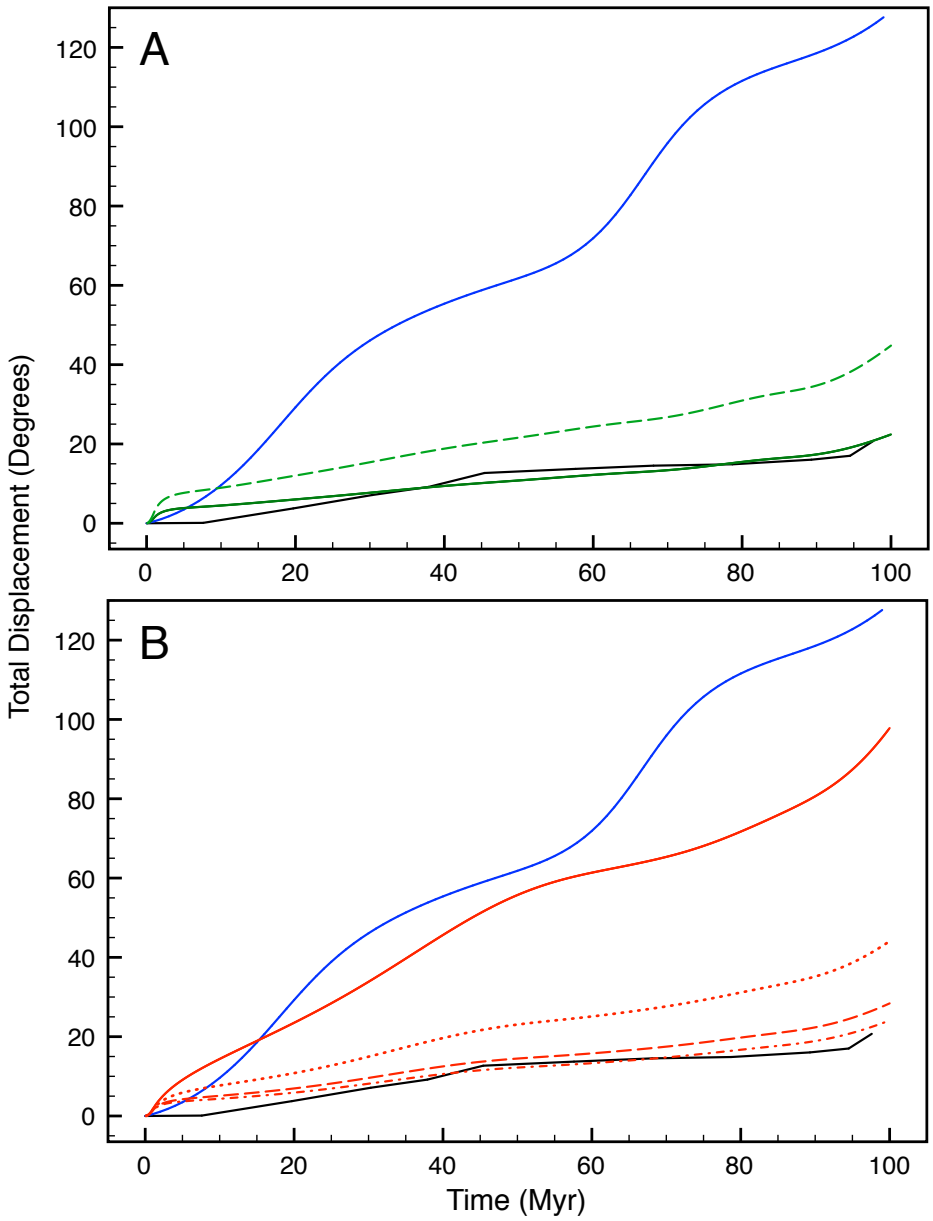

Figure 3.4: (A) The total along-path displacement of the TPW curves shown in Figure 3.1. The line colours are adopted from that earlier figure. The additional dashed green line is analogous to the solid green, with the exception that the peak convection-induced inertia tensor perturbation is doubled to 40% of the mean present-day excess ellipticity. (B) The solid blue and black line are reproduced from frame A. The four red lines are predictions of the total along-path displacement in the case where the revised rotation theory incorporates the stabilisation associated with the remnant rotational bulge (equation 3.4, with k_{nh} set to zero). These calculations adopt a lithosphere with elastic thickness (LT) of 25 km (solid), 46 km (dotted), 67 km (dashed) and 88 km (dashed-dotted).

tensive suite of data associated with glacial isostatic adjustment and mantle convection [Mitrovica & Forte, 2004]. The predictions described below, which are based on a prescribed inertia tensor perturbation, are relatively insensitive to details of this profile. (However, if we varied the viscosity profile, then the inertia tensor perturbation should in fact also be varied since the parameter τ_{conv} will be a function of viscosity.)

We begin with a prediction of time-dependent TPW in the case where stabilisation due to the excess ellipticity is included, but the remnant bulge is not. We once again adopt the inertia tensor perturbation in Figure 3.3, but we now scale these values so that the peak inertia tensor perturbation across the 100 Myr time window is 20% of the observed mean present-day excess ellipticity, or about two parts in a thousand of $(C - A)$. The predicted TPW path and the total along-path displacement are shown in Figures 3.1 (green line) and 3.4A (solid green line), respectively. The combination of the time-dependent adjustment of the Earth and the excess ellipticity is clearly sufficient to exert a significant stabilisation of the pole position; indeed, the predicted excursion of the pole, as reflected in the pole path and the total displacement, is 6 times smaller than predicted by the standard equilibrium rotational theory [Gold, 1955] and is thus in accord with the observed TPW. (Matching the direction of TPW is of no importance given the stochastic nature of the adopted inertia tensor perturbation.) As discussed above, the predicted TPW is linearly related to the inertia tensor perturbation, and therefore doubling the inertia perturbation to 40% of the observed excess ellipticity doubles the total along-path displacement (Figure 3.4A; dashed green line) and leads to a misfit with the observed TPW.

Next, we investigate the stabilisation associated with a remnant bulge in the absence of any excess ellipticity. In particular, using the inertia tensor perturbation in Figure 3.3 (scaled to 20% of the observed mean excess ellipticity), we compute the integrated displacement of the pole for a suite of Earth models with uniform elastic lithospheres of thickness ranging from 25–88 km (red lines, Figure 3.4B). As the thickness is increased, the stabilisation associated with the remnant bulge strengthens, and the predicted TPW decreases. Indeed, predictions based on an elastic litho-

sphere of thickness $\sim$ 70 km or greater are in accord with the palaeomagnetically inferred polar motion.

The calculations plotted in Figure 3.4B adopt a lithosphere with a globally uniform elastic thickness and this assumption raises a rather fundamental question: what is the effective elastic thickness of the Earth's broken, globally variable lithosphere in response to a centrifugal forcing with a timescale of 100 Myr? In the following we provide a preliminary estimate of this effective thickness.

In the absence of an excess ellipticity, the long-term stability of the axis of rotation will be governed by the ratio $k_2^T(LT, \nu, s)/k_2^T(LT = 0, s = 0)$ as $s \rightarrow 0$ (equation 3.5 with k_{nh} set to zero); in particular, the larger the discrepancy between the k_2^T fluid Love number computed for a model with ($LT \neq 0$) and without ($LT = 0$) a lithosphere, the greater the stabilisation. This discrepancy (and thus the remnant bulge stabilisation) increases as the elastic lithospheric thickness LT increases [Mitrovica et al., 2005], resulting in the trend of the red lines in Figure 3.4B. One can show [e.g., Mitrovica et al., 2005] that the limit of $k_2^T(LT, \nu, s)$ as $s \rightarrow 0$ is the same as the following infinite time response:

$$\lim_{s \rightarrow 0} k_2^T(LT, \nu, s) = \lim_{t \rightarrow \infty} H(t) * k_2^T(LT, \nu, t), \tag{3.11}$$

where $H(t)$ is a Heaviside step function and the asterisk denotes a time convolution. In other words, the fluid Love number can be computed by either considering the $s \rightarrow 0$ limit in the s-domain (equation 3) or, in the time-domain, by applying and retaining a spherical harmonic degree-2 load and computing the infinite time response to this load.

We return to the question posed above: what would the effective elastic thickness of the lithosphere be if the uniform shell were broken into tectonic plates? That is, what is the appropriate choice of LT in the Love number $k_2^T(LT, \nu, t)$ when considering the response of the Earth to a forcing of timescale 10–100 Myr? Creveling et al. [2012, supplementary information] considered this issue in a scenario characterised by a single continental plate in the Pangean supercon-

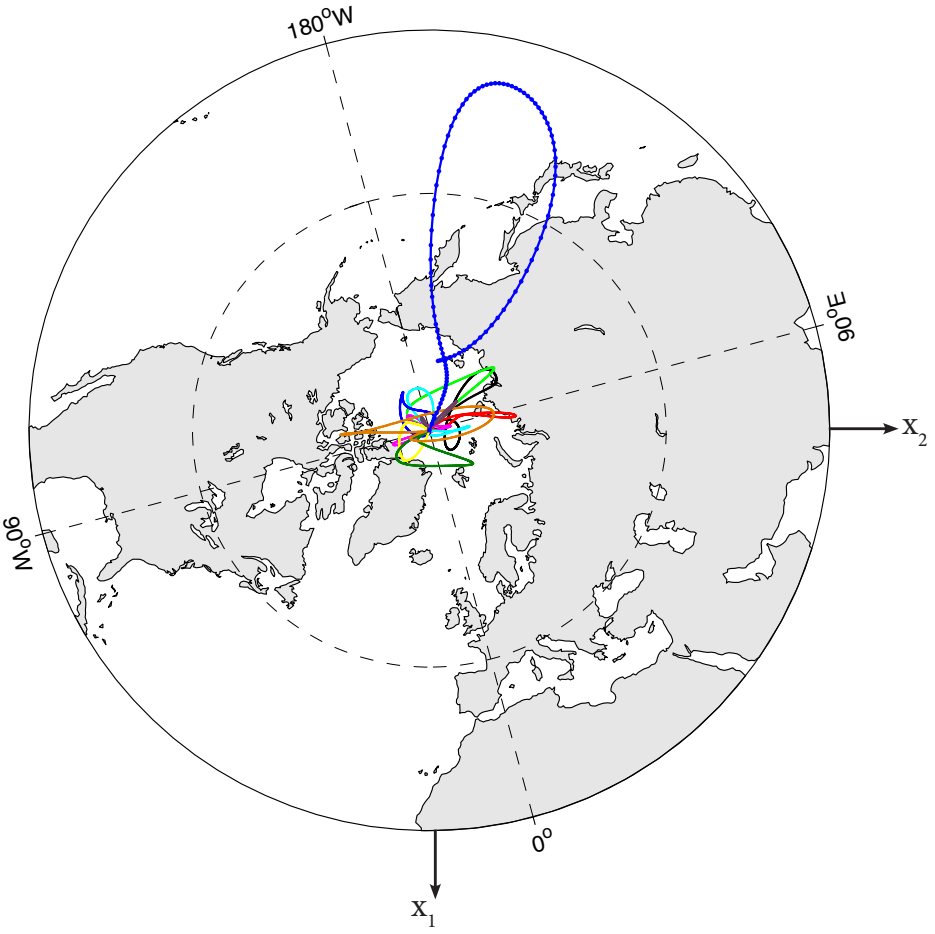

Figure 3.5: Predictions of TPW path based on the equilibrium rotational stability theory of Gold [1955] (blue line with dots) and (all remaining lines) based on the revised rotational theory in the case where stabilisation of the rotation axis associated with the Earth's excess ellipticity is included (equation 3.6, with LT set to zero in the numerator). The latter 10 lines are computed using different realisations of the stochastically-derived inertia tensor perturbation due to mantle convection. In all these cases, the peak inertia tensor perturbation is scaled to be equal to 20% of the mean present-day excess ellipticity.

tinent configuration surrounded by oceanic lithosphere that has no elastic strength. Their results indicate that, for continental lithospheric thicknesses of 100 km and 200 km, the equivalent 'effective' globally uniform lithospheres have elastic thicknesses of about 5 km and 10 km, respectively. These tests suggest that at least part of the observed stability of the pole position over the last 100 Myr may be a consequence of remnant bulge stabilisation, although a definitive conclu-

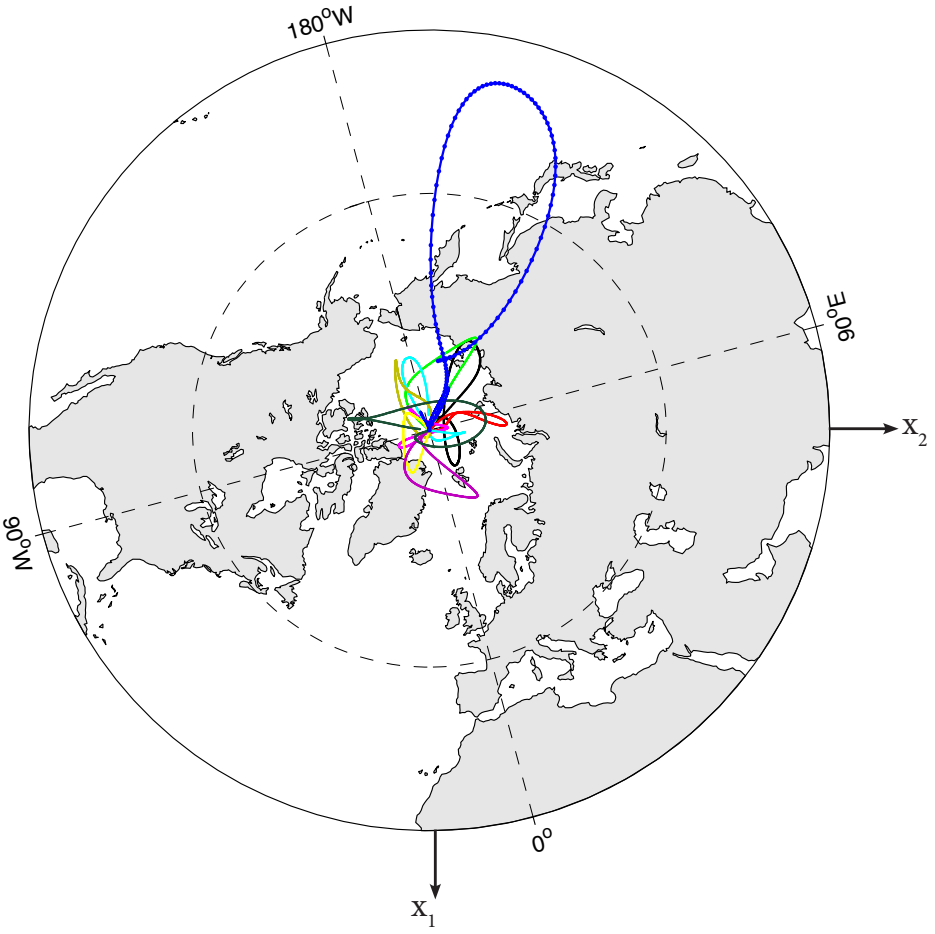

Figure 3.6: As in Figure 5, with the exception that all lines except the blue (with dots) are based on the revised rotational theory in the case where stabilisation of the rotation axis associated with a remnant bulge is included (equation 3.4 with $LT = 67$ km in the numerator and $k_{nh} = 0$).

sion in regard to this issue requires more detailed modelling of global lithospheric structure and rheology.

We have thus far only considered TPW predictions based on a single realisation of the stochastically-derived inertia tensor perturbation due to mantle convection (Figure 3.3). As a final sensitivity test, we have repeated the calculations in Figure 3.1 (green line) and computed the TPW path for a set of ten other time series of the inertia tensor perturbation, each with a peak magnitude of 20% of the mean observed present-day excess ellipticity. Results in the case where stabilisation of

the rotation axis associated with either the Earth's excess ellipticity (equation 3.6, with LT set to zero in the numerator) or the remnant bulge (equation 3.4, with k_{nh} set to zero and $LT = 67$ km) is included, are shown in Figures 3.5 and 3.6, respectively. These calculations confirm that the importance of the stabilising mechanisms we have described is not a result that is unique to the perturbation history shown in Figure 3.3.

The limited extent of TPW over the last 100 Myr, as inferred through analyses of palaeomagnetic data, has represented a long-standing issue in studies of Earth system evolution. A number of previous studies have pointed to a long-lived excess ellipticity as a possible cause of the muted TPW [Goldreich & Toomre, 1969; Evans, 1998; Zhang et al., 2010], and this stability of the Earth's figure must, in turn, relate to the stability of the long-wavelength component of mantle convection [Richards et al., 1997; Rouby et al., 2010; Steinberger & Torsvik, 2010]. We have demonstrated, using a time-dependent TPW theory incorporating several potentially important sources of rotational stability, that the muted TPW requires a convection-induced perturbation in the Earth's inertia tensor elements, I_{13} and I_{23}, over the last 100 Myr that is less than $\sim 20\%$ of the current excess ellipticity's impact on the inertia tensor. This upper bound may be higher if any portion of the Earth's lithosphere retains elastic strength over such long timescales.

To ask is always the desire to know. Yet the preservation of simple human truths requires mystery. The mysteries of happiness, death, and love.

Kris Kevin (character)
in *Solaris* [1972 Russian film], closing dialogue

4

Ice Age True Polar Wander

Did Glacially-Induced True Polar Wander End the Ice Age?

THE ROTATIONAL STABILITY of a terrestrial planetary body is governed by its viscoelastic response to applied forcings and by its background form or flattening. The first modern treatment of the rotational stability of an ice-age Earth, including perturbations to the rotation rate (or length of day, LOD) and orientation of the rotation vector relative to the surface geography (or true polar wander, TPW), date to the pioneering work of Sabadini & Peltier [1981] and Wu & Peltier [1984]. In both studies, the response of the Earth to the applied surface mass (ice plus ocean) loading and the centrifugal potential forcing driven by planetary reorientation was computed using viscoelastic Love number theory [Peltier, 1974]. Wu & Peltier [1984] also formulated the rotational response as a normal mode problem in which the complete time history of the evolving rotation vector was expressed as a superposition of rotational normal modes having distinct amplitudes and relaxation times [see also Mitrovica & Milne, 1998].

Ice-age TPW predicted using the above stability theories is characterised by an oscillatory back-and-forth nodding of the pole position, which reflects the glaciation-deglaciation phases of the ice-age cycles, and a slow drift of the pole away from its initial position. The latter (i.e. the slow drift) has two contributions. The first arises from the rotational normal modes with decay times that are sufficiently long relative to the typical ice-age cycle that each cycle contributes a small level of disequilibrium and pole displacement, whilst being sufficiently short that the mode is non-negligibly excited by loading associated with the ice-age cycle. In this case, each successive cycle adds to the net pole displacement until a steady state is reached where the contribution from the last cycle balances the relaxation from previous cycles [e.g. Sabadini et al., 1982, 1983; Wu & Peltier, 1984; Vermeersen et al., 1997; Mitrovica et al., 2001]. If the surface mass load returns to, and remains in its initial state, then this contribution to TPW will decay to zero with a timescale governed by the decay times of the rotational normal modes. The second contribution to the slow drift of the pole is the so-called 'unidirectional TPW' highlighted, in particular, by Wu & Peltier [1984]. This contribution is proportional to the time-integrated perturbation of inertia tensor elements and it is permanent in the sense that it is an unrecoverable shift in the pole position even in the case where the surface mass loading returns to its initial state. A physical explanation for the existence of this term has remained enigmatic.

The progressively increasing displacement of the rotation axis during ice-age loading that is predicted in the aforementioned treatments of rotational stability has played an important role in studies of ice-age climate. For example, Sabadini et al. [1982] have argued that the predicted drift of the pole position (by order 1°) altered Milankovitch forcing by an amount sufficient to transition the Earth system out of the present glacial epoch. Sabadini et al. [1983] reinforced this argument with additional calculations that demonstrated that the magnitude of the predicted drift was sensitive to the treatment of mantle phase transitions in the ice-age loading theory. In particular, the deflection of these boundaries in traditional Love number theory [Peltier, 1974] is responsible for the rotational normal modes with very long decay times that contribute to the recoverable compo-

nent of the slow drift discussed above [Mitrovica & Milne, 1998].

In this study we revisit the issue of the ice-age-induced drift of the rotation axis and its connection to ice-age climate. To begin, we briefly review the 'traditional' ice-age stability theory of Wu & Peltier [1984] and a revised stability theory that incorporates a more accurate treatment of the background oblateness of the Earth [Mitrovica et al., 2005; Cambiotti et al., 2010; Mitrovica & Wahr, 2011]. The latter treatments were motivated, in part, by the important study of Nakada [2002], who showed that the traditional theory led to enigmatic differences in TPW predicted using an elastic and very high viscosity viscoelastic lithospheres. We note that the term responsible for unidirectional TPW is missing from expressions in Mitrovica & Wahr [2011] and, using this insight, we derive a complete physical model that explains the existence of this term in the earlier theory. Next, we compare predictions of TPW based on the old and new theories driven by ice-age loading over various time windows, including the period of the last $\sim$ 1 Myr characterised by 100-kyr ice-age cycles, the 3 Myr since the end of the mid-Pliocene climate optimum, and the last 25 Myr. Our goal is to reassess the magnitude of net pole displacement over these glacial epochs and thus the veracity of previous claims that this drift was responsible for an important climatic transition in Earth history.

4.1 Theoretical Background

Descriptions of ice-age rotation are based on a linearisation of the equations governing conservation of angular momentum valid for small perturbations to the rotation vector. If we assume that all processes occur on a timescale much longer than the $\sim$ 14-month Chandler wobble period, then the linearised equation (the Liouville equation) in the Laplace Transform (i.e., s) domain is given by [Mitrovica et al., 2005]

$$\mathbf{m}(s) = \frac{\mathbf{I}^L(s)}{C-A} \frac{1 + k_2^L(s;\mathrm{LT})}{1 - \dfrac{k_2^T(s;\mathrm{LT})}{k_f}} , \tag{4.1}$$

where $\mathbf{m} = (m_1, m_2)$ is the perturbation to the initial rotation vector in the direction of Greenwich and 90°E, respectively; $\mathbf{I}^L = (I_{13}, I_{23})$ is the perturbation to the inertia tensor due to the direct effect of the surface mass loads; (A, A, C) are the principal moments of inertia in the (assumed biaxial) unperturbed state; and k_f is the observed fluid Love number, which represents a measure of flattening of the Earth's figure.

The parameters k_2^L and k_2^T are s-domain forms of the viscoelastic surface load and tidal (or tidal effective) k Love numbers, respectively, at spherical harmonic degree 2. These numbers are a function of the viscoelastic structure of the model Earth, although we only make explicit their dependence on the thickness of any elastic portion of the lithosphere (LT). These numbers can be expressed as [Peltier, 1976; Wu & Peltier, 1984]

$$k_2^L(s;\mathrm{LT}) = k_2^{L,E} + \sum_{k=1}^{K} \frac{r'_k}{s+s_k} \tag{4.2}$$

$$= k_2^L(s=0;\mathrm{LT}) - s\sum_{k=1}^{K} \frac{\frac{r'_k}{s_k}}{s+s_k} \tag{4.3}$$

$$= [-1 + l_s(\mathrm{LT})] - s\sum_{k=1}^{K} \frac{\frac{r'_k}{s_k}}{s+s_k}\,, \tag{4.4}$$

and

$$k_2^T(s;\mathrm{LT}) = k_2^{T,E} + \sum_{k=1}^{K} \frac{r''_k}{s+s_k} \tag{4.5}$$

$$= k_2^T(s=0;\mathrm{LT}) - s\sum_{k=1}^{K} \frac{\frac{r''_k}{s_k}}{s+s_k}\,, \tag{4.6}$$

where r'_k and r''_k are amplitudes of the normal modes of the viscoelastic surface load and tidal response, respectively, and s_k are their corresponding inverse decay times. Note that the term dependent on LT, $l_s \equiv 1 + k_2^L(s=0;\mathrm{LT})$, is 0 when $\mathrm{LT} = 0$; this term will be important later in this analysis.

The rotational stability of a rotating planet is governed by two competing forces. The first is the loading, which tends to drive TPW. The second is the delayed viscoelastic adjustment of the equatorial bulge, which tends to inhibit TPW. The numerator in equation (4.1) represents the effective forcing from the surface mass load, since it takes into account the viscoelastic compensation of the load (via the k_2^L Love number). The greater the departure from zero of this term, the greater the load-induced forcing of TPW. In contrast, the denominator represents the stabilisation associated with the delayed (and, as we will see, incomplete) adjustment of the equatorial bulge in response to TPW. The greater the departure from zero of this term, the greater the stabilisation associated with the bulge [Mitrovica et al., 2005; Cambiotti et al., 2010; Mitrovica & Wahr, 2011].

4.1.1 Wu & Peltier [1984] formulation

In the traditional approach to ice-age TPW, the observed fluid Love number of the Earth is approximated as $k_f \simeq k_2^T(s=0;\mathrm{LT})$ [Wu & Peltier, 1984]. Physically, this approximation is equivalent to assuming that the planet's oblateness is identical to the form that would be established by spinning up, to the present rotation rate, the same model planet used to compute the fluid Love numbers, and waiting until the system reaches equilibrium [Mitrovica et al., 2005]. Clearly, this predicted equilibrium form will have a flattening that depends on the adopted value of LT — the greater LT, the less oblate the form [Mitrovica & Wahr, 2011]. The above approximation, when applied to finely stratified Earth models, yields an estimate of the observed k_f with an error on the order of 1%.

Using the above approximation, Wu & Peltier [1984] inverted equation (4.1) into the time domain, giving

$$\mathbf{m}(t) = \frac{\Omega}{A\sigma_0}\left[D_1\mathbf{I}^L(t) + D_2\int_0^t \mathbf{I}^L(t')dt' + \sum_{k=1}^{K-1} E_k\left(\mathbf{I}^L(t) * e^{-\lambda_k t}\right)\right], \tag{4.7}$$

where Ω is the Earth's angular velocity, σ_0 is the Chandler wobble frequency of the deformable

Earth, λ_k are the inverse decay times of polar motion,

$$D_1 \equiv 1 + k_2^{L,E} \,, \tag{4.8}$$

$$D_2 \equiv l_s(\mathrm{LT}) \frac{\prod_{k=1}^{K} s_k}{\prod_{k=1}^{K-1} \lambda_k} \,, \tag{4.9}$$

and

$$E_k \equiv -\frac{\frac{l_s(\mathrm{LT})}{\lambda_k} \prod_{i=1}^{K} (s_i - \lambda_k) + \sum_{j=1}^{K} \frac{r'_j}{s_j} \prod_{\substack{i=1 \\ i \neq j}}^{K} (s_i - \lambda_k)}{\prod_{\substack{i=1 \\ i \neq k}}^{K-1} (\lambda_i - \lambda_k)} \,. \tag{4.10}$$

The first term in the square brackets of equation (4.7), with coefficient D_1, characterises the immediate elastic response of the rotation vector. The third term is the viscous response of the rotation vector, which involves a convolution in time between the inertia perturbation $\mathbf{I}^L(t)$, and a set of rotational modes of pure exponential decay with amplitudes E_k and inverse decay times λ_k. The decay times associated with the phase boundaries at 420 km and 670 km depth in the mantle can exceed 1 Myr [Mitrovica & Milne, 1998], and these modes are, in part, responsible for the slow drift of the rotation axis from its initial state predicted using the traditional rotation theory [Sabadini & Peltier, 1981; Wu & Peltier, 1984] when considering multiple glacial cycles [e.g. Sabadini et al., 1982, 1983; Wu & Peltier, 1984; Vermeersen et al., 1997; Mitrovica et al., 2001]. The second term in equation (4.7), involving the parameter D_2, is the second contributor to this slow drift; it represents a progressively increasing ('unidirectional') TPW signal that will be non-zero unless the elastic lithospheric thickness is zero, in which case $l_s = 0$.

As a final point, we define a parameter ϵ, which is the relative error in approximating k_f in-

curred in the traditional theory, as

$$\varepsilon(\mathrm{LT}) = 1 - \frac{k_2^T(s=0;\mathrm{LT})}{k_f} \,. \tag{4.11}$$

This term will be used in expressions discussed below.

4.1.2 Mitrovica et al. [2005] formulation

Mitrovica et al. [2005] replaced the approximation to k_f adopted in the traditional theory with the following expression for the observed fluid Love number:

$$k_f = k_2^T(s=0;\mathrm{LT}=0) + k_{ee} \,. \tag{4.12}$$

This expression is comprised of two terms. The first, $k_2^T(s=0;\mathrm{LT}=0)$, represents the hydrostatic form of the planet; that is, it represents the form established in a rotating planet after all viscoelastic relaxation has been completed. The second term, k_{ee}, is the excess ellipticity of the planet. This term is due to any processes that give rise to non-hydrostatic ellipticity, and, in the Earth, it is estimated to be ~ 0.01, or about 1% of the hydrostatic form [Chambat et al., 2010]. The expression adopted by Mitrovica et al. [2005] ties the parameter k_f to the observed value, but takes into account that the Love numbers are only computed using a first-order accurate theory.

Using equation (4.12) in the linearised Liouville equation, and inverting the result into the time domain yields [Mitrovica & Wahr, 2011] (see also Appendix A)

$$\mathbf{m}(t) = \frac{\Omega}{A\sigma_0}\frac{1}{\beta(\varepsilon,\mathrm{LT})}\left[\mathbf{I}^L(t)D_1 + \sum_{k=1}^{K} E_k' \left(\mathbf{I}^L(t) * e^{-\kappa_k t}\right)\right], \tag{4.13}$$

where D_1 is as before (equation 4.8), and

$$E'_k \equiv \frac{l_s(\mathrm{LT})\prod_{i=1}^{K}(s_i-\kappa_k)+\kappa_k\sum_{j=1}^{K}\frac{r'_j}{s_j}\prod_{\substack{i=1\\ i\neq j}}^{K}(s_i-\kappa_k)}{\prod_{\substack{i=1\\ i\neq k}}^{K}(\kappa_i-\kappa_k)}. \tag{4.14}$$

The decay times, κ_k, are solutions of the polynomial

$$\prod_{i=1}^{K}(s+\kappa_i)=\frac{1}{\beta(\varepsilon,\mathrm{LT})}\left[\varepsilon(\mathrm{LT})\frac{k_2^T(s=0;\mathrm{LT})}{\sum_{k=1}^{K}\frac{r''_k}{s_k}}\prod_{i=1}^{K}(s+s_i)+(1-\varepsilon(\mathrm{LT}))\,s\prod_{i=1}^{K-1}(s+\lambda_i)\right], \tag{4.15}$$

where

$$\frac{1}{\beta(\varepsilon,\mathrm{LT})}=\frac{1}{1-\varepsilon(\mathrm{LT})+\varepsilon(\mathrm{LT})\frac{k_2^T(s=0;\mathrm{LT})}{\sum_{k=1}^{K}\frac{r''_k}{s_k}}}. \tag{4.16}$$

Now, from equation (4.11), equation (4.13) should collapse to equation (4.7) if we set $\varepsilon(\mathrm{LT}) = 0$ in the latter equation (that is, if we approximate the observed fluid Love number by $k_2^T(s = 0;\mathrm{LT})$, as in Wu & Peltier [1984]). Setting $\varepsilon(\mathrm{LT}) = 0$ in the polynomial (4.15) yields

$$\prod_{i=1}^{K}(s+\kappa_i)=s\prod_{i=1}^{K-1}(s+\lambda_i). \tag{4.17}$$

This equation implies that $\kappa_i = \lambda_i$ for $k = 1\cdots K-1$, and using this in equation (4.14) yields $E_k = E'_k$ for $k = 1\cdots K-1$. Equation (4.17) also implies that $\kappa_K = 0$, and in this case equation (4.14) yields $E'_K = D_2$. Thus, setting $\kappa_K = 0$ and $E'_K = D_2$ in the K^{th} term in the convolution of equation (4.13) yields an expression identical to the D_2 term in equation (4.7). Thus, equations (4.7)–(4.10) represent a special case of equations (4.13)–(4.14) when one assumes that $\varepsilon(\mathrm{LT}) = 0$.

Since $\beta(\varepsilon,\mathrm{LT})$ is very close to unity (the departure is of order 0.01), a comparison of equa-

tions (4.13) and (4.7) indicates that the elastic response of the rotation vector is essentially the same in both theoretical formulations of TPW. In contrast, the unidirectional-TPW physics highlighted by Wu & Peltier [1984], i.e., the physics embodied by the D_2 term in equation (4.7), disappears in the more accurate theory; this term is an artefact of the approximation $\varepsilon(\mathrm{LT}) = 0$ adopted by Wu & Peltier [1984]. The approximation has the effect of setting the inverse decay time of one of the rotational normal modes to zero, thus yielding a permanent displacement of the pole from its initial position even if the surface mass load returns to its initial state. Finally, we note that the remaining set of $K - 1$ decay times and modal amplitudes are also impacted by the same approximation, and the error introduced by the approximation will be explored in numerical results discussed below.

4.2 Unidirectional TPW Revisited

In this section, we provide a physical explanation for the presence of the unidirectional-TPW term in equation (4.7), as well as its disappearance in the revised rotational stability theory (equation 4.13). We also provide an argument for the mathematical form of this term.

4.2.1 Physical Interpretation

We begin with a short summary of the physics of TPW as embodied in equations (4.7) and (4.13). (A more comprehensive discussion of this physics may be found in Mitrovica et al. [2005] and Mitrovica & Wahr [2011].)

The physics associated with traditional and revised rotation theories may be understood with reference to the schematic illustration in Figure 4.1. The first row represents the physics embodied in the traditional rotational stability theory. A planet, initially at rest, is spun up to the present rotation rate, and an equilibrium form is eventually established (Figure 4.1A1). Some time later, a load is applied (Figure 4.1A2). Application of the load causes the pole to tip away from the load;

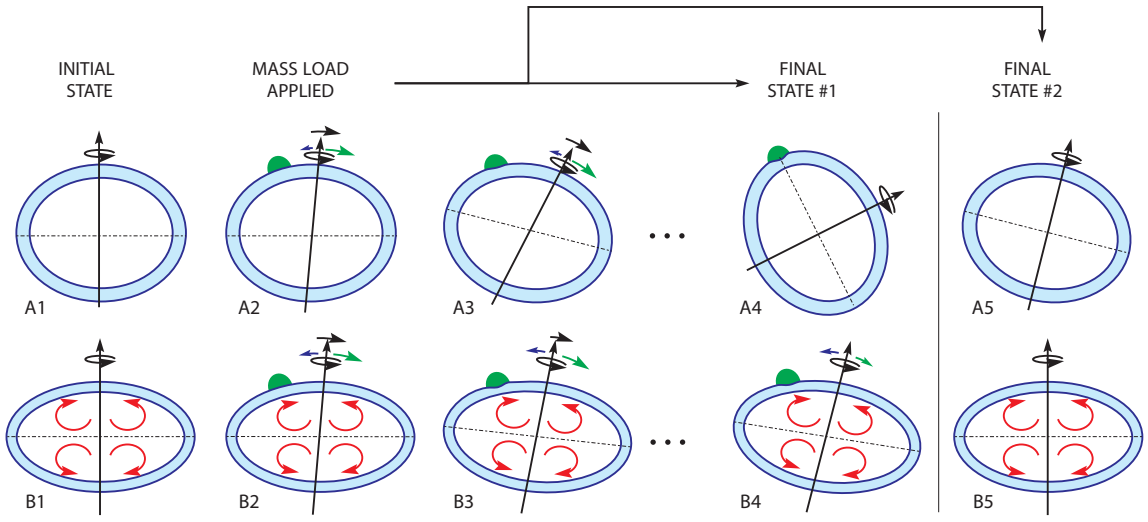

Figure 4.1: Schematic illustrating the traditional (A1 - A5) and revised rotational stability theories (B1 - B5). Both planets have an elastic lithosphere (shaded blue regions). However, the lithosphere in A1 was spun-up from a perfect sphere (and is thus stressed), while the lithosphere in B1 has a hydrostatic form (i.e., is unstressed). A mass load is represented by the green dot, and its associated forcing on the rotation axis is shown by a green arrow. The resistance generated by the planetary bulge is represented by a blue arrow. The red circular arrows in the planetary interior represent mantle convection that drives an excess ellipticity in the planetary form.

that is, the load is moved towards the equator. This polar motion will be initially resisted by the rotational bulge, but the resistance is transient. Eventually, the bulge will reorient itself perfectly to the rotation vector, and the pole is free to tip further from the load (Figure 4.1A3). This sequence will continue until the load reaches the equator (Figure 4.1A4). The important point to note is that the same Earth model is used to compute both the background oblateness and the viscoelastic response to surface mass loading and the perturbed centrifugal potential (i.e., $\epsilon(\mathrm{LT}) = 0$ in equation (4.11)). Therefore, the bulge can reorient itself perfectly to the new rotational state. In this regard, the system loses all memory of its initial orientation.

Next, consider the revised rotation theory, in which the background form of the planet is hydrostatic (rather than the equilibrium form of Figure 4.1A1) with an additional excess ellipticity (Figure 4.1B1). Upon loading, the pole migrates away from the load (i.e., the load moves towards the

equator), and the rotational bulge once again resists this motion. However, in this case, the bulge cannot adjust perfectly to the new orientation. This is because the perturbed centrifugal potential associated with TPW sees an Earth that, on ice-age timescales, has an effectively elastic lithosphere. Therefore, as the pole moves, the originally unstressed lithosphere will become stressed, and will exert a restoring force on the rotation vector. In addition, the excess ellipticity, since it is stationary on ice-age timescales, will also prevent the bulge from adjusting perfectly to any new orientation of the pole. Consequently, the reorientation of the bulge will be incomplete and, after a sequence of such steps, a final state will be reached (Figure 4.1B4) in which the forcing associated with the load will be balanced by the resistance associated with both the stressed lithosphere and the excess ellipticity. The load will not reach the equator.

Finally, consider what would happen if, at some time equivalent to the third column on Figure 4.1, the load was removed. The traditional theory predicts that long after the load's removal (i.e., jumping from Figure 4.1A3 to the final, unloaded state given by Figure 4.1A5) the pole will not return to its initial orientation. As discussed above, since the bulge adjusts (perfectly) to the new orientation of the pole, any memory of the pole's initial orientation is lost. The net displacement of the pole from its initial state (Figure 4.1A5) is a reflection of this residual memory loss. In contrast, in the revised theory (Figure 4.1B), the system retains memory of its original rotational state, and the final unloaded state (Figure 4.1B5) is the same as this initial state. The final displacement of the pole from its initial position in Figure 4.1A5, even after the load returns to its initial state, represents the unidirectional TPW predicted by the traditional rotational stability theory (the term in D_2 in equation 4.7). The disappearance of this term in the revised theory (equation 4.13) is, in this regard, reflected by the return of the pole to its initial state in Figure 4.1B5. Thus, unidirectional TPW represents an integrated measure of the planet's loss of memory of its initial rotational state through bulge adjustment, as modelled by the traditional rotational stability theory. Since the planet retains a memory of its original rotational state in the more accurate, revised stability theory, the unidirectional-TPW term disappears in this theoretical treatment. In the next

section, we move from this physical explanation to a brief discussion of the mathematical form of the unidirectional-TPW term.

4.2.2 Some Mathematical Insight

The unidirectional-TPW term in equation (4.7) can be thought of as a product of a term involving the decay times of the deformational and rotational normal modes, the parameter $l_s(\mathrm{LT})$, and the time-integrated perturbation of inertia tensor elements. We will consider each of these in turn, beginning with the second.

The total inertia tensor perturbation due to surface mass loading plus any isostatic compensation (i.e., the forcing that drives TPW) is given by

$$\mathbf{I}^L(t) + k_2^L(t) * \mathbf{I}^L(t) \,, \tag{4.18}$$

where the time domain form of the viscoelastic surface-load Love number, k_2^L, is given by

$$k_2^L(t) = k_2^{L,E}\delta(t) + \sum_{k=1}^{K} r_k' e^{-s_k t} \,. \tag{4.19}$$

The expression (4.18) is simply the time domain form of the numerator of the Liouville equation (4.1).

Let us consider the total perturbation in the inertia tensor elements arising from the application of a load at time t_0. In this case, $\mathbf{I}^L(t) = \mathbf{I}^L H(t-t_0)$, where H is the Heaviside step function. Using this expression in (4.18) yields

$$\mathbf{I}^L H(t-t_0)\left[1 + k_2^{L,E} + \sum_{k=1}^{K} \frac{r_k'}{s_k}\left(1 - e^{-s_k(t-t_0)}\right)\right] \,. \tag{4.20}$$

Now, if this load is removed at time t_1, then the full time history of the loading may be written as $\mathbf{I}^L(t) = \mathbf{I}^L H(t-t_0) - \mathbf{I}^L H(t-t_1)$. Next, we ask: What is the integrated perturbation to the inertia el-

ement a very long time after the load is removed? Using expression (4.20), this integrated forcing is, at time t_∞,

$$\begin{aligned}
&\mathbf{I}^L \int_{t_0}^{t_\infty} \left[1 + k_2^{L,E} + \sum_{k=1}^{K} \frac{r'_k}{s_k}\left(1 - e^{-s_k(t-t_0)}\right)\right] dt \\
&\qquad\qquad - \mathbf{I}^L \int_{t_1}^{t_\infty} \left[1 + k_2^{L,E} + \sum_{k=1}^{K} \frac{r'_k}{s_k}\left(1 - e^{-s_k(t-t_1)}\right)\right] dt \\
&= \mathbf{I}^L \int_{t_0}^{t_\infty} \left[1 + k_2^{L}(s=0;\mathrm{LT}) - \sum_{k=1}^{K} \frac{r'_k}{s_k} e^{-s_k(t-t_0)}\right] dt \\
&\qquad\qquad - \mathbf{I}^L \int_{t_1}^{t_\infty} \left[1 + k_2^{L}(s=0;\mathrm{LT}) - \sum_{k=1}^{K} \frac{r'_k}{s_k} e^{-s_k(t-t_1)}\right] dt \\
&= \mathbf{I}^L \int_{t_0}^{t_\infty} \left[l_s - \sum_{k=1}^{K} \frac{r'_k}{s_k} e^{-s_k(t-t_0)}\right] dt - \mathbf{I}^L \int_{t_1}^{t_\infty} \left[l_s - \sum_{k=1}^{K} \frac{r'_k}{s_k} e^{-s_k(t-t_1)}\right] dt \\
&= l_s(t_1 - t_0)\mathbf{I}^L = l_s \int_0^{t_\infty} \mathbf{I}^L \left[H(t-t_0) - H(t-t_1)\right] dt \,, \qquad (4.21)
\end{aligned}$$

where we have used equations (4.2) to (4.4) for the substitution with l_s.

We conclude that the integrated perturbation to the inertia tensor elements long after the unloading — that is, the integrated forcing on the rotation pole — is not zero, as one might have expected, unless the lithosphere has no elastic strength, in which case $l_s = 0$, or in the trivial case where the load is removed the instant it is applied (i.e., $t_0 = t_1$). The integrated forcing at t_∞ is non-zero because of an imbalance between the integrated load (plus compensation) forcing that drives TPW during the period of loading ($t_0 < t < t_1$) and during the period subsequent to loading ($t > t_1$). The magnitude of this net forcing is proportional to l_s, which is proportional to the thickness of the elastic lithosphere. The final expression in equation (4.21) includes all parameters in the expression for the unidirectional TPW in equation (4.7) with the exception of the ratio $\prod_{k=1}^{K} s_k / \prod_{k=1}^{K-1} \lambda_k$. We next turn to a discussion of this factor.

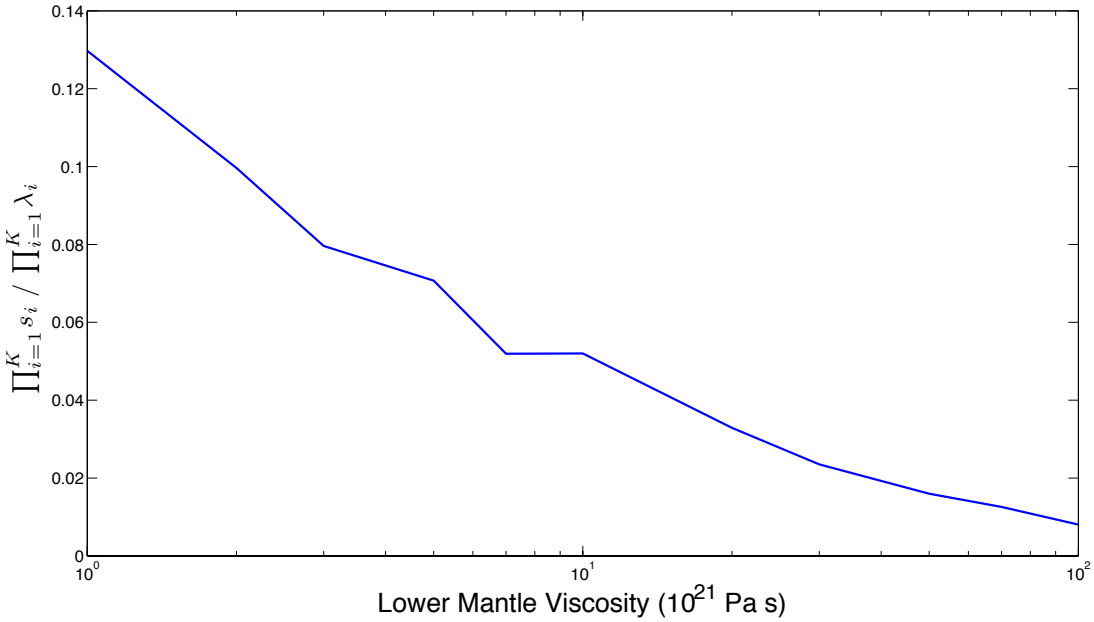

Figure 4.2: Plot of the ratio in D_2, $\prod_{k=1}^{K} s_k / \prod_{k=1}^{K-1} \lambda_k$, as a function of lower mantle viscosity. For this calculation we adopt an Earth model with a 30-layer volume-averaged version of PREM, an elastic lithosphere of thickness 80 km, and an upper mantle viscosity of 5×10^{20} Pa s.

The inverse decay times s_k govern the adjustment timescale of the rotational bulge. Since the bulge provides resistance to TPW, longer decay times (i.e., smaller s_k) will hinder TPW. One might ask, however, what qualifies as long? Generally, if the adjustment of the bulge is significantly slower than the adjustment of the pole (i.e., if $\prod_{k=1}^{K} s_k \ll \prod_{k=1}^{K-1} \lambda_k$), TPW will be hindered. If the converse is true (i.e., if the bulge relaxes much quicker than the adjustment of the pole), TPW will be efficiently excited. Hence the appearance of the ratio $\prod_{k=1}^{K} s_k / \prod_{k=1}^{K-1} \lambda_k$ in the term governing unidirectional TPW.

This physical argument, however, does not provide insight into the sensitivity of the parameter D_2 to mantle viscosity. If one increases the mantle viscosity, the inverse decay times governing both the bulge adjustment and polar motion will decrease (i.e., the decay times will increase). However, it is unclear whether the numerator or denominator will decrease more rapidly. We explore this in Figure 4.2, which shows a plot of $\prod_{k=1}^{K} s_k / \prod_{k=1}^{K-1} \lambda_k$ as a function of lower mantle

viscosity of the adopted viscoelastic Earth model. The prediction indicates that, while the decay times governing polar motion and bulge adjustment will both increase as the lower mantle is stiffened, the latter will increase more quickly than the former. The net effect is that unidirectional TPW predicted by the traditional rotational stability theory [Wu & Peltier, 1984] will diminish as the lower mantle viscosity is increased.

4.3 Numerical Results

We next return to the more general issue of the magnitude of the net displacement of the rotation axis driven by ice-age loading. As discussed in the Introduction to this chapter, numerical predictions based on the traditional rotational stability theory [e.g. Sabadini et al., 1982, 1983; Wu & Peltier, 1984; Vermeersen et al., 1997; Mitrovica et al., 2001] are characterised by a relatively large drift of the rotation axis during ice-age loading, and this drift has been suggested as a driving mechanism for the Earth's transition out of the ice age [Sabadini et al., 1982, 1983]. The drift of the pole is due both to the unidirectional-TPW term in the traditional rotational stability theory, and to rotational normal modes with decay times sufficiently short that the mode is non-negligibly excited by a typical glacial cycle whilst sufficiently long that this excitation persists well after the cycle has ended. While we have established that unidirectional TPW is an artefact of an approximation made in the traditional rotational ice-age theory associated with the Earth's background form, it remains unclear how improvements to the rotation theory impact previous predictions of the net shift of the pole. In this section, we address this issue by presenting numerical predictions of TPW over a suite of successively longer time periods extending from the Plio-Pleistocene to the Miocene. All calculations will be based on viscoelastic Earth models with elastic and density structure given by the Preliminary Reference Earth Model [Dziewonski & Anderson, 1981], an elastic lithosphere of thickness 120 km, and upper mantle viscosity below the lithosphere of 5×10^{20} Pa s. The lower mantle viscosity will serve as a free parameter of the modelling.

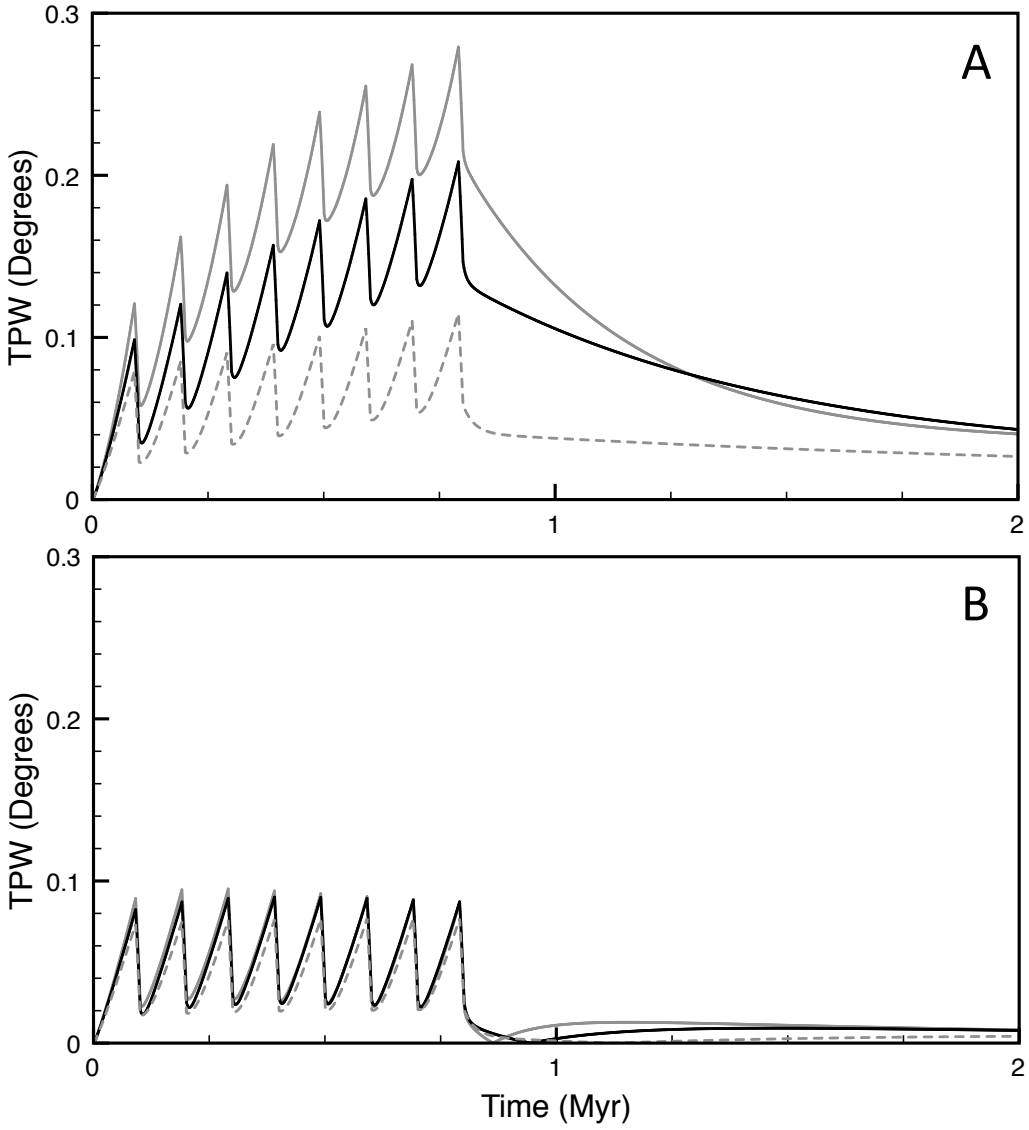

Figure 4.3: Prediction of TPW during and subsequent to a ice-age loading history characterised by eight cycles of 100-kyr duration (see text). (A) Predictions based on the traditional ice-age rotation theory [Wu & Peltier, 1984] distinguished on the basis of the adopted lower mantle viscosity: (solid grey line) 2×10^{21} Pa s; (solid black line) 5×10^{21} Pa s; and (dashed grey line) 2×10^{22} Pa s. (B) As in (A), except the revised ice-age rotation theory of Mitrovica et al. [2005] and Mitrovica & Wahr [2011] is adopted.

To begin, we consider the TPW response to a simple sawtooth loading history characterised by eight cycles, each with a 90 kyr glaciation phase in which the surface mass load increases linearly in volume, followed by a 10 kyr deglaciation with a linearly decreasing ice volume (Figure 4.3). Following Mitrovica & Milne [1998], we adopt peak inertia perturbations at each glacial maximum of $I_{13} = -6.67 \times 10^{31}$ kg m^{-2} and $I_{23} = 2.31 \times 10^{32}$ kg m^{-2}. These values are based on the ICE-3G deglaciation history [Tushingham & Peltier, 1991], and they incorporate inertia perturbations associated with a complementary, eustatic water load. The top and bottom frames of Figure 4.3 are based on the traditional [Wu & Peltier, 1984] and revised [Mitrovica et al., 2005] rotational stability theories, respectively, and on each frame we show simulations adopting three different values of lower mantle viscosity.

The net displacement of the pole predicted using the rotation theory of Wu & Peltier [1984] (Figure 4.3A) grows with each glacial cycle and, while this trend is gradually decreasing, the predictions have not yet converged to a steady state oscillation after eight cycles. The peak-to-trough amplitude of the TPW oscillation is relatively similar in all three simulations ($\sim 0.06°$), but the slow drift of the rotation axis superimposed on these oscillations is a function of the lower mantle viscosity. In particular, as the lower mantle viscosity is increased an order of magnitude, from 2×10^{21} Pa s to 2×10^{22} Pa s, the net displacement by the end of loading decreases by over 70%, from $0.22°$ to $0.06°$. This suggests that, with increasing lower mantle viscosity, the decay times of the rotational normal modes with slowest relaxation increase such that each 100-kyr glacial cycle excites these modes less efficiently. At the end of the eight cycles, each of the TPW curves decreases towards a final displacement, i.e., towards the unidirectional TPW value, that is unique to each simulation. We note that this monotonic decrease has a timescale that increases significantly with the lower mantle viscosity of the simulation. The unidirectional TPW value also decreases as the adopted lower mantle viscosity increases, as one would expect from Figure 4.2, but in all three cases this permanent displacement (not shown on the figure) is less than $0.04°$.

Figure 4.3B shows analogous results for the case where TPW is predicted using the revised

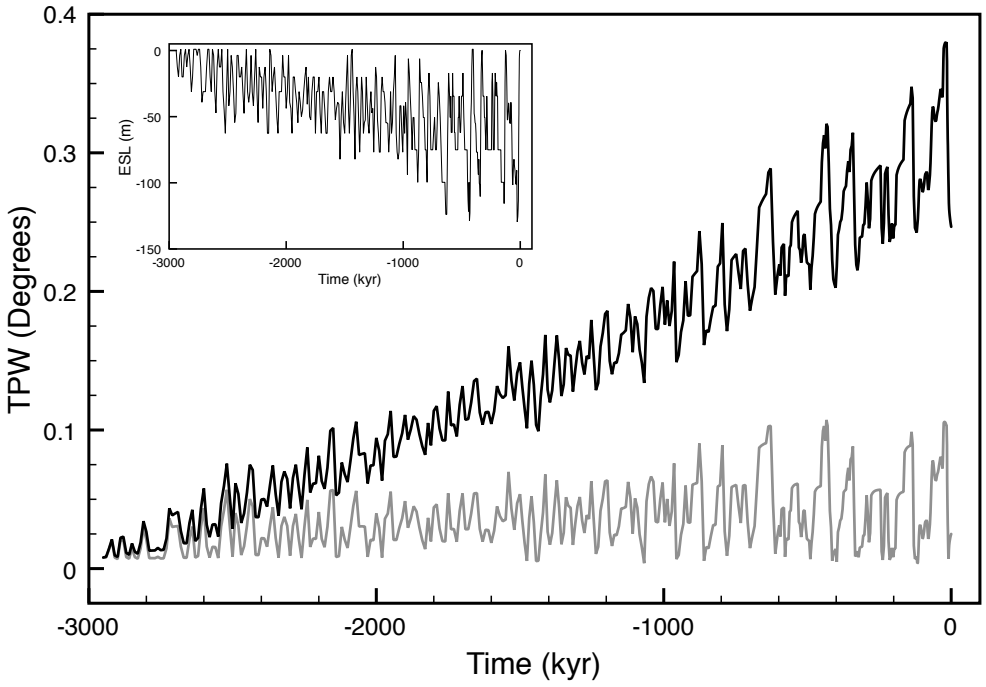

Figure 4.4: Prediction of TPW over the past 3 Myr based on the ice history constructed by Raymo et al. [2011]. The equivalent eustatic sea-level change associated with this ice history is shown in the inset of the figure. In the main frame, results are shown for simulations based on both the (black line) traditional [Wu & Peltier, 1984] and (grey line) revised [Mitrovica et al., 2005; Mitrovica & Wahr, 2011] rotational stability theories. The calculations adopt an Earth model with a lower mantle viscosity of 5×10^{21} Pa s, and include a gravitationally self-consistent sea-level change.

rotational stability theory. While the amplitude of the TPW oscillation across each glacial cycle remains similar to the simulations in Figure 4.3A, the net displacement after the eight loading cycles is small ($\sim 0.02^{\circ}$) and insensitive to the adopted mantle viscosity [see also Nakada, 2002]. We have also verified that in all three simulations the pole ultimately returns to its initial position a long time after the loading ends.

In Figure 4.4 we extend our TPW analysis to consider ice-age loading since the end of the mid-Pliocene climate optimum, at ~ 3 Ma. Details regarding the construction of the ice history in this case may be found in Raymo et al. [2011]. The globally-averaged (eustatic) sea-level change asso-

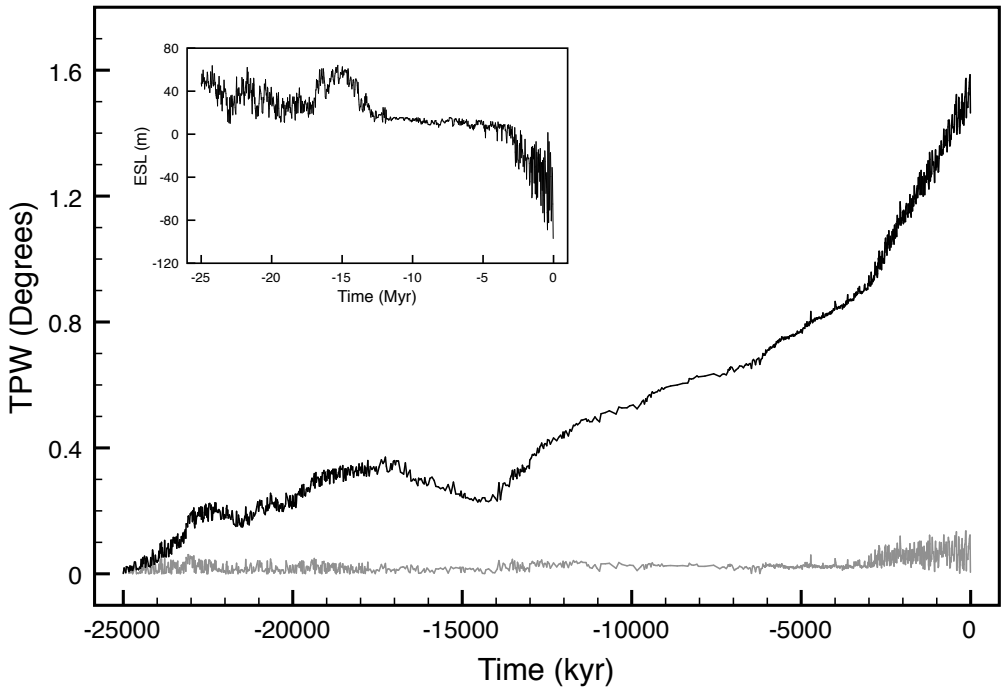

Figure 4.5: Prediction of TPW over the past 25 Myr based on the ice history constructed by Morrow et al. [2012], after de Boer et al. [2010]. The equivalent eustatic sea-level change associated with this ice history is shown in the inset of the figure. In the main frame, results are shown for simulations based on both the (black line) traditional [Wu & Peltier, 1984] and (grey line) revised [Mitrovica et al., 2005; Mitrovica & Wahr, 2011] rotational stability theories. The calculations adopt an Earth model with a lower mantle viscosity of 5×10^{21} Pa s, and include a globally-uniform sea-level change.

ciated with this ice history is shown in the inset to Figure 4.4, where one may note a progressive increase in peak ice volumes with time, as well as the well known transition from a periodicity of 40 kyr to 100 kyr in the ice-age cycles circa 800 ka. The Earth model adopted in the simulation is characterised by a lower mantle viscosity of 5×10^{21} Pa s, and a calculation based on the rotational stability theory of Wu & Peltier [1984] shows a significant long-term drift in the pole position that reaches $\sim 0.3^{\circ}$ at present day. In contrast, a calculation based on the revised rotation theory that more accurately accounts for the Earth's background ellipticity [Mitrovica et al., 2005; Mitrovica & Wahr, 2011] is characterised by a variability that reflects the ice-age loading history but with no

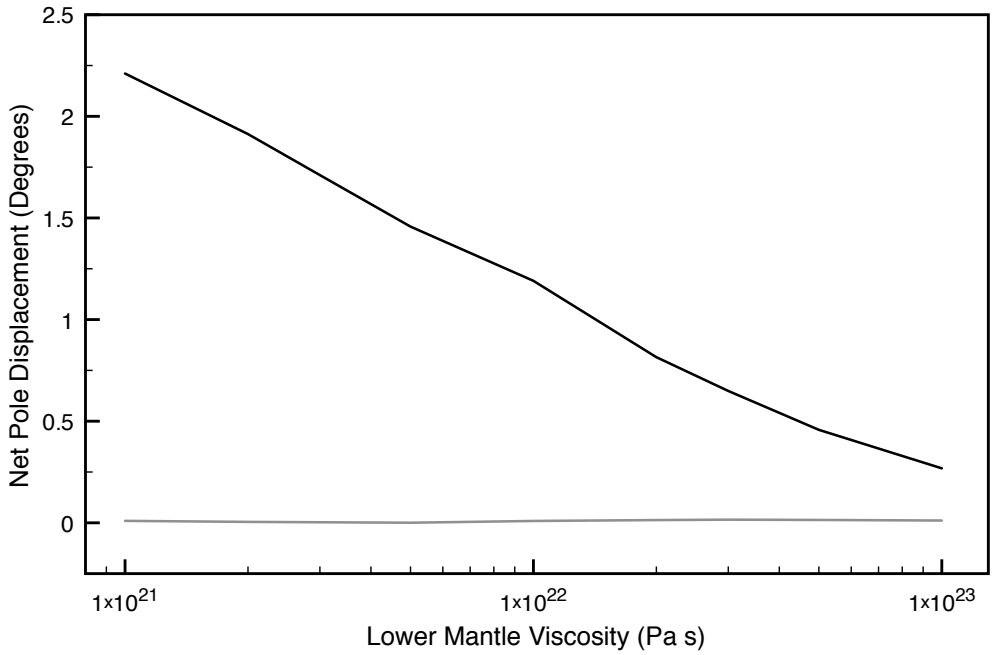

Figure 4.6: Predicted net TPW over the past 25 Myr based on the simulation for this time period described in the text (see also Figure 4.5) as a function of the lower mantle viscosity adopted in the simulation. Results are shown for simulations based on both the (black line) traditional [Wu & Peltier, 1984] and (grey line) revised [Mitrovica et al., 2005; Mitrovica & Wahr, 2011] rotational stability theories.

long-term drift in the pole position.

Finally, we predict TPW over the last 25 Myr driven by an ice history constructed by Morrow et al. [2012] (Figure 4.5). This history is based on a time series of global ice volume inferred using a set of one dimensional ice sheet models that were constrained, in an inverse procedure, from observed benthic δ^{18}O records [de Boer et al., 2010]. The inset of Figure 4.5 shows the eustatic sea-level variation across the Neogene associated with the ice history. This time series suggests that ice volumes reached present levels only after the mid-Pliocene climate optimum, with the first $\sim$ 12 Myr of the time series characterised by significantly smaller polar ice cover than at present day. The net displacement of the pole reaches $\sim 1.6^\circ$ over the 25-Myr time window when the traditional TPW theory of Wu & Peltier [1984] is adopted and the lower mantle viscosity is 5×10^{21} Pa s. This net displacement is sensitive to the viscosity (Figure 4.6): indeed, decreasing

the lower mantle viscosity from 10^{23} Pa s to 10^{21} Pa s leads to a monotonic increase in the net TPW from 0.3° to 2.2°. As in our earlier simulations, adopting the revised rotation theory of Mitrovica et al. [2005] effectively removes this background drift in the pole position, which, for the same set of models, remains less than 0.1°.

4.4 Final Remarks

Previous studies, based on a longstanding theoretical treatment of the rotational stability of an ice-age Earth [Sabadini & Peltier, 1981; Wu & Peltier, 1984], have argued that a predicted long-term drift in the orientation of the rotation axis (of order several degrees) may be responsible for transitioning the Earth system out of the ice age [Sabadini et al., 1982, 1983]. Recent advances in Earth rotation theory [Mitrovica et al., 2005; Cambiotti et al., 2010; Mitrovica & Wahr, 2011], motivated by the pioneering study of Nakada [2002], have demonstrated that these traditional treatments of TPW have underestimated the background ellipticity of the Earth's figure and, therefore, the stability of the rotation axis. We have noted that the revised theories do not include the permanent shift in the orientation of the rotation axis, known as unidirectional TPW, that is predicted by the traditional treatments of ice-age Earth rotation. We have also developed the first physical and mathematical framework for understanding both the appearance of this term in the traditional rotation theory and its absence in the more accurate, revised theory. Furthermore, we have adopted the latter theory to predict ice-age-induced TPW over successively longer time intervals, including the last 1 Myr, 3 Myr, and 25 Myr. We find that the long-term drift of the rotation axis predicted in previous studies disappears when using the revised theory, and thus the factors that drove the Earth system out of the last ice age must be sought elsewhere.

Tall trees catch the gales.

Chinese proverb

5

Time-Dependent Rotational Stability of Terrestrial Planets

5.1 Introduction

Redistributions of mass on a planet, whether driven by internal processes such as thermochemical convection, external processes such as the growth and ablation of ice sheets, or some combination of the two (e.g., volcanism), will drive reorientations of the rotation axis relative to the surface geography over a broad spectrum of timescales. Long-term, secular components of this reorientation are known as true polar wander (henceforth, TPW).

The analysis of the rotational stability of terrestrial planets, and in particular TPW, is a classic problem that dates, in the geophysical literature, to the canonical mid-20$^{\text{th}}$-century study of Gold [1955]. Gold's conceptual model of load-induced TPW is illustrated schematically in Figure 5.1A.

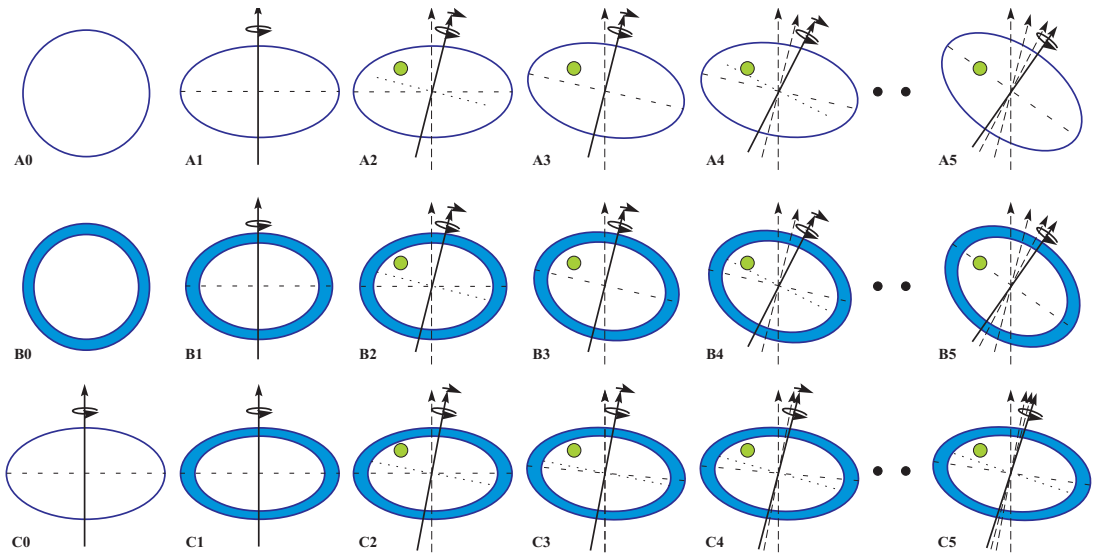

Figure 5.1: Schematic illustration of the physics of TPW. The green disk represents an internal load, the solid-blue outer shell is an elastic lithosphere, the solid arrow (with spin and TPW directions specified near the tip) is the rotation vector, and the long-dashed arrows are previous rotation vectors within the same series. On each frame, the short-dashed line within the interior of the model planet denotes the plane of the rotational bulge, while the dotted line is the rotational equator (i.e., 90° from the contemporaneous rotation axis). Rows (A) and (B) treat cases where the rotational bulge can ultimately relax perfectly to any change in the orientation of the rotation axis (whenever this occurs, the axis of the bulge and the equator, denoted by the short-dashed and dotted lines, respectively, will coincide). In this case, which is the scenario discussed by Gold [1955], an equilibrium theory predicts that TPW will ultimately reorient the load to the equator (frames A5 or B5). Row (C) shows the case where the initial state is hydrostatic, but where any readjustment of the bulge will introduce elastic stresses in the (initially unstressed) lithosphere. In this case, the rotational bulge cannot adjust perfectly to a change in the orientation of the rotation axis, and the final position of the load will not be the equator (frame C5). This final state is predicted by the equilibrium theory of Matsuyama et al. [2006] (see equation 5.28) and it is governed by a balance between the load-induced forcing and the resistance provided by the elastic lithosphere (the latter stabilisation is termed the 'remnant bulge'; see also Willemann [1984]). The schematics in the figure are shown in a reference frame fixed to the location on the load. While the figure presents the case of an internal loading, the same physics applies to external loads; however, in this case the no-lithosphere scenario shown in row A must assume that the surface mass load is never fully compensated.

We begin with a rotating planet whose gravitational figure has fully relaxed to an imposed centrifugal potential, i.e., a planet with a hydrostatic figure (Figure 5.1A1). If the planet is subject to a positive load, then the load will be thrown outwards toward the equator, or, for an observer fixed to the planet, the pole will migrate (or wander) away from the load (Figure 5.1A2). This wander will be opposed by the rotational bulge, since it represents an excess mass that will resist displacement off the equator. However, Gold [1955] argued that this resistance is transient, since the Earth will viscously deform in response to the perturbed centrifugal potential so as to bring the bulge back onto the equator (Figure 5.1A3). Once this adjustment takes place, the load is free to move farther away from the rotation axis and the process will continue in incremental steps (Figure 5.1A4) until the load has reached the equator (Figure 5.1A5). In the conceptual model of Gold [1955], planetary rotation is inherently unstable because a load of any size will ultimately migrate to the equator.

We can extend these ideas to the hypothetical case of a planet with an elastic lithosphere, the initial figure of which is not hydrostatic (Figure 5.1B1). This case is consistent with a non-rotating, spherical planet (Figure 5.1B0) with an elastic lithosphere that is spun up to a final form in which all viscous stresses have relaxed. As in Figure 5.1A2, loading this planet will drive TPW, and this polar motion will meet transient resistance from a rotational bulge that will ultimately reorient perfectly to any new rotational state (Figure 5.1B3). The process will continue and, once again, the load will reach the equator (Figure 5.1B5). The key point in Figures 5.1A and 5.1B is that the rotation axis is inherently unstable whenever the rotational bulge can relax so that the initial form of the planet is re-established around the new rotational state, whether this initial form is hydrostatic or not. In this case, in the terminology of Gold [1955], the rotating planet is said to lose all memory of previous rotational states.

Goldreich & Toomre [1969] provided a theoretical framework for the conceptual model of Gold [1955] and considered rotational stability in the case of multiple loads. They demonstrated, for slow changes in the shape of a quasi-rigid body, that the angle between the angular momen-

tum vector and the principal axes is an adiabatic invariant. In the context of TPW, this invariance means that the rotation axis will remain aligned with the principal axis of inertia whenever changes in the shape of the planet are slow.

It is important to note that Gold's conceptual model predicts the final orientation of the rotation axis (i.e., Figures 5.1A5, 5.1B5), but not the timescale of TPW (i.e., Figures 5.1A1–A4, Figures 5.1B1–B4). A variety of methodologies have been developed within the geophysical literature to estimate the time dependence of TPW driven by mantle convection, including both nonlinear [Ricard et al., 1993; Steinberger & O'Connell, 2002; Tsai & Stevenson, 2007] and linearised [Chan et al., 2011a; Cambiotti et al., 2011] treatments of the governing equations. Ricard et al. [1993] made use of the adiabatic invariance described by Goldreich & Toomre [1969] and incorporated perturbations in the moment of inertia tensor associated with: (i) time-dependent mass redistribution, including boundary deformations, associated with internal convective forcing, and (ii) the time-dependent, viscous response of the rotational bulge to the perturbed centrifugal potential. They expressed the latter contribution in terms of a long-timescale, asymptotic expansion of the viscoelastic tidal Love number at spherical harmonic degree 2.

The conceptual model of Gold [1955] was extended by Willemann [1984] [see also Matsuyama et al., 2006] to incorporate stabilisation associated with an elastic lithosphere, as illustrated in Figure 5.1C. Consider an initially hydrostatic planet characterised by an unstressed elastic lithosphere (Figure 5.1C1). This situation may arise in several ways. First, an elastic lithosphere may gradually cool out of a proto-planet that, at least initially, had no lithosphere. In this case, the creation of an unstressed elastic lid would not alter the gravitational figure of the planet (i.e., the evolution from Figure 5.1C0 to C1). Alternatively, one can imagine a planet with a rotation vector that has been stable over a timescale long enough that the viscous stresses in even a high-viscosity lithosphere would have relaxed. The planets in Figure 5.1B1 and Figure 5.1C1 have the same rotation rate; the important distinction between them is that the lithosphere in the former is stressed in the pre-loaded state and, as a consequence, the gravitational figure of the planet is not hydrostatic. As

discussed by Willemann [1984] and Matsuyama et al. [2006], the distinction has profound implications for rotational stability [see also Daradich et al., 2008].

Consider a scenario in which the planet in Figure 5.1C1 is subject to a load. As before, the pole will move away from the load, the rotational bulge will act to resist this motion, and this resistance will gradually weaken as the rotational bulge readjusts to the new orientation of the rotation axis. However, in contrast to the previous scenarios, elastic stresses induced in the lithosphere by TPW will prevent the rotational bulge from adjusting perfectly to the new rotational state. That is, the rotational bulge remains misaligned with the geographic equator in Figure 5.1C3. Nevertheless, the (imperfect) adjustment of the rotational bulge will permit further TPW and the process will continue until elastic stresses in the lithosphere balance the forcing associated with the load (Figure 5.1C5). In this case, the final position of the load will not be the equator. The stabilisation associated with TPW-induced elastic stresses is known as the 'remnant bulge' [Willemann, 1984] (Figure 5.1C5).

Willemann [1984] concluded that the remnant bulge stabilisation is independent of the elastic thickness of the lithosphere. An extension and minor correction of his derivation by Matsuyama et al. [2006] demonstrated, in contrast, that the magnitude of TPW would be dependent on the lithospheric thickness; however, this dependence is only significant for planets with relatively thin lithospheres. As in Gold [1955] and Goldreich & Toomre [1969], Willemann [1984] and Matsuyama et al. [2006] were concerned with equilibrium theories that predicted the final state of the rotation axis in response to a loading.

Chan et al. [2011a] derived a linearised (valid for small-amplitude TPW), time-dependent treatment of convection-driven TPW that incorporated stabilisation by both the remnant bulge and the delayed viscous adjustment of the rotational bulge. In this paper, we derive a non-linear, time-dependent rotational stability theory that incorporates both of these stabilisation mechanisms. In our derivation, the first of these stabilisation mechanisms is incorporated using the method first outlined by Ricard et al. [1993]. The derivation is valid for both internal and external loading, and

we will describe the modifications necessary to move from one application to the other. In this regard, one might interpret this manuscript as either an extension of the Ricard et al. [1993] study to incorporate remnant bulge stabilisation, or an extension of the equilibrium theory of Matsuyama et al. [2006] to treat time-dependent rotational stability. A preliminary discussion of this extended theory, in which the governing equation was provided without derivation, may be found in Creveling et al. [2012].

In the next section, we begin with a detailed mathematical derivation of the governing equations. Following this, we present a series of illustrative numerical simulations that adopt model parameters consistent with the Earth and Mars. Recent finite element modelling has shown that the Earth's broken lithosphere has an effective elastic thickness more than an order of magnitude smaller than the mean plate thickness when considering its impact on rotational stability [Creveling et al., 2012]. In the simulations described below, we generally adopt a lithospheric thickness of 15 km, which is above the upper bound of 10 km suggested by Creveling et al. [2012]; however, to illustrate the physics of the stabilisation we consider the sensitivity of the results to variations in this parameter over the range of 5–25 km. The scenario in Figure 5.1C1 is more directly appropriate for Mars, which has an elastic lithosphere with a thickness of several hundred kilometres, but a form that is very close to hydrostatic [Daradich et al., 2008].

5.2 Mathematical Formulation

5.2.1 Conservation of Angular Momentum: Euler Equation

In a rigid body subject to no external torques, angular momentum is conserved and time variations in the angular velocity vector, ω, are governed by the standard Euler equation,

$$\frac{dL}{dt} + \omega \times L = 0 \,, \tag{5.1}$$

where L is the angular momentum vector. The first term on the left-hand side of equation (5.1) represents the change of L as measured by an observer fixed to the rotating body, while the sum of the two terms is the change measured by an observer in inertial space. When the body is deformable, the moment of inertia tensor, $\mathbf{I}$, becomes variable in time, such that $L(t) = \mathbf{I}(t) \cdot \omega(t)$. In this case, if the coordinate system is chosen to coincide with the instantaneous principle axes of $\mathbf{I}(t)$, equation (5.1) generalises into the so-called Liouville equation.

In geophysical applications, the broad spectrum of time variability in both $\mathbf{I}$ and ω makes it challenging, in general, to solve the non-linear Liouville equation. As a consequence, problems involving timescales much longer than a year have been solved using various approximations. For example, in the case where perturbations to both $\mathbf{I}$ and ω are relatively small, the Euler equation can be linearised around an initial state. This approach has been the standard methodology in predicting perturbations in Earth rotation driven by ice-age loading, where TPW is of order 1° or less [Sabadini & Peltier, 1981; Wu & Peltier, 1984; Mitrovica et al., 2005]. In this regard, Mitrovica et al. [2005] demonstrated that traditional ice-age formulations [Sabadini & Peltier, 1981; Wu & Peltier, 1984; Mitrovica & Milne, 1998] introduced significant error in predicting TPW by ignoring stabilisation associated with both the remnant bulge (Figure 5.1C) and long-term (relative to ice-age timescales) excess ellipticity of the Earth's figure.

Chan et al. [2011a] extended the linearised Mitrovica et al. [2005] formulation to consider TPW driven by mantle convection; they argued that the error incurred in such predictions is only $\sim$ 10%–20% when TPW of $\sim 40^\circ$ is driven by internal convective forcing concentrated at mid-latitudes. The Chan et al. [2011a] stability theory incorporates stabilisation associated with both the delayed, viscoelastic adjustment of the rotational bulge and elastic strength in the lithosphere (i.e., the remnant bulge).

A variety of other methodologies have been developed to model convection-driven TPW [Ricard et al., 1993; Steinberger & O'Connell, 2002; Tsai & Stevenson, 2007]. Of particular interest here is the Ricard et al. [1993] approach, which has commonly been adopted within the mantle

convection community [e.g. Richards et al., 1999]. Their treatment solves equation (5.1) under the assumption of very long timescale forcing and includes stabilisation due to delayed adjustment of the bulge (but not the remnant bulge); in this (very long timescale) case, the governing equation reduces to an eigenvalue problem [Gold, 1955; Lefftz, 1991; Ricard et al., 1993]:

$$\mathbf{I}\,\omega = \lambda\,\omega\,. \tag{5.2}$$

In this case, the evolution of ω may be calculated by diagonalising $\mathbf{I}$ at each time step.

In the derivations below, we adopt the approximation inherent to equation (5.2), and the problem reduces to finding all contributors to the moment of inertia tensor, $\mathbf{I}$. In general, this tensor can be decomposed into three components: (i) the initial (background) equilibrium form of the planet, (ii) any deformations of the planet arising from perturbations in the centrifugal potential, and (iii) mass loads and their associated boundary (surface or internal) deformations.

5.2.2 Viscoelastic Love Numbers

For a spherically symmetric, linear viscoelastic body, the deformation components within the contributions (ii) and (iii) of the last paragraph are commonly described in terms of load and tidal (or tidal effective) viscoelastic k Love numbers at spherical harmonic degree 2 [Peltier, 1974]. In the time domain, these Love numbers may be written, respectively, as

$$k^L(t,\mathrm{LT}) = k^{L,E}\delta(t) + \sum_{k=1}^{K} r'_k e^{-s_k t}\,, \tag{5.3}$$

$$k^T(t,\mathrm{LT}) = k^{T,E}\delta(t) + \sum_{k=1}^{K} r''_k e^{-s_k t}\,, \tag{5.4}$$

where the superscript E denotes the elastic component of the Love numbers, $\delta(t)$ is the Dirac delta function, r'_k and r''_k are the amplitudes of a set of K normal modes of viscoelastic decay associated

with the load and tidal response, respectively. The s_k are the associated characteristic decay times for these modes, which are the same for both the loading and tidal responses. The amplitudes and decay times are a function of the internal structure of the planet. For reasons that will become clear below, we have made the dependence of the Love numbers on the elastic thickness of the lithosphere, LT, explicit. In the Laplace-transform domain (i.e., s-domain), the Love numbers have the form

$$k^L(s, \mathrm{LT}) = k^{L,E} + \sum_{k=1}^{K} \frac{r'_k}{s + s_k} , \tag{5.5}$$

$$k^T(s, \mathrm{LT}) = k^{T,E} + \sum_{k=1}^{K} \frac{r''_k}{s + s_k} . \tag{5.6}$$

Taking the limit as $s \to 0$, we have the so-called fluid Love numbers,

$$k_f^L(\mathrm{LT}) = k^{L,E} + \sum_{k=1}^{K} \frac{r'_k}{s_k} , \tag{5.7}$$

$$k_f^T(\mathrm{LT}) = k^{T,E} + \sum_{k=1}^{K} \frac{r''_k}{s_k} . \tag{5.8}$$

The fluid Love numbers characterise the response of the planet after all viscous stresses have relaxed; they are dependent on the thickness of the purely elastic lithosphere, but not on viscosity. The hydrostatic response of the planet can be expressed using fluid Love numbers with $\mathrm{LT} = 0$. Following Matsuyama et al. [2006], we will denote these special ($\mathrm{LT} = 0$) cases as $k_f^{T,*}$ and $k_f^{L,*}$, respectively.

In the next subsection, we consider the case where TPW driven by (external or internal) loading is only stabilised by the delayed, viscoelastic adjustment of the rotational bulge, i.e., the cases shown by Figure 5.1A and B. Following this, we extend the theoretical formulation to incorporate stabilisation associated with the remnant bulge, as in Figure 5.1C.

5.2.3 Transient Stabilisation by the Rotational Bulge

In the initial, unperturbed state, we adopt a co-ordinate system aligned with the principal axis of inertia, such that the angular velocity vector is given by $\Omega = [0, 0, \Omega]$. Making use of viscoelastic Love number theory, a general expression for the time-dependent inertia tensor in the scenarios of Figures 5.1A and 5.1B is given by

$$\begin{aligned} \mathrm{I}_{ij}(t) = \mathrm{I}_0 \delta_{ij} + \frac{a^5}{3G} k_f^T(\mathrm{LT})\, \Omega^2 \left(\delta_{i3} - \frac{1}{3}\right) \delta_{ij} \\ + \frac{a^5}{3G} k^T(t, \mathrm{LT}) * \left\{ \left[\omega_i(t)\omega_j(t) - \frac{1}{3}\omega^2(t)\delta_{ij}\right] - \Omega^2 \left(\delta_{i3} - \frac{1}{3}\right) \delta_{ij} \right\} + \mathrm{I}_{ij}^L(t)\,, \end{aligned} \quad (5.9)$$

where δ_{ij} is the Kronecker delta, a is the radius of the Earth, G is the gravitational constant, ω is the magnitude of the ω vector, and the $*$ denotes a time convolution. The first two terms on the right-hand side of the equation represent the inertia tensor in the initial, pre-loaded state of the planet (Figure 5.1A1, where $\mathrm{LT} = 0$, and Figure 5.1B1, where $\mathrm{LT} \neq 0$). The first of these terms is the moment of inertia of the spherical, non-rotating planet; the second is the (infinite-time) departure from sphericity driven by the centrifugal potential associated with the initial angular velocity vector, Ω. The third term involves a time convolution between the tidal Love number and the perturbation in the centrifugal potential from this initial state. This time convolution introduces a delayed, viscous response of the rotational bulge to the evolving rotation vector, and this delay acts to stabilise the pole [Ricard et al., 1993]. The last term is the load inertia tensor (contribution (iii) in the last paragraph of § 5.2.1).

The Equilibrium Theory of Gold [1955]

The physics described by Gold [1955] was concerned with the response of the rotating system over timescales much longer than those that govern the viscous adjustment of the rotational bulge. In this limit, the modes of viscoelastic decay associated with the k^T Love number will be fully

relaxed, and equation (5.9) simplifies to

$$\mathrm{I}_{ij}(t) = \mathrm{I}_0\delta_{ij} + \frac{a^5}{3G}\,k_f^T(\mathrm{LT})\left[\omega_i(t)\omega_j(t) - \frac{1}{3}\omega^2(t)\delta_{ij}\right] + \mathrm{I}_{ij}^L(t)\ . \tag{5.10}$$

The first two terms on the right-hand side represent the response of the planet in the fluid limit to the (very slowly) evolving centrifugal potential. This so-called equilibrium form indicates that, under the assumptions used to derive equation (5.9), the rotational bulge ultimately adjusts perfectly to any changes in the angular velocity vector, ω. As discussed above, TPW is computed by applying the expression equation (5.10) in the eigenvalue equation (5.2). In this case, the equilibrium form does not contribute, and the time-dependent orientation of the rotation axis (i.e., TPW) is given by the principal axis of the load inertia tensor $\mathrm{I}_{ij}^L(t)$ with maximum moment; hence, the load will always reach the equator (Figures 5.1A5 and B5). The scenarios shown in rows A and B of Figure 5.1 are distinguished by the choice of LT. In the former case, where $\mathrm{LT} = 0$, the planet is in hydrostatic equilibrium in both the initial and final states (Figures 5.1A1 and A5).

The Ricard et al. [1993] Formulation

Whereas Gold [1955] was concerned with the final, equilibrium state of the load, Ricard et al. [1993] was concerned with the timescale of polar motion towards this state; that is, the time-dependent evolution shown schematically in Figures 5.1A2–A5 or 5.1B2–B5. This time dependence is governed by equation (5.9). If we once again collect and cancel the terms in Ω, this equation simplifies to

$$\mathrm{I}_{ij}(t) = \mathrm{I}_0\delta_{ij} + \frac{a^5}{3G}\,k^T(t,\mathrm{LT}) * \left[\omega_i(t)\omega_j(t) - \frac{1}{3}\omega^2(t)\delta_{ij}\right] + \mathrm{I}_{ij}^L(t)\ . \tag{5.11}$$

Ricard et al. [1993] used the convolution theorem to express the time convolution in equation (5.11) as a simple multiplication in the Laplace transform (s) domain. In this context,

they derived the following approximation for the s-domain k^T Love number in the small s limit:

$$k^T(s, \mathrm{LT}) \approx k_f^T(\mathrm{LT})\ [1 - T_1 s]\ , \tag{5.12}$$

where

$$T_1 \equiv \frac{1}{k_f^T(\mathrm{LT})} \sum_{k=1}^{K} \frac{r_k''}{s_k^2}\ .$$

The small-s approximation is consistent with the assumption of a long-timescale forcing that permits the application of the eigenvalue approach (equation 5.2) for predicting TPW. Using the expression (5.12) in the s-domain form of equation (5.11), and inverting the result back into the time domain, yields [Ricard et al., 1993]

$$\begin{aligned} \mathrm{I}_{ij}(t) = \mathrm{I}_0 \delta_{ij} + \frac{a^5}{3G} k_f^T(\mathrm{LT}) \left[\omega_i(t)\omega_j(t) - \frac{1}{3}\omega^2(t)\delta_{ij} \right] \\ - \frac{a^5}{3G} k_f^T(\mathrm{LT})\, T_1 \left[\dot{\omega}_i(t)\omega_j(t) + \omega_i(t)\dot{\omega}_j(t) - \frac{2}{3}\omega_\ell(t)\dot{\omega}_\ell(t)\delta_{ij} \right] + \mathrm{I}_{ij}^L(t)\ . \end{aligned} \tag{5.13}$$

Following equation (5.2), Ricard et al. [1993] computed TPW by tracking the time-dependent principal axis of the inertia tensor $\mathrm{I}_{ij}(t)$ with maximum moment. As in the last section, the first two terms on the right-hand side of equation (5.13), which represent the equilibrium form, do not impact the diagonalization, and thus the reorientation is governed by a competition between the driving force for TPW ($\mathrm{I}_{ij}^L(t)$) and the stabilisation associated with the delayed viscous adjustment of the rotational bulge (the third term on the right-hand side of equation 5.13).

5.2.4 Incorporating Stabilisation by the Remnant Bulge

As described in the context of Figure 5.1C, remnant bulge stabilisation arises when the response of the rotating planet to a perturbed centrifugal potential is governed by a planetary model with an elastic lithospheric thickness that is different from the thickness associated with the rotational form

of the background (i.e., initial, pre-loading) state. In the case of Figure 5.1C, the background state is hydrostatic, but the planetary response to the evolving centrifugal potential is determined by a model with LT $\neq 0$.

The inertia tensor perturbation associated with this scenario can be derived by replacing $k_f^T(\mathrm{LT})$ in the second term of the right-hand side of equation (5.9) with the fluid Love number governing the hydrostatic form, $k_f^{T,*}$. This yields

$$\mathrm{I}_{ij}(t) = \mathrm{I}_0 \delta_{ij} + \frac{a^5}{3G} k_f^{T,*} \Omega^2 \left(\delta_{i3} - \frac{1}{3} \right) \delta_{ij} + \frac{a^5}{3G} k^T(t, \mathrm{LT}) * \left\{ \left[\omega_i(t) \omega_j(t) - \frac{1}{3} \omega^2(t) \delta_{ij} \right] - \Omega^2 \left(\delta_{i3} - \frac{1}{3} \right) \delta_{ij} \right\} + \mathrm{I}_{ij}^L(t) \, . \quad (5.14)$$

The first two terms on the right-hand side represent the initial, hydrostatic state (Figure 5.1C1). As in equation (5.9) (or equation 5.13), the third term introduces a delayed, viscous response of the rotational bulge to the evolving rotation vector. However, in contrast to this earlier equation, the rotational bulge cannot adjust perfectly to a perturbation in pole position (i.e., in the long-term fluid limit, the two terms involving Ω on the right-hand side of equation (5.14) do not cancel) and this non-cancelation gives rise to the remnant bulge stabilisation. We can rearrange equation (5.14) by collecting the two terms in Ω. This exercise yields

$$\mathrm{I}_{ij}(t) = \mathrm{I}_0 \delta_{ij} + \frac{a^5}{3G} \left[k_f^{T,*} - k_f^T(\mathrm{LT}) \right] \Omega^2 \left(\delta_{i3} - \frac{1}{3} \right) \delta_{ij} + \frac{a^5}{3G} k^T(t, \mathrm{LT}) * \left[\omega_i(t) \omega_j(t) - \frac{1}{3} \omega^2(t) \delta_{ij} \right] + \mathrm{I}_{ij}^L(t) \, . \quad (5.15)$$

The remnant bulge stabilisation is given by the second term of the right-hand side, which is a function of the difference between the fluid k Love number for the two planetary models with and without an elastic lithosphere. Note that if we set LT $= 0$, this stabilisation disappears.

If we once again apply both the small-s approximation to the s-domain form of the k^T Love

number (equation 5.12) and the convolution theorem to equation (5.15), we arrive, after some minor rearrangement, at the result

$$\begin{aligned} \mathrm{I}_{ij}(t) = \mathrm{I}_0 \delta_{ij} + \frac{a^5}{3G} k_f^T(\mathrm{LT}) \left[\omega_i(t)\omega_j(t) - \frac{1}{3}\omega^2(t)\delta_{ij} \right] \\ + \frac{a^5}{3G} \left[k_f^{T,*} - k_f^T(\mathrm{LT}) \right] \Omega^2 \left(\delta_{i3} - \frac{1}{3} \right) \delta_{ij} \\ - \frac{a^5}{3G} k_f^T(\mathrm{LT})\, T_1 \left[\dot{\omega}_i(t)\omega_j(t) + \omega_i(t)\dot{\omega}_j(t) - \frac{2}{3}\omega_\ell(t)\dot{\omega}_\ell(t)\delta_{ij} \right] + \mathrm{I}_{ij}^L(t) \,. \quad (5.16) \end{aligned}$$

Using equation (5.16) in the eigenvalue equation (5.2) yields a time-dependent, non-linear theory of TPW that incorporates stabilisation due to both the delayed, viscous adjustment of the rotational bulge and the remnant bulge. As before, the first two terms on the right-hand side of the equation (the equilibrium form) do not impact the diagonalisation, and thus the reorientation of the rotation axis is governed by a competition between the driving force for TPW ($\mathrm{I}_{ij}^L(t)$) and the stabilisations associated with both the delayed viscous adjustment of the rotational bulge and the remnant bulge (the fourth and third terms on the right-hand side of equation (5.16), respectively).

In analogy with § 5.2.3 (equation 5.10), we can use the above equations to derive an expression for the inertia tensor perturbation in the case when the driving load is applied over timescales much longer than those that characterise the viscous adjustment of the rotational bulge (i.e., the equilibrium case). Eq. (5.15) then simplifies to

$$\begin{aligned} \mathrm{I}_{ij}(t) = \mathrm{I}_0 \delta_{ij} + \frac{a^5}{3G} k_f^T(\mathrm{LT}) \left[\omega_i(t)\omega_j(t) - \frac{1}{3}\omega^2(t)\delta_{ij} \right] \\ + \frac{a^5}{3G} \left[k_f^{T,*} - k_f^T(\mathrm{LT}) \right] \Omega^2 \left(\delta_{i3} - \frac{1}{3} \right) \delta_{ij} + \mathrm{I}_{ij}^L(t) \,. \quad (5.17) \end{aligned}$$

We could have also derived this expression by setting the time derivatives of the angular velocity components in equation (5.16) to zero. The above expression extends equation (5.10) to incorporate remnant bulge stabilisation. In contrast to the earlier result, the final location of a load that is

applied and retained for all time is not the equator. Rather, the location is established through a balance between the load forcing and the remnant bulge stabilisation. In practical terms, the equilibrium TPW is computed, following equation (5.2), by diagonalising the sum of the third and fourth terms on the right-hand side of equation (5.17).

5.2.5 External Loads: The Form of $\mathrm{I}^L_{ij}(t)$

The derivations above are general in the sense that they apply to the case of either external or internal loading processes. In the case of the latter, the time-dependent inertia tensor may be input from a simulation of mantle convection (on Earth or other terrestrial planets) and, in this regard, one can make use of the well-established mapping between the components of the inertia tensor and the spherical harmonic components of the gravitational potential at degree 2 [e.g. Matsuyama et al., 2006]. These harmonic components must, of course, include contributions both from mantle buoyancy variations and boundary deformations driven by this buoyancy field.

In the case of external mass loads, one can decompose the load inertia tensor $\mathrm{I}^L_{ij}(t)$ into terms associated with the mass anomalies and the planetary deformation driven by the mass anomalies. The latter contribution can, in turn, be expressed using viscoelastic load Love number theory, just as we used viscoelastic tidal Love numbers to express the deformation induced by a perturbed centrifugal potential. In particular, if we denote the inertia tensor perturbation associated with surface mass redistribution on a rigid Earth as $\mathrm{I}^R_{ij}(t)$, then the inertia perturbation due to the combined effects of this redistribution and the associated planetary deformation, i.e., $\mathrm{I}^L_{ij}(t)$, is given by

$$\mathrm{I}^L_{ij}(t) = [\delta(t) + k^L(t, \mathrm{LT})] * \mathrm{I}^R_{ij}(t) = \mathrm{I}^R_{ij}(t) + k^L(t, \mathrm{LT}) * \mathrm{I}^R_{ij}(t) \, . \tag{5.18}$$

This relation can be applied in place of $\mathrm{I}^L_{ij}(t)$ in any of the expressions for the total inertia tensor perturbation derived above when one is considering TPW driven by surface mass loading. In par-

ticular, equation (5.16) becomes

$$\begin{aligned}\mathrm{I}_{ij}(t) = \mathrm{I}_0\delta_{ij} + \frac{a^5}{3G}k_f^T(\mathrm{LT})\left[\omega_i(t)\omega_j(t) - \frac{1}{3}\omega^2(t)\delta_{ij}\right] \\ + \frac{a^5}{3G}\left[k_f^{T,*} - k_f^T(\mathrm{LT})\right]\Omega^2\left(\delta_{i3} - \frac{1}{3}\right)\delta_{ij} + \left[\mathrm{I}_{ij}^R(t) + k^L(t,\mathrm{LT}) * \mathrm{I}_{ij}^R(t)\right] \\ - \frac{a^5}{3G}k_f^T(\mathrm{LT})\,T_1\left[\dot{\omega}_i(t)\omega_j(t) + \omega_i(t)\dot{\omega}_j(t) - \frac{2}{3}\omega_\ell(t)\dot{\omega}_\ell(t)\delta_{ij}\right]. \quad (5.19)\end{aligned}$$

The Case of An Axisymmetric Surface Mass Load

It will be useful, in comparing our results to those of Willemann [1984] and Matsuyama et al. [2006], to consider a further special case of equation (5.19) valid for an axisymmetric surface mass load applied at time $t = 0$ and retained for all time. We can denote the space-time dependence of this surface mass load by $R(\theta, \psi)H(t)$, where θ and ψ are the colatitude and east-longitude, respectively, and $H(t)$ is the Heaviside step function. (We note that a disk load with arbitrary time dependence can be modelled as a series of step loadings with suitable time lags, and therefore, in practical terms, the Heaviside time dependence involves no loss of generality.) The spherical harmonic decomposition of R can then be written as

$$R(\theta,\ \psi) = \sum_{\ell=0}^{\infty}\sum_{m=-\ell}^{\ell} R_{\ell m}Y_{\ell m}(\theta, \psi), \quad (5.20)$$

where $Y_{\ell m}$ are complex surface spherical harmonics of degree ℓ and order m. We will assume that these basis functions are normalised such that

$$\int_S Y^{\dagger}_{\ell' m'}(\theta, \psi)Y_{\ell m}(\theta, \psi)d\Omega = 4\pi\delta_{\ell\ell'}\delta_{mm'}, \quad (5.21)$$

where † denotes complex conjugation.

The load inertia tensor perturbation, $\mathbf{I}^R(t)$, can be expressed in terms of the spherical harmonic

components of the surface mass load at degree 2 [e.g., Matsuyama et al., 2006]:

$$
\begin{aligned}
I^R_{11}(t) &= 4\pi a^4 \left[\frac{1}{3\sqrt{5}} R_{20} - \sqrt{\frac{2}{15}} \mathrm{Re}(R_{22}) \right] H(t) \\
I^R_{22}(t) &= 4\pi a^4 \left[\frac{1}{3\sqrt{5}} R_{20} + \sqrt{\frac{2}{15}} \mathrm{Re}(R_{22}) \right] H(t) \\
I^R_{33}(t) &= -\frac{8\pi a^4}{3\sqrt{5}} R_{20} H(t) \\
I^R_{12}(t) &= \frac{8\pi a^4}{\sqrt{30}} \mathrm{Im}(R_{22}) H(t) \\
I^R_{13}(t) &= \frac{8\pi a^4}{\sqrt{30}} \mathrm{Re}(R_{21}) H(t) \\
I^R_{23}(t) &= -\frac{8\pi a^4}{\sqrt{30}} \mathrm{Im}(R_{21}) H(t)
\end{aligned}
\quad . \tag{5.22}
$$

Next, consider an axisymmetric load centred at a colatitude θ_L and east longitude ψ_L. Let us say that this load, if centred at the north pole, had a degree-2 zonal harmonic given by R'_{20}, then one can show that the spherical harmonic coefficients for the load centred at (θ_L, ψ_L) are given by [Matsuyama et al., 2006]

$$
R_{2m} = R'_{20} \frac{Y^\dagger_{2m}(\theta_L, \psi_L)}{\sqrt{5}}. \tag{5.23}
$$

Willemann [1984] normalised the surface mass load by considering the ratio between the degree-2 perturbations in the geopotential associated with the direct effect of the load and the hydrostatic rotational bulge. In particular, he defined a parameter Q' such that

$$
Q' = -\frac{\frac{4\pi a G}{5} R'_{20}}{-\frac{1}{3\sqrt{5}} a^2 \Omega^2 k_f^{T,*}}. \tag{5.24}
$$

Using equations (5.23) and (5.24) in equation (5.22), and, for simplicity, choosing $\psi_L = 0$ yields

$$
\begin{aligned}
I^R_{11}(t) &= \frac{\Omega^2 a^5}{9G} k_f^{T,*} Q' \left[P_{20}(\cos\,\theta_L) - \frac{1}{2} P_{22}(\cos\,\theta_L) \right] H(t) \\
I^R_{22}(t) &= \frac{\Omega^2 a^5}{9G} k_f^{T,*} Q' \left[P_{20}(\cos\,\theta_L) + \frac{1}{2} P_{22}(\cos\,\theta_L) \right] H(t) \\
I^R_{33}(t) &= -\frac{2\Omega^2 a^5}{9G} k_f^{T,*} Q' P_{20}(\cos\,\theta_L) H(t) \\
I^R_{13}(t) &= \frac{\Omega^2 a^5}{9G} k_f^{T,*} Q' P_{21}(\cos\,\theta_L) H(t) \\
I^R_{12}(t) &= I^R_{23}(t) = 0
\end{aligned}
\quad , \tag{5.25}
$$

where the P_{2m} are un-normalised associated Legendre polynomials. Our predictions of time-dependent TPW driven by an axisymmetric surface mass load are generated by applying the above expressions into (5.19) and diagonalising the result.

The Equilibrium Theory of Willemann [1984] and Matsuyama et al. [2006]

Willemann [1984] and Matsuyama et al. [2006] were concerned with the final displacement of the rotation axis in the case of the axisymmetric loading treated in the last subsection. If we consider the inertia tensor an infinite time after the application of the surface mass load, then equation (5.19) becomes

$$
\begin{aligned}
\mathrm{I}_{ij}(t_\infty) = \mathrm{I}_0 \delta_{ij} &+ \frac{a^5}{3G} k_f^T(\mathrm{LT}) \left[\omega_i(t_\infty)\omega_j(t_\infty) - \frac{1}{3}\omega^2(t_\infty)\delta_{ij} \right] \\
&+ \frac{a^5}{3G} \left[k_f^{T,*} - k_f^T(\mathrm{LT}) \right] \Omega^2 \left(\delta_{i3} - \frac{1}{3} \right) \delta_{ij} + \left[1 + k_f^L(\mathrm{LT}) \right] \mathrm{I}^R_{ij}(t_\infty) \, .
\end{aligned} \tag{5.26}
$$

The equilibrium TPW is governed by the diagonalisation of the third plus fourth term on the right-hand side of this equation. If we denote the sum of these two terms by the superscript *eq*, then we

have

$$\mathrm{I}_{ij}^{eq}(t_\infty) = \frac{a^5}{3G}\left[k_f^{T,*} - k_f^T(\mathrm{LT})\right]\Omega^2\left(\delta_{i3} - \frac{1}{3}\right)\delta_{ij} + \left[1 + k_f^L(\mathrm{LT})\right]\mathrm{I}_{ij}^R(t_\infty)\,. \tag{5.27}$$

Using equations (5.23)–(5.25) in equation (5.27), and diagonalising the result, yields a TPW angle δ given by

$$\delta = \frac{1}{2}\arctan\left[\frac{Q_{eff}\sin(2\theta_L)}{1 - Q_{eff}\cos(2\theta_L)}\right], \tag{5.28}$$

where $Q_{eff} = Q'\alpha$, and

$$\alpha = \frac{1 + k_f^L(\mathrm{LT})}{1 - k_f^T(\mathrm{LT})/k_f^{T,*}}. \tag{5.29}$$

This result for δ is identical to the expression derived by Matsuyama et al. [2006].

The TPW angle is a function of the initial load colatitude, θ_L, and on the parameter Q_{eff}. Embedded in the latter is a sensitivity to the uncompensated size of the load (governed by the parameter Q') and the parameter α, which is a function of the planetary density structure and the elastic thickness of the lithosphere. In Figure 5.2 we plot the TPW angle versus θ_L for a suite of solutions distinguished on the basis of the choice for Q_{eff}. A detailed discussion of the figure can be found in Matsuyama et al. [2006], and we include it here because it will serve as a useful reference for, and check of, the time-dependent TPW results discussed in the next section. We note that as $Q_{eff} \rightarrow \infty$ in Figure 5.2 (or equation 5.28), the reorientation of the pole is $90 - \theta_L$; that is, the final position of the pole is the equator. This is as one would expect. For a very large load, the load driving TPW will dominate the remnant bulge stabilisation and the solution converges to the scenario in Figure 5.1A5 or B5 described by Gold [1955]. As an example of a smaller surface mass load, consider the case of $Q_{eff} = 0.5$. A load of this size placed at an initial colatitude of 20°, will ultimately drive TPW of $\sim 13°$, or just $\sim 20\%$ of the 70° reorientation expected on the basis of an equilibrium theory of Gold [1955].

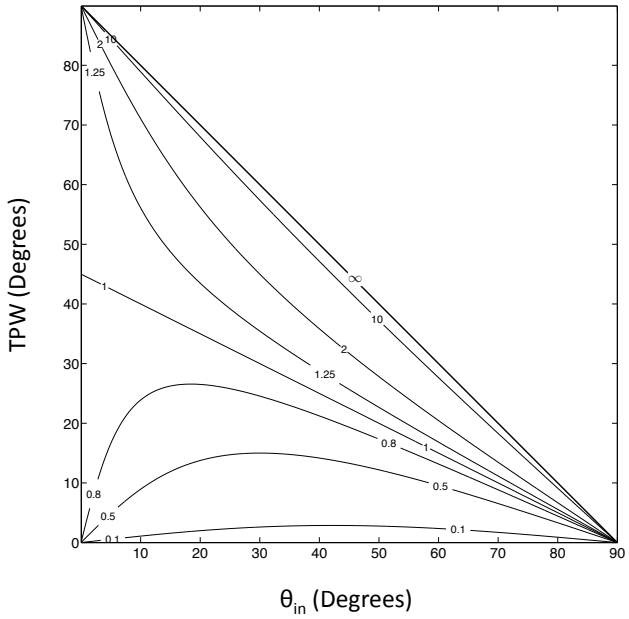

Figure 5.2: Predictions of equilibrium TPW angle as a function of the initial colatitude (θ_L) of the loading (see equation 5.28). The lines join solutions based on the same value of Q_{eff}, as indicated.

5.3 Results

In this section we present a suite of illustrative predictions of time-dependent TPW on spherical, self-gravitating, Maxwell viscoelastic Earth and Mars models that incorporate stabilisation from both the delayed adjustment of the rotational bulge and the remnant bulge. To begin, we consider TPW on Earth driven by simplified surface mass loads.

5.3.1 Time-dependent TPW on Earth: some illustrative examples

The elastic and density structure of the Earth model is taken from the seismically inferred Preliminary Reference Earth Model [Dziewonski & Anderson, 1981]. The viscosity of the Earth model is discretised into three layers: a uniform elastic (i.e., infinite viscosity) lithosphere of thickness LT; a constant upper mantle viscosity of 5×10^{20} Pa s; and a constant lower mantle viscosity de-

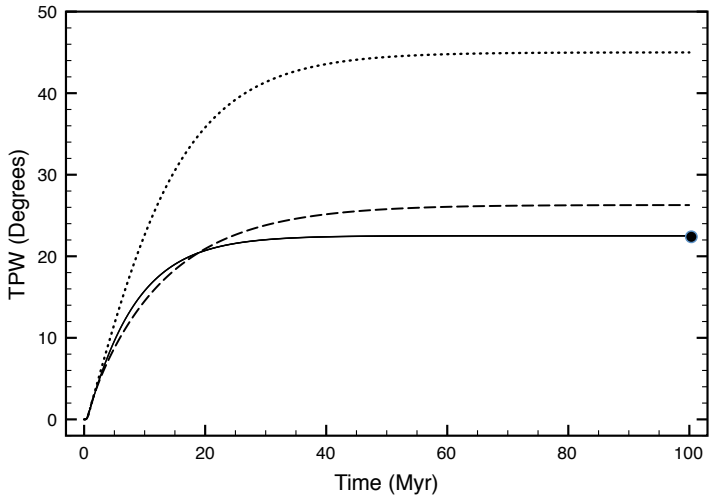

Figure 5.3: Predictions of surface-load induced TPW as a function of time computed using a Maxwell viscoelastic Earth characterised by an elastic lithospheric thickness LT = 15 km, and upper and lower mantle viscosities of 5 $\times$ 10^{20} Pa s and 10^{22} Pa s, respectively. The surface load is an axisymmetric disk centred at an initial colatitude θ_L = 45°. The disk size is increased such that the parameter Q_{eff} is varied from 0.0 to 1.0 in the first 1 Myr of the simulation (see text) and then retained for all time. This is the test model case discussed in the text. The solid and dotted lines are solutions in which remnant bulge stabilisation is either included (equation 5.19 with $\mathbf{I}^R(t)$ given by equation 5.25) or not included (the same equations, with the exception that the third term on the right-hand side of equation 5.19 is deleted), respectively, in the TPW calculation. As a check on the result with the remnant bulge stabilisation (solid line), we have repeated that calculation using the linearised rotational stability theory derived by Chan et al. [2011a] and discussed in § 5.2.1 (dashed line; see text). All calculations incorporate stabilisation by the delayed, viscous adjustment of the rotational bulge. The solid circle on the right-hand side of the figure is the TPW predicted for the test model case using the equilibrium (i.e., infinite time) theory of Matsuyama et al. [2006] (see equation 5.28).

noted by ν_{lm}. Both LT and ν_{lm} serve as free parameters of the modelling, but our standard case will be characterised by LT $=$ 15 km and ν_{lm} $=$ 10^{22} Pa s. The external load will be modelled as an axisymmetric disk load placed on the Greenwich meridian, and at an initial co-latitude of θ_L. The standard case will adopt θ_L $=$ 45° and a Q_{eff} value of unity. The size of the load is assumed to increase from zero to the adopted Q_{eff} value in the first 1 Myr of each simulation with a time dependence given by a hyperbolic tangent function. We chose this timescale because it is consistent with the underlying assumption of the theory that the loading timescale is longer than the longest normal mode decay time, yet it is sufficiently short that the computed TPW departs from the path predicted using an equilibrium theory. Our predictions are based on equation (5.19),

with the inertia tensor perturbation associated with the direct effect of the surface mass load given by equation (5.25). The Earth has a broken lithosphere, and, as discussed in the introduction, we interpret the parameter LT as an effective elastic lithospheric thickness; our choice of LT $= 15$ km or the standard case is likely above the upper bound for this thickness [Creveling et al., 2012], and thus in an analysis described below we will consider the sensitivity of the predictions to a variation of LT in the range 5–25 km. As a final point, a numerical instability occurs for time steps that are too short (see § 5.5). In this regard, our time step for each model run is chosen to be uniform and as small as possible without encountering this instability.

In Figure 5.3, we plot the prediction of time-dependent TPW based on the standard case. The large dot on the extreme right of the figure is the equilibrium TPW computed using the analytic expression (5.28) [Matsuyama et al., 2006]. The agreement between this analytic expression and the long-time asymptote of the time-dependent TPW prediction provides an important check on the latter. The time-dependent prediction reaches 50% and 90% of the equilibrium value (22.5°) in 6.1 Myr and 18.3 Myr, respectively. (We henceforth denote the time elapsed for the pole to reach half its maximum value by the symbol $t_{1/2}$.)

As a second check on the result in Figure 5.3, we have repeated the standard calculation using the linearised rotational stability theory derived by Chan et al. [2011a] and discussed in § 5.2.1 (dashed line, Figure 5.3). This theory does not require that the forcing have a timescale comparable to or longer than the longest mode of viscoelastic decay, but it assumes that perturbations to the pole position are 'small'. Chan et al. [2011a] explored the range of validity for their linearised theory, and found that, for forcing placed near mid-latitudes, errors are only O(10%) for TPW of 20–30°. This estimate is consistent with the offset between the solid and dashed lines on Figure 5.3 at the limit of $t \to \infty$. We assume that in the earliest stages of TPW in Figure 5.3, the Chan et al. [2011a] theory is more accurate. During this phase, we note that the discrepancy between results generated with the linear and non-linear theories is small.

The dotted line in Figure 5.3 is analogous to the solid, with the exception that stabilisation due

to the remnant bulge is ignored by deleting the third term on the right-hand side of equation (5.19). This deletion yields a governing equation consistent with the rotational stability theory derived by Ricard et al. [1993]. The equilibrium TPW predicted in this case (45°) is such that the final position of the disk load is at the equator, as expected from the physics associated with Figure 5.1B, Gold [1955] and Ricard et al. [1993]. As we noted in our discussion of stabilisation due to the remnant bulge, the existence of even a relatively thin elastic lithosphere is sufficient to significantly reduce the predicted TPW from the value expected on the basis of the canonical theory of Gold [1955] [Matsuyama et al., 2006; Daradich et al., 2008]. However, we note from Figure 5.3 that the inclusion of remnant bulge stabilisation also acts to alter the characteristic timescale of the predicted TPW. As an example, $t_{1/2} = 9.9$ Myr for the dotted line in Figure 5.3, which is 65% longer than the analogous timescale for the case where the remnant bulge is included. This difference is primarily due to the reduced amplitude of TPW when remnant bulge stabilisation is included, whereas the damping caused by the viscous rotational bulge remains relatively unchanged between both cases.

We next turn to a sensitivity analysis in which we repeat the calculation in Figure 5.3 (solid line) for a suite of simulations in which Q_{eff}, ν_{lm} and θ_L are individually varied while the other parameters are held constant at values that define the standard case. Figures 5.4 and 5.5 show predictions of time-dependent TPW and TPW speed, respectively. In addition, for each of these time-dependent simulations, we compute and plot the value of $t_{1/2}$ and the peak TPW speed in Figures 5.6 and 5.7.

As Q_{eff} is increased, the equilibrium position of the pole increases asymptotically toward 45°. That is, as the load size increasingly dominates the remnant bulge stabilisation, the final load position will reach progressively closer to the equator (Figure 5.4A). (Note, once again, that the long time limit of each simulation in Figure 5.4A matches the equilibrium TPW predicted on the basis of equation 5.28.) Regardless of the value of Q_{eff}, the peak speed of TPW is obtained at the end of the loading phase, 1 Myr after the onset of loading. It is interesting to note that the peak TPW

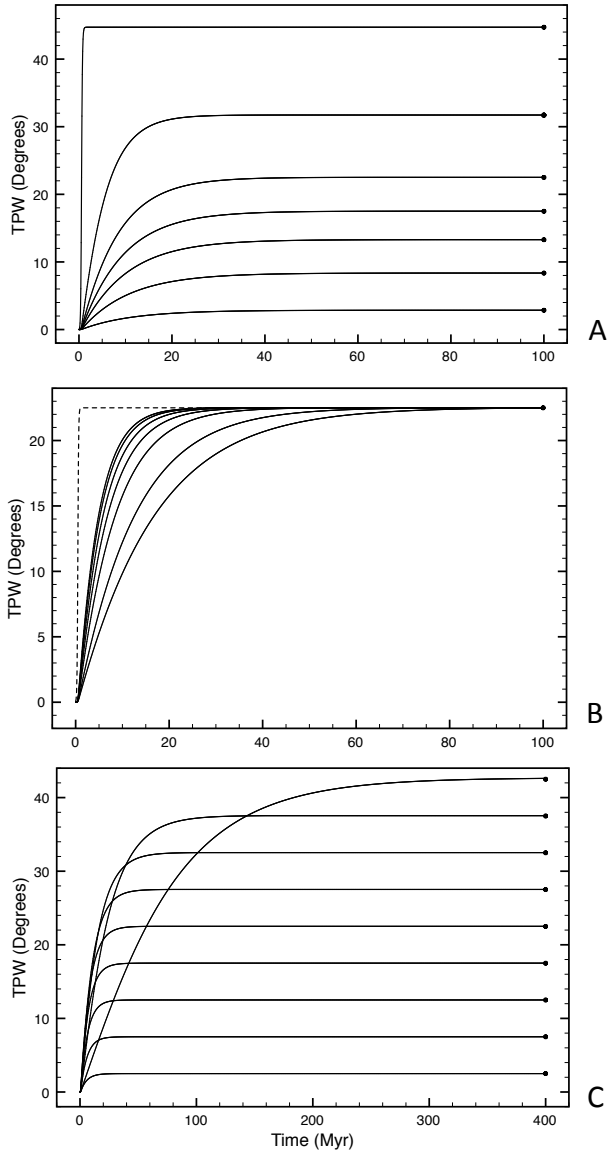

Figure 5.4: Predictions of surface-load induced TPW as a function of time computed for a suite of simulations in which the parameter Q_{eff}, the lower mantle viscosity ν_{lm}, or the initial load colatitude θ_L are varied from the test model case used in Figure 5.3 (solid line). (A) Q_{eff} values (from bottom to top) of 0.1, 0.3, 0.5, 0.7, 1.0, 2.0 and 100.0. (B) ν_{lm} values (solid lines from left to right) of 1, 2, 3, 5, 10, 20 and 30 $\times$ 10^{21} Pa s. The dashed line is a solution in which the rotational bulge stabilisation is excluded (i.e., the term involving T_1 in equation 5.19 is set to 0). (C) θ_L values (from top-right to bottom-right) of 5°, 15°, 25°, 35°, 45°, 55°, 65°, 75° and 85°. All calculations include stabilisation by both the delayed viscous adjustment of the rotational bulge and the remnant bulge (equation 5.19 with $\mathbf{I}^R(t)$ given by equation 5.25). The solid circles on the right-hand side of the results on each figure are the TPW predictions based on the equilibrium (i.e., infinite time) theory of Matsuyama et al. [2006] (see equation 5.28).

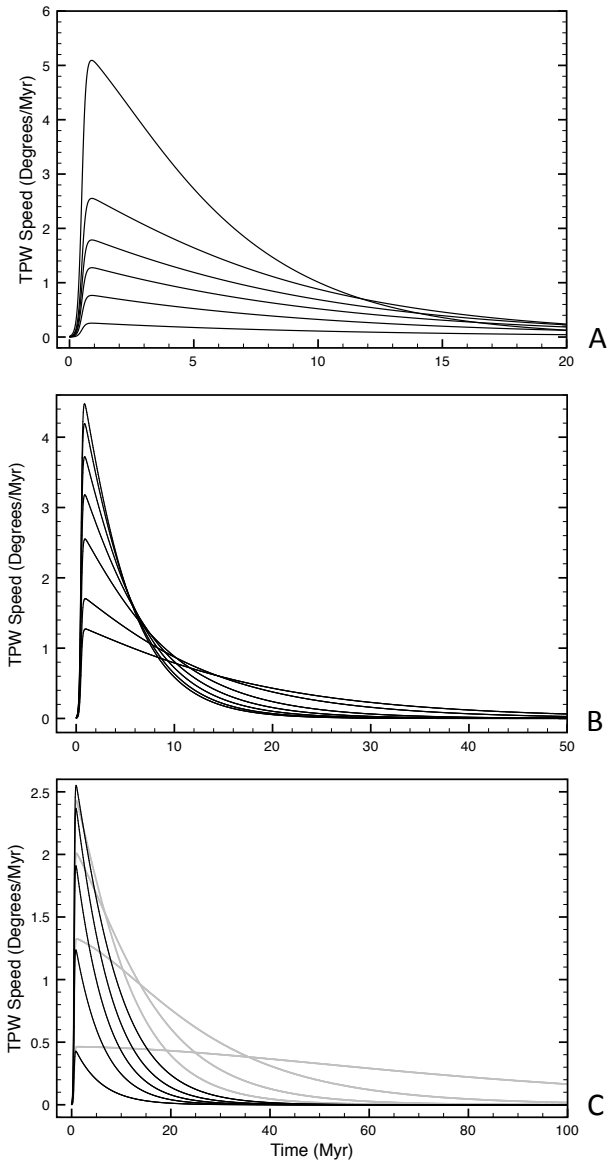

Figure 5.5: Predictions of surface-load induced TPW speed as a function of time computed for a suite of simulations in which the parameter Q_{eff}, the lower mantle viscosity ν_{lm}, or the initial load colatitude θ_L are varied from the test model case used in Figure 5.3 (solid line). (A) Q_{eff} values (from bottom to top) of 0.1, 0.3, 0.5, 0.7, 1.0, and 2.0. (B) ν_{lm} values (from top to bottom at location of peaks) of 1, 2, 3, 5, 10, 20 and 30 $\times$ 10^{21} Pa s. (C) θ_L values (from bottom to top at peak values of grey lines) of 5°, 15°, 25°, 35°, and (from top to bottom at peak values of black lines) 45°, 55°, 65°, 75° and 85°. All calculations include stabilisation by both the delayed viscous adjustment of the rotational bulge and the remnant bulge (equation 5.19 with $\mathbf{I}^R(t)$ given by equation 5.25).

speed is a linear function of the adopted value of Q_{eff} (Figure 5.7A). In contrast, the time to reach half the final TPW, $t_{1/2}$, varies in a more complex manner with the adopted Q_{eff} (Figure 5.6A). Specifically, for values of $Q_{eff} \leq 0.5$, $t_{1/2} \sim 7$–8 Myr and is relatively insensitive to variations in Q_{eff}. As Q_{eff} increases above ~ 0.5, $t_{1/2}$ decreases more rapidly.

Each of Figures 5.4B, 5.5B, 5.6B, and 5.7B shows results for a suite of simulations in which the lower mantle viscosity of the Earth model is varied from 10^{21} Pa s to 3×10^{22} Pa s. The equilibrium (i.e., long-time) position of the pole is entirely insensitive to ν_{lm}, while the time-dependent trajectory toward this equilibrium value is not (Figure 5.4B). The parameter $t_{1/2}$ is linearly proportional to the adopted value of ν_{lm} (Figure 5.6B). The proportionality is such that the factor of 30 increase in viscosity treated in the figure produces a factor of ~ 3.5 increase in the time necessary for the pole to be displaced by half its equilibrium displacement. Figure 5.6B shows the analogous prediction for $Q_{eff} = 0.1$. This additional calculation indicates that the linear proportionality between ν_{lm} and $t_{1/2}$ is a general result, and that the proportionality constant connecting these parameters is weakly sensitive to the adopted Q_{eff}. In contrast to these results, while the peak TPW speed decreases monotonically with increasing ν_{lm}, this decrease is not a linear function of the adopted lower mantle viscosity (Figure 5.7B).

The dashed line in Figure 5.4B represents a TPW simulation in which the stabilising effects of the delayed adjustment of the rotational bulge is excluded. At each stage in the loading, the dashed line represents the TPW computed using the equilibrium theory of Matsuyama et al. [2006] (equation 5.28). The lag between the dashed line and each of the solid lines represents the delay associated with the adjustment of the rotational bulge, which is, of course, a function of the adopted lower mantle viscosity. Inferences of lower mantle viscosity [Nakada & Lambeck, 1989; Mitrovica, 1996; Lambeck et al., 1998; Mitrovica & Forte, 2004] are greater than the lowest viscosity (10^{21} Pa s) in the figure, indicating that stabilisation associated with the rotational bulge is active for loading timescales of order 1 Myr.

The predicted time dependence of TPW is a complex function of the initial position of the disk

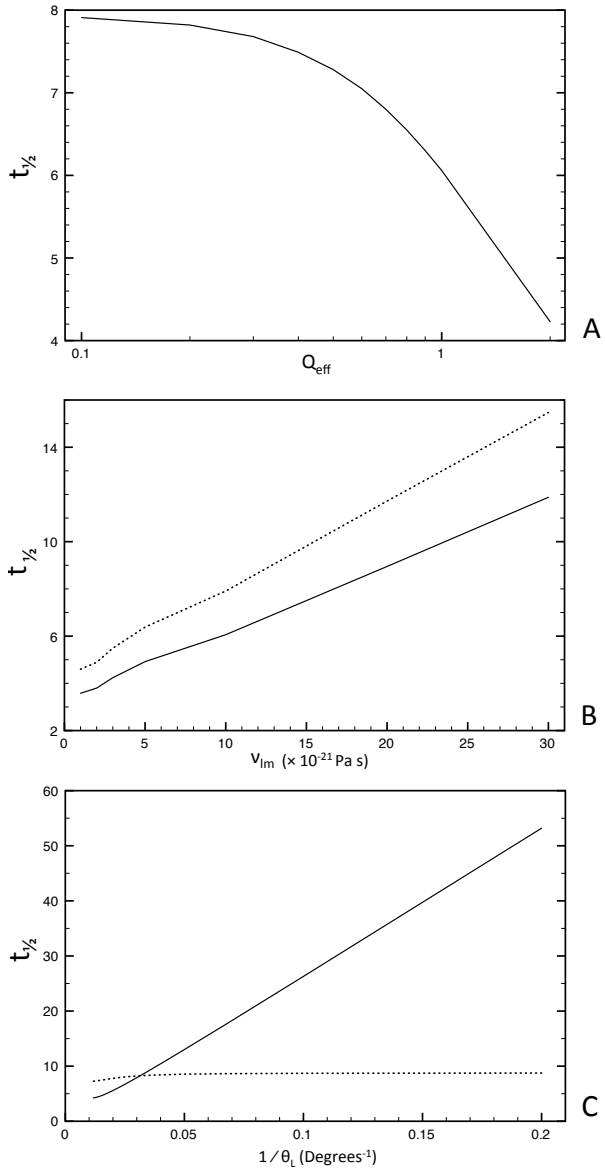

Figure 5.6: Solid lines on each frame show predictions of the time (in Myr) required for the pole to be displaced by half the maximum (i.e., infinite time) value ($t_{1/2}$) for a suite of simulations in which the parameter Q_{eff}, the lower mantle viscosity ν_{lm}, or the initial load colatitude θ_L are varied from the test model case used in Figure 5.3 (solid line). (A) Q_{eff} is varied from 0.1 to 2.0; (B) ν_{lm} is varied from 10^{21} Pa s to 30 $\times$ 10^{21} Pa s; and (C) θ_L is varied from 5° (or $1/\theta_L$ = 0.2) to 85°. In frames (B) and (C), the dotted line shows a result analogous to the solid line case (where Q_{eff} = 1.0) with the exception that the parameter Q_{eff} has a value of 0.1. All calculations include stabilisation by both the delayed viscous adjustment of the rotational bulge and the remnant bulge (equation 5.19 with $\mathbf{I}^R(t)$ given by equation 5.25).

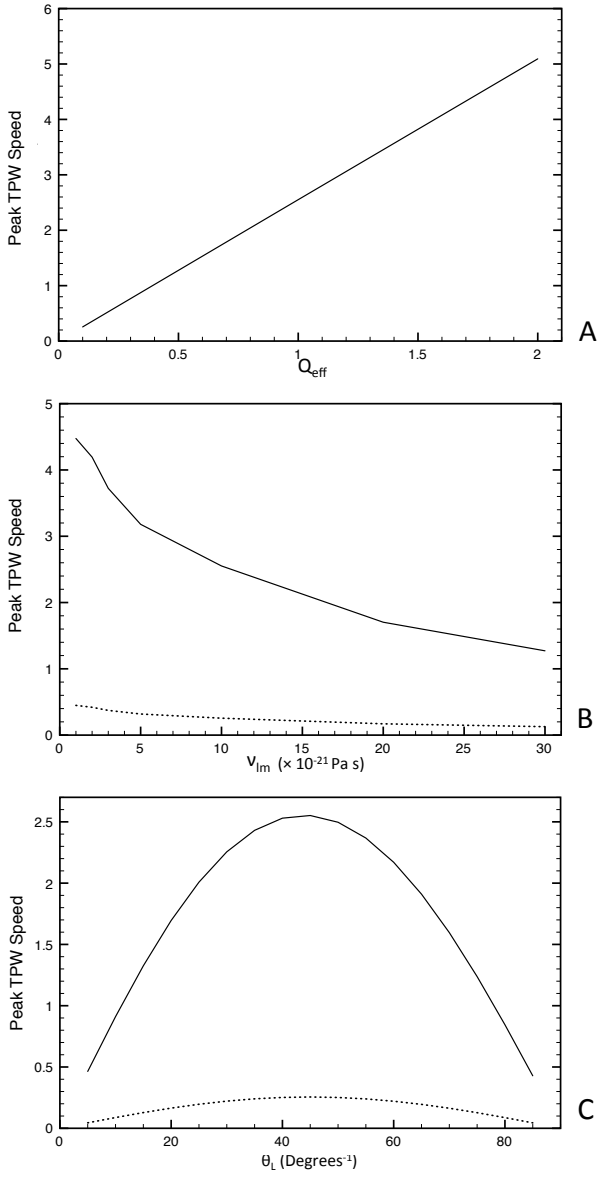

Figure 5.7: As in Figure 5.6, except for predictions of the peak TPW speed (Degrees/Myr).

load (Figure 5.4C). This complexity is particularly evident in the time dependence of the TPW speed, which is characterised by a non-monotonic peak amplitude (Figure 5.5C). In particular, the predicted peak TPW speed is highest for a load placed at mid-latitudes and drops off symmetrically as the initial position of the disk load is placed closer to either the rotation axis (θ_L is small) or the equator ($\theta_L \rightarrow 90^\circ$) (Figures 5.5C, 5.7C). In the latter case, the final TPW is small because the load is already close to the equator (Figure 5.4C), and thus the TPW speed is limited by this proximity (e.g., see the $\theta_L = 85^\circ$ case in Figure 5.5C). The explanation for the former, small θ_L case, is more complicated. In the former case, when the load is placed close to the rotation axis there is a near cancellation between the load induced forcing and the remnant bulge stabilisation since $Q_{eff} = 1$, i.e., the net forcing is small. In this case, even though the total displacement of the pole is large (the equilibrium TPW is $\sim 45^\circ$; Figures 5.2 and 5.4C), the TPW speed will be small throughout the reorientation of the pole from its initial to final position.

In the $Q_{eff} = 0.1$ case (Figure 5.7C), the net TPW is small because the remnant bulge is stronger than the load-induced forcing (Figure 5.2) and thus the TPW speed is limited by the small net displacement of the pole. The symmetry evident in Figure 5.7C is particularly interesting given that the equilibrium TPW for these Q_{eff} values in Figure 5.2 do not exhibit symmetry across mid-latitudes. The above arguments suggest that the symmetry evident in Figure 5.7C will disappear for Q_{eff} values progressively greater than 1.

As a final point in regard to Figure 5.4C, the fact that the TPW predicted in the long-time limit is linearly related to θ_L is consistent with the $Q_{eff} = 1$ case in Figure 5.2. Note, once again, that the time-dependent TPW predictions in Figure 5.4C converge to the equilibrium values given by the analytic expression (5.28).

In Figure 5.8 we extend the analyses described above to consider the sensitivity of the predictions to a change in the elastic thickness of the lithosphere, LT. The solid line in the figure is the TPW predicted for the standard case, and it is reproduced from Figure 5.3. As discussed above, this calculation adopts a value of $Q_{eff} = 1.0$. To isolate the impact of LT on the adjustment of

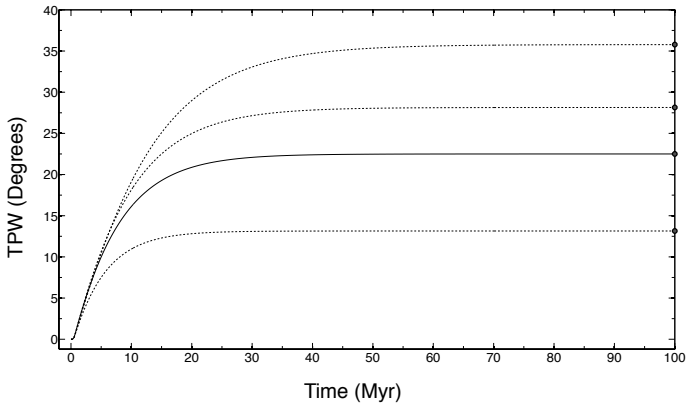

Figure 5.8: Predictions of surface-load induced TPW as a function of time computed using a Maxwell viscoelastic Earth characterised by upper and lower mantle viscosities of 5 $\times$ 10^{20} Pa s and 10^{22} Pa s, respectively. The surface load is an axisymmetric disk centred at an initial colatitude θ_L = 45°. All calculations use the full rotational stability theory in which stabilisation by both the delayed, viscous adjustment of the rotational bulge and the remnant bulge are included (equation 5.19 with $\mathbf{I}^R(t)$ given by equation 5.25). Solid line: An elastic lithospheric thickness of LT = 15 km, and a disk size that is increased such that the parameter Q_{eff} is varied from 0.0 to 1.0 in the first 1 Myr of the simulation (see text) and then retained for all time. This is the test model case discussed in the text. Dashed lines (from top to bottom): LT = 5 km, 10 km, and 25 km; for these cases, the uncompensated sizes of the loads (Q'; equation 5.24) are varied such that the product Q' (1 + k_f^L) remains identical to that used to generate the solid line. The solid circles on the right-hand side of the figure are the equilibrium TPW predicted for these cases (see equation 5.28).

the rotational bulge from its direct impact on the load via isostatic compensation, we vary LT from 5–25 km (dashed lines in Figure 5.8) while holding the product $Q'(1+k_f^L)$ constant and equal to the LT $=$ 15 km case. Following our definition for $Q_{eff} \equiv Q'\alpha$ (where α is defined in equation 5.29), keeping $Q'(1 + k_f^L)$ constant requires that we vary Q_{eff} appropriately. As a result, the long-time limits of the TPW predictions are distinct, and they converge to the equilibrium values expected on the basis of equation (5.28). A more significant difference is the timescale over which these predictions converge to their respective equilibrium values. In particular, as LT increases from 5 km to 25 km, $t_{1/2}$ decreases from $\sim$ 9 Myr to $\sim$ 4 Myr. As mentioned in the discussion of Figure 5.3, this trend is primarily due to the reduced amplitude of TPW associated with the remnant bulge

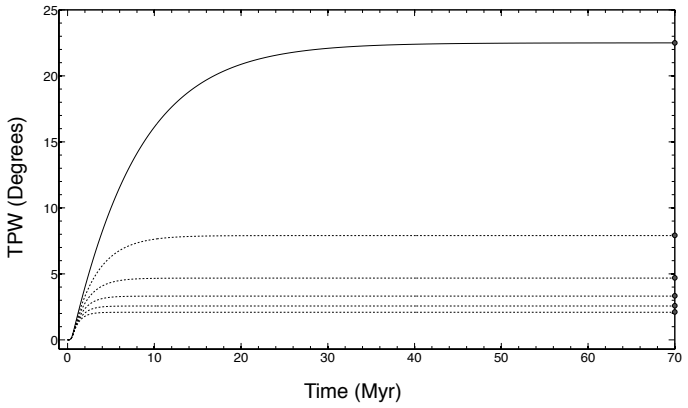

Figure 5.9: Predictions of TPW as a function of time using the test model case corresponding to the solid line in Figure 5.3 (reproduced here also as solid line), as well as additional simulations in which stabilisation due to a stable excess ellipticity is included (see text). From top to bottom (dotted lines), simulations using excess ellipticity values of 0.002, 0.004, 0.006, 0.008, and 0.01, respectively (see text). The solid circles on the right-hand side of the figure are the equilibrium TPW predicted for these cases.

stabilisation (third term on the right-hand side of equation 5.19). The effect of this stabilisation on the perturbed pole position is constant, whereas the stabilisation associated with the delayed adjustment of the viscous rotational bulge (fifth term of equation 5.19) evolves with time. Given a comparable effective loading ($Q'(1 + k_f^L)$), the timescale of the TPW predictions in Figure 5.8 depends on the time-evolving relative importance of these effects.

In addition to the remnant bulge, a planet may also have a stable excess ellipticity arising, for example, from long timescale convective flow in the interior. On present-day Earth, this excess ellipticity is observed to contribute an additional ~ 0.01 to the degree-2 k tidal Love number when averaged over the two principal equatorial axes [Chambat et al., 2010]. Figure 5.9 shows the stabilising effect of excess ellipticity on our standard scenario. An excess ellipticity of 0.002 (top-most dotted line), or 20% of Earth's present-day value, reduces the final TPW by over 60% relative to the case without this stabilisation. The reduction is over 90% if we adopt the Earth's present-day excess ellipticity (bottom-most dotted line). These predictions include the combined effects of the

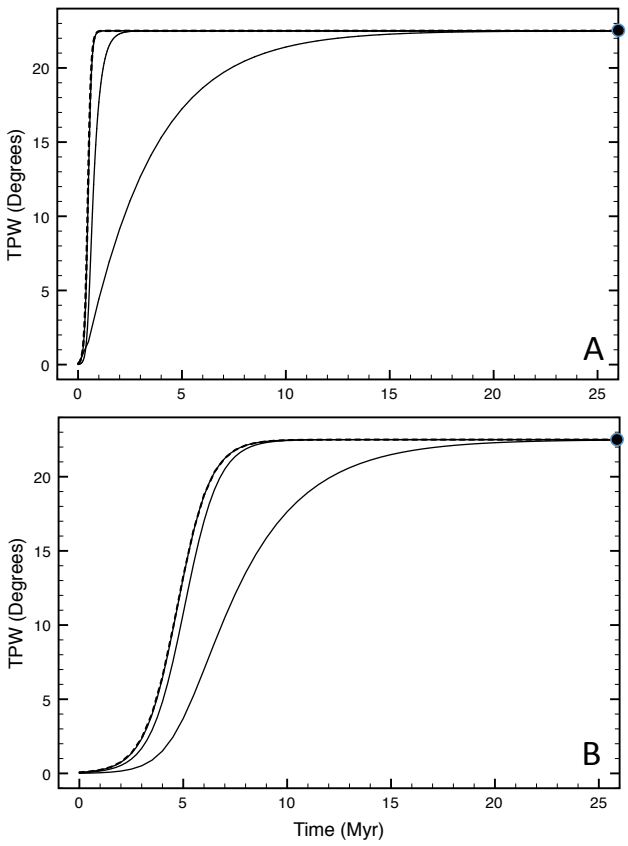

Figure 5.10: Predictions of surface-load induced TPW as a function of time computed using a Maxwell viscoelastic Mars model characterised by an elastic lithospheric thickness LT = 110 km, and mantle viscosities of 10^{21} Pa s, 10^{22} Pa s, and 10^{23} Pa s (solid curves from left to right, respectively). The surface load is an axisymmetric disk centered at an initial colatitude $\theta_L = 45^\circ$. The disk size is increased such that the parameter Q_{eff} is varied from 0.0 to 1.0 in (A) the first 1 Myr and (B) the first 10 Myr of the simulation, and then retained for all time. The dashed line on each frame is a solution in which the rotational bulge stabilisation is excluded (i.e., the term involving T_1 in equation 5.19 is set to 0). The solid circle on the right-hand side on each frame is the TPW predicted using the equilibrium (i.e., infinite time) theory of Matsuyama et al. [2006] (see equation 5.28).

remnant bulge and the excess ellipticity. However, even in the absence of an elastic lithosphere, any long-term excess ellipticity would still contribute a significant stabilisation towards a planet's rotation [Creveling et al., 2012].

5.3.2 Time-dependent TPW on Mars: some illustrative examples

Figure 5.10 shows a set of illustrative simulations of time-dependent TPW on Mars. The predictions are once again based on equation (5.19), with the inertia tensor perturbation associated with the direct effect of the surface mass load given by equation (5.25). The elastic and density structure of the Mars model is taken from Zharkov & Gudkova [2005]. The viscosity of the model is discretised into two layers: a uniform elastic (infinite viscosity) lithosphere of thickness 110 km and constant mantle viscosities of 10^{21} Pa s, 10^{22} Pa s, and 10^{23} Pa s (the three solid lines on each frame). In all cases, the axisymmetric load is placed at $\theta_L = 45^\circ$. In Figure 5.10A, the size of this load is assumed to increase from zero to $Q_{eff} = 1$ in the first 1 Myr of each simulation, as in Figures 5.3–5.8. For a convective forcing, this is unrealistically short, and therefore, in Figure 5.10B, the timescale is increased by an order of magnitude.

In each frame of the figure, the dashed line represents a simulation in which the stabilising effect of the delayed adjustment of the rotational bulge is excluded. Thus, as discussed in relation to Figure 5.4B, at each stage in the loading, the dashed line represents the TPW computed using the equilibrium theory of Matsuyama et al. [2006] (equation 5.28). For loading timescales of either 1 or 10 Myrs, stabilisation associated with the rotational bulge in the case of a mantle viscosity of 10^{21} Pa s introduces a negligible lag in the TPW prediction relative to this equilibrium theory. Conversely, this lag only becomes significant over this timescale of loading when the mantle viscosity exceeds 10^{22} Pa s. The viscosity of Martian mantle is not well constrained, but most recent studies adopt values from $\sim 10^{19}$ Pa s to 10^{21} Pa s, where the range reflects uncertainties associated with both temperature and composition [e.g. Hauck & Phillips, 2002; Williams & Nimmo, 2004; Breuer & Spohn, 2006]. This suggests, with reference to Figure 5.10, that stabilisation associated

with the Martian rotational bulge is unimportant for loads that evolve over timescales longer than ~ 1 Myr.

5.4 Final Remarks

We have derived and applied a non-linear theory for predicting time-dependent TPW of terrestrial planets subject to (internal or external) mass redistribution. The theory accounts for stabilisation associated with both the delayed viscous readjustment of the rotational bulge and TPW-induced stresses in an elastic lithosphere (i.e., a remnant bulge). Our derivation is an extension of the treatment by Ricard et al. [1993] to include remnant bulge stabilisation and it assumes, following that work, that load-induced inertia tensor perturbations have a timescale longer than the viscous response of the planetary model to an applied tidal-effective forcing. Our derivation may also be understood as an extension of the equilibrium rotational stability theory of Willemann [1984] and Matsuyama et al. [2006] to incorporate time dependence.

Previous work has shown that the remnant bulge can significantly reduce the amplitude of TPW relative to calculations which incorporate stabilisation by the viscoelastically deforming rotational bulge alone [Willemann, 1984; Matsuyama et al., 2006; Daradich et al., 2008]. Our new calculations demonstrate that the remnant bulge also acts to reduce the characteristic timescale of the TPW (e.g., Figs. 5.3 and 5.8). This reduction in timescale can be understood by inspection of the equations governing TPW; namely, the eigenvalue problem in equation (5.2) with the total inertia tensor perturbation given by equation (5.16). The remnant bulge stabilisation is embodied within the third term on the right-hand side of the latter equation. This term depends on the thickness of the elastic lithosphere and the original orientation of the rotation axis, and it is stationary in time. Thus, if stabilisation by the remnant bulge is switched on (as in Figure 5.3), or if it is strengthened by increasing the thickness of the elastic lithosphere (as in Figure 5.8), then it will moderate the time dependence associated with the delayed viscous adjustment of the rotational bulge (the fourth

term on the right-hand side of equation 5.16).

The remaining calculations based on the Heaviside-type loading of a viscoelastic Earth model reveal other interesting sensitivities. For example, the peak TPW speed is linearly dependent on the effective load size, Q_{eff}, while the time to reach half the final (equilibrium) displacement of the pole, $t_{1/2}$, is linearly proportional to the adopted lower mantle viscosity. Also, the peak TPW speed decreases monotonically with increasing ν_{lm}, but this decrease is not a linear function of ν_{lm}.

Finally, using current estimates of mantle viscosity for both Earth and Mars, our calculations suggest that the transient stabilisation associated with the rotational bulge will be significant for Earth but negligible for Mars in the case of forcings with timescale 1 Myr or longer. That is, the predicted TPW on Mars driven by forcings over these timescales will track the equilibrium response, where the latter includes stabilisation associated with the remnant bulge [Willemann, 1984; Matsuyama et al., 2006]

The calculations presented in this chapter all converge, as they should, to the equilibrium solution a long time after the application of the loading. In future work we will further extend the theory described here to incorporate a viscoelastic, rather than elastic, lithosphere. In this case, TPW should trend toward the equilibrium theory discussed by Willemann [1984] and Matsuyama et al. [2006] over timescales that are long, but shorter than the viscous relaxation time of the viscoelastic lithosphere. However, once the timescale of the loading exceeds this relaxation time, stabilisation by the remnant bulge will disappear, and the pole will further reorient so as to bring the load to the equator, as predicted by the classic equilibrium theory of Gold [1955].

5.5 A Note on Time Step Sizes in the Numerical Implementations

As mentioned in § 5.2.1, the eigenvalue approach discussed in this article is based on the assumption that the timescale of loading is similar to or longer than the reorientation timescale of the rotation pole. A further long-timescale condition was imposed in equation (5.12) [following Ricard et al., 1993].

In numerically implementing the theory described in § 5.2.3 and § 5.2.4, we have (empirically) found that there are limitations in the numerical procedure that are consistent with such long-timescale assumptions. Consider the principal axis associated with the maximum moment of inertia of the viscous component of the rotational bulge (whose adjustment is induced by the rotational-potential perturbation but delayed by viscosity, i.e., the second and fourth term on the right-hand side of equation 5.16), and the principal axis of maximum moment associated with the load (last term of equation 5.16). The numerical solution will only converge if both of these axes are on the same side of the rotation pole in the previous time step (for the initial step, this is $\mathbf{\Omega}$), which requires that sufficiently large time steps are taken. The minimum bound of such time steps depends on the planetary model used (which impact k_f^T and T_1). This limitation may be thought of as a requirement that the time steps are sufficiently long to ensure that the viscous portion of the rotational bulge will begin to adjust towards the latest perturbation of the rotational potential, thus inherently satisfying the long-timescale assumptions underlying the rotational stability theory.

Le cœur a ses raisons,
que la raison ne connaît point.

Blaise Pascal, *Pensées*

6

Ancient Ocean on Mars

Reassessing the hypothesis using the global distribution of valley networks

The surface of Mars is marked by a variety of geologic and topographic features that suggest the past existence of a global hydrological system. These include contacts that resemble shorelines [Parker et al., 1989, 1993; Clifford & Parker, 2001], deltaic deposits [di Achille & Hynek, 2010, and references therein], sedimentary deposits [Lewis et al., 2008; Malin & Edgett, 2000], valley networks [Carr, 1995; Fassett & Head, 2008; Hynek et al., 2010; Matsubara et al., 2013], amongst other terrain forms [e.g. Moscardelli, 2014]. Despite the abundance of such features, the existence of an ancient ocean, or even a sustained and/or widespread hydrological cycle, remains controversial [e.g. Ghatan & Zimbelman, 2006; Leverington, 2011]. The controversy mostly arise from the difficulty in reconciling the past conditions predicted by climate models and the conditions required to sustain water in liquid form for long periods of time [e.g. Fairén, 2010; Wordsworth et al., 2013].

Several recent studies have used topography to investigate the Martian ocean hypothesis. Perron et al. [2007] showed that the long-wavelength topography of continuous contacts along the Martian surface is consistent with deformation caused by true polar wander (TPW) and that the preferred TPW path satisfied a strong dynamic constraint that the massive Tharsis volcanic province remain on the planet's equator (see below). Thus, the topographic contacts could be identified as ancient shorelines. In contrast, di Achille & Hynek [2010] analysed the elevations of ancient deltaic deposits and argued that they lie close to a present-day equipotential surface, concluding that these putative ocean markers have undergone little post-depositional deflection from TPW or other processes.

In this chapter, we revisit the Martian ocean hypothesis by examining the topography of another possible equipotential marker — fluvial valley networks. Specifically, we are interested in the terminus of each valley network (henceforth, VNT) on the Martian surface, especially near the dichotomy boundary. The locations and elevation of these VNTs may shed additional light on whether ancient sea level, as inferred from the VNTs, is consistent with present-day topography, or whether the elevation of the VNTs shows long-wavelength deflection consistent with TPW. In considering the latter, the size and location of the Tharsis rise is important. The Tharsis rise is a dominating feature of the non-hydrostatic component of the aeroid [Smith et al., 1999], particularly at spherical harmonic degree 2, which controls TPW. Since long-term TPW is driven by the degree-2 non-hydrostatic moments of inertia [Gold, 1955; Goldreich & Toomre, 1969], the Tharsis rise, being centered near the equator, strongly stabilises the planet against any TPW that would move Tharsis significantly off the equator. That is, as noted by Perron et al. [2007], any TPW path(s) would have been limited to the great circle $\sim 90^\circ$ from the center of Tharsis. Since most of the valley networks formed after the emplacement of Tharsis [Phillips et al., 2001; Hynek et al., 2010], any palaeopole deduced from the present elevation of VNTs would have to satisfy this strict dynamic constraint.

In the next section, we describe the methodological and mathematical details of our analysis.

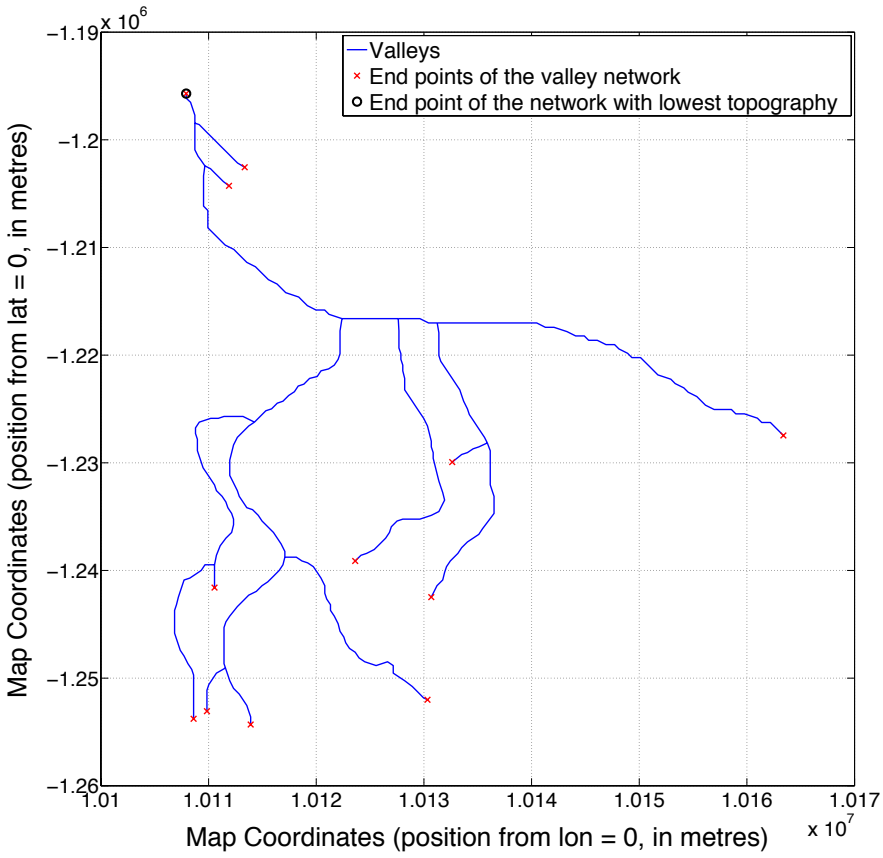

Figure 6.1: A valley network example showing its end points and the identification of the lowest end point (i.e., the VNT).

Preliminary results are discussed in § 6.2. Finally, remarks and directions for future work are described in § 6.3.

6.1 Methods and Data

Our goal is to test whether the elevation pattern of valley networks support the hypotheses that: (i) an ancient Martian ocean existed; and (ii) that TPW produced a discernible long-wavelength deflection of VNTs that were initially close to an equipotential surface.

We use the global map of Martian valley networks produced by Hynek et al. [2010] in conjunction with the 128 pixels per degree topographic map from the Mars Global Surveyor (MGS)

Mars Orbiter Laser Altimeter (MOLA) Mission Experiment Gridded Data Record (MEGDR) [Smith et al., 2003] to find the VNT of each of the 9879 mapped valley networks (e.g. Figure 6.1). Since the sea level of the putative ocean likely varied across different periods, we need to limit our choice of valley networks by age. In particular, studies have suggested that most of the Martian valley networks formed in the Noachian period [Carr, 1995; Hynek & Phillips, 2003; Fassett & Head, 2008; Hynek et al., 2010] and mostly post-dated the emplacement of the Tharsis rise [Phillips et al., 2001]. Therefore, we select only the valley networks entirely contained within Noachian-aged terrains. This age distinction is achieved by comparing the valley network coordinates against the Mars Global Geologic Map M-1082 A, B, and C [Skinner et al., 2006]. Figure 6.2 shows the Noachian VNTs as black points plotted on the Martian topographic map. We note that the age of terrains into which the valley networks incised represents only an upper limit for the age of the valley networks, since the valleys could have formed during any subsequent period after the formation of the terrain.

The next step is to identify all candidate VNTs that would have drained directly into the putative ocean that covered the plains north of the dichotomy boundary. By overlaying the MOLA topographic map with the age-separated valley networks (with their associated VNTs marked), we manually examine all the valley networks along the entire length of the dichotomy boundary region. The VNTs are separated into different categories based on criteria such as: flow direction and geometry (both of the valley network and neighbouring networks); number of tributaries; and proximity to valley networks on younger terrains. These categories are used to assess the (qualitative) likelihood of the selected VNTs being at or near an ancient shoreline. This process yielded 181 VNTs (highlighted cyan in Figure 6.2), 95 of which were attributed higher confidence than the rest and will form one of the groups in the Monte Carlo analysis described in § 6.2 below. We emphasise that only the valley network map and the MOLA topography data were used in the process of manually selecting the VNTs; this limits any potential bias in the selection procedure (e.g. from any visual connection to the Arabia or Deuteronilus contacts).

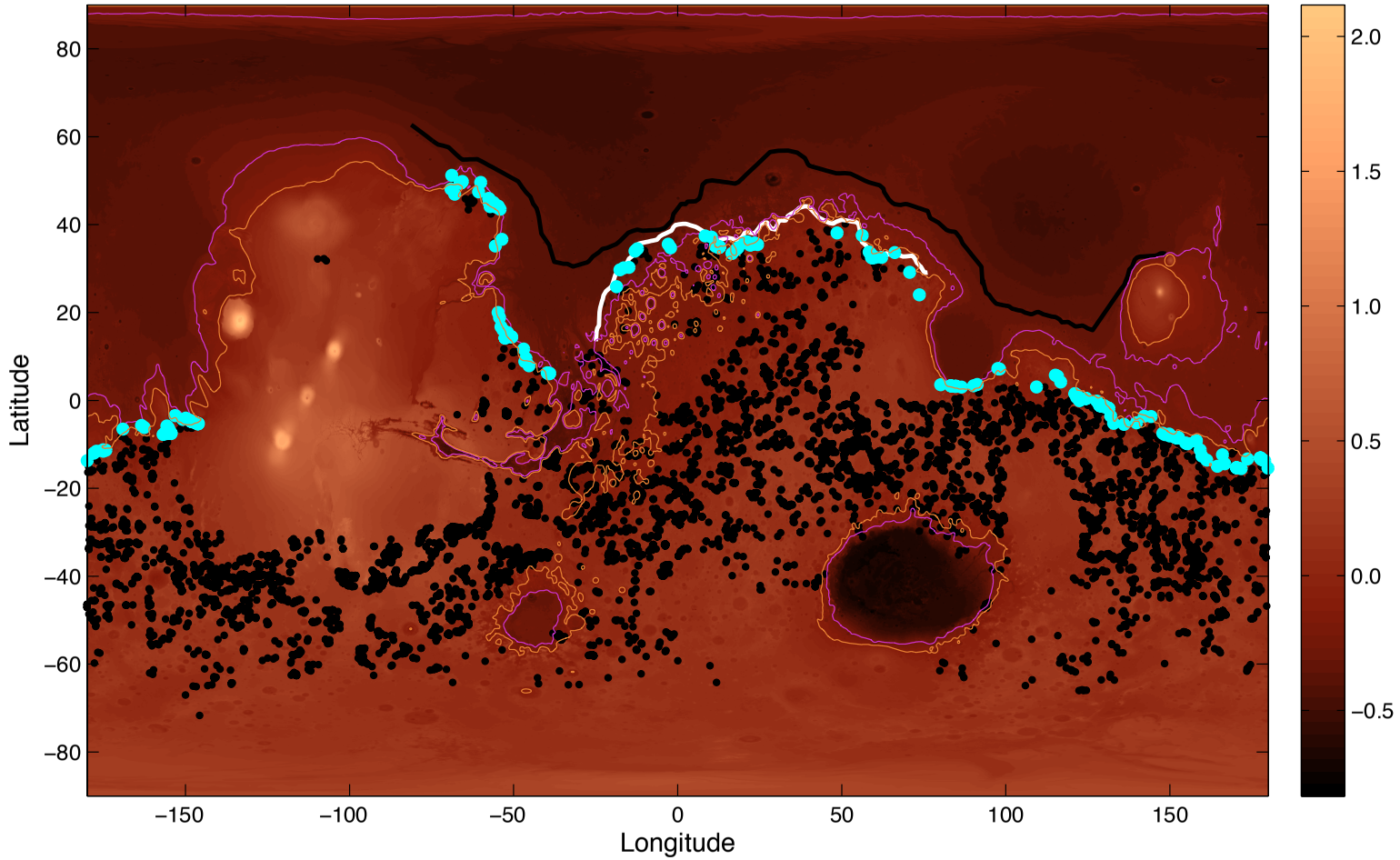

Figure 6.2: Topography map of Mars with the colour bar in units of km. The VNTs of Noachian valley networks are shown as black dots, with the manually selected near-shore VNTs (see § 6.1) highlighted in cyan. The contours show the equipotential level representing the sea surface in the case of (magenta) di Achille & Hynek [2010] and (orange) after the incorporation of TPW-driven deformation associated with the mean palaeopole predicted by this study with its associated topography. Note that both contours are Gaussian smoothed (with 5 passes) for clarity, sacrificing short-wavelength details such as small craters, off-shore islands, and the extent of inland canyons. Also plotted for reference are the Arabia shoreline (white) and Deuteronilus shoreline (black) adopted by Perron et al. [2007] in their analysis.

6.1.1 Accounting for Possible TPW

Following Perron et al. [2007], we account for the possibility that Mars may have undergone TPW subsequent to the disappearance of water from its surface. Using fluid Love number theory, we can calculate the topographic response to TPW. Given an ancient North Pole at (θ', ψ') in a coordinate system in which the present-day North Pole is at $(\theta = 0, \psi = 0)$, the centrifugal potential of this palaeo-rotational state is given by [Lambeck, 1980]

$$\varphi(\theta, \psi) = \frac{1}{3}\omega^2 a^2 - \frac{1}{3}\omega^2 a^2 P_{2,0}(\cos\gamma)\,, \tag{6.1}$$

where ω is the rotation rate of the planet, a is its mean radius, and γ is the angular distance between (θ, ψ) and (θ', ψ'). The degree-2, order-0 Legendre polynomial is given by

$$P_{2,0}(\cos\eta) = \frac{1}{2}\left(3\cos^2\eta - 1\right). \tag{6.2}$$

If we assume a constant ω, the difference between the palaeo-centrifugal potential and the present-day potential is

$$\Lambda(\theta, \psi) = \frac{1}{3}\omega^2 a^2 \left[P_{2,0}\left(\cos\gamma\right) - P_{2,0}\left(\cos\theta\right)\right]. \tag{6.3}$$

The topographic response to a TPW event is then [Mound & Mitrovica, 1998]

$$\Delta T(\theta, \psi) = \frac{\Lambda(\theta, \psi)}{g}\left[h_f - (1 + k_f)\right] + Z\,, \tag{6.4}$$

where g is the gravitational acceleration at the surface, h_f and k_f are the degree-2 h and k fluid tidal Love numbers, and Z is a constant shift factor introduced to account for the fact that the equipotential defining the present-day aeroid is not necessarily the same as the equipotential level at the ancient sea surface [Dahlen, 1976]. An illustration of the geometry of ΔT is shown in Fig. 6.3. In general, values for h_f and k_f depend on the internal structure of the planet. For the purpose of

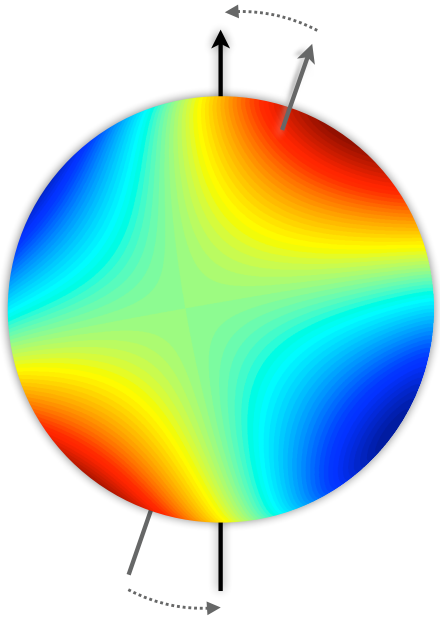

Figure 6.3: An example of the geometry of the topographic response to TPW (i.e., ΔT in equation 6.4) plotted on a globe, viewed from above the equator $\sim 80^\circ$ west of the palaeo-North Pole. The palaeopole is represented by the grey straight arrow, whereas the present-day pole is in black (the dotted arrows denote the migration of the pole). The range of colours from red (through green) to blue denote a range of topographic deformations from positive to negative. Note the dominance of a degree-two, order-one spherical harmonic geometry of ΔT.

this chapter, we adopt the values consistent with a Mars model having an elastic lithosphere that is 200 km thick: $h_f = 1.663$ and $k_f = 0.899$ [Sohl & Spohn, 1997; Perron et al., 2007].

Using equations (6.3) and (6.4), we can correct the present-day topography for the deformation that would have been caused by the rotation pole migrating from its ancient orientation. Specifically, we seek to find a palaeopole that yields a ΔT that best fits the present-day topography of the VNTs, where the fit is based on the minimisation of the root-mean-square standard deviation.

To check for the effect of outliers, we also assessed the fit using a maximum-likelihood method based on an L1 norm [Aster et al., 2005, § 2.4]. The two approaches resulted in best-fit palaeopoles that are less than 5° apart. For this reason, we adopt and only cite the least squares in the remainder of this chapter.

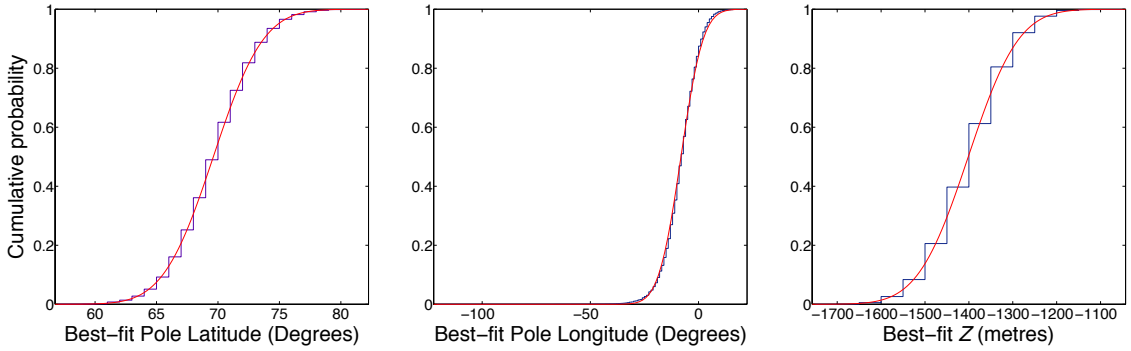

Figure 6.4: Cumulative distribution functions of, from left to right in blue steps, the palaeo-North Pole's latitude, longitude, and the Z potential shift, respectively. Fitted on top (in red) are the best-fit normal cumulative distribution functions.

6.2 Results and Discussion

In order to estimate a statistical distribution for our results in the absence of a priori knowledge of the data errors, we employ a Monte Carlo algorithm to perform case resampling (with replacement) of the selected VNTs. This resampling is performed separately (i.e., stratified) for the subset of 95 VNTs that was ascribed higher confidence. Each set of resampled data is assembled using a random number generator (seeded with time) with uniform distribution. For each of the resulting sets, we compute a misfit as described in the previous subsection. In total, 11200 iterations were performed.

Figure 6.4 shows the cumulative distribution functions (CDFs) of the latitude and longitude of the best-fit palaeopoles and the uniform shift Z resulting from the Monte Carlo analysis. The red line on each frame is the CDF of the best-fit normal distribution*. The computed mean values of the latitude, longitude, and potential shift (Z) of the palaeopole, together with their associated 95% confidence limits, are $70°\text{N} \pm 6°$, $8°\text{W} \pm 16°$, and -1400 m $\pm$ 200 m, respectively. (Note that the values are rounded to the resolution chosen for our palaeopole fitting algorithm, which is $1°$ for the

*The best-fit longitude would be better approximated with a t-distribution, but the resulting mean and standard deviation differ by less than $1°$ relative to those obtained from the assumption of a normal distribution.

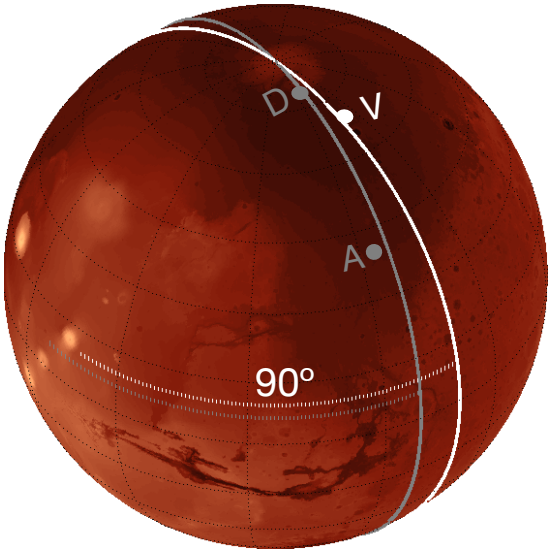

Figure 6.5: Map of Mars centered around the mid-latitude region west of Arabia Terra. The white dot (labelled 'V') denotes the location of the mean palaeopole predicted by the method described in § 6.1. The palaeopoles predicted by Perron et al. [2007] on the basis of the Arabia and Deuteronilus shorelines are shown in grey, labelled 'A' and 'D', respectively. The longitudinal great circle 90° away from the center of Tharsis (9.8°N,258.6°E; see Matsuyama & Manga, 2010) is also shown in white; the grey line is the equivalent but based on the Tharsis center location predicted by Zuber & Smith [1997].

geographical coordinates, and 50 metres for Z.) The location of the mean palaeopole is shown in Figure 6.5, labelled 'V'.

As mentioned above, the path of any TPW deforming the VNTs is unlikely to diverge far from the great circle $\sim 90^\circ$ away from the center of Tharsis. Two great circles, based on two different estimates of centroid of Tharsis, [Zuber & Smith, 1997; Matsuyama & Manga, 2010], are superimposed on Figure 6.5. Clearly, our inference of the palaeopole location is consistent with this relatively stringent dynamical constraint.

There is a $\sim 30^\circ$ difference between in the location of our mean palaeopole and the palaeopole inferred by Perron et al. [2007] on the basis of the putative Arabia shoreline (labelled 'A' in Figure 6.5), despite the fact that our predicted shoreline location is very close to the Arabia contact. In contrast, the palaeopole inferred by Perron et al. on the basis of the topography of the Deuteronilus contact (labelled 'D' in Figure 6.5) is $\sim 10^\circ$ from our VNT-inferred palaeopole.

The Arabia contact is inferred to be older than the Deuteronilus contact [Clifford & Parker, 2001], and there is morphological evidence that the latter formed during the Late Hesperian or even Early Amazonian period [Erkeling et al., 2012]. However, the age of the VNTs relative to these topographic features is uncertain. Assuming a unidirectional TPW path, the inferences in Figure 6.5 suggest that the age of the VNTs is intermediate to the Deuteronilus and Arabia ages. Assuming a drying trend in the putative Martian ocean, the mean present-day elevation of these features provides a somewhat coarse test of relative age. The mean elevation of the VNTs is -1.76 km, whereas the Arabia and Deuteronilus shorelines have a mean elevation of -1.68 km and -3.76 km, respectively [Clifford & Parker, 2001]. This is consistent with our argument based on the inferred palaeopole locations in Figure 6.5 that the rotation axis moved from 'A' to 'V' to 'D' and then ultimately to the present-day pole position. Finally, we note that the VNTs we have selected as the most robust extend over $\sim 290^\circ$ of longitude, a much longer distance than the Arabia or Deuteronilus shorelines cited by Perron et al. [2007] (see Figure 6.2) and in this regard the inference of the palaeopole location associated with the VNTs may be more robust than those based on the shorelines.

Figure 6.2 shows the location of a palaeo-shoreline inferred by di Achille & Hynek [2010] on the basis of their analysis of deltaic deposits by di Achille & Hynek [2010] (magenta) and the location we infer after correction of present-day topography for the TPW implied by the palaeopole labeled 'V' in Figure 6.5 (orange). The discrepancy between these shorelines is due to a combination of TPW-induced perturbation in topography and the ~ 1 km difference in Z cited by di Achille & Hynek [2010] relative to our estimate. We note that our shoreline reconstruction provides a significant improvement in tracing the location of the VNTs in both northeast Arabia Terra to the northwest of Isidis Planitia (a region from roughly 25°N to 40°N and 55°E to 75°E) and along Elysium Planitia (roughly, 10°S to 10°N and 120°E to 170°E). In both regions, the area between the two shoreline reconstructions is nearly devoid of valley networks of any age. Therefore, if the ancient shoreline coincided with the inference of di Achille & Hynek [2010], then it would mean

that there was either an abrupt and coherent termination of incisions a few hundred kilometres onshore, or a complete erasure of all valleys in a region extending from the VNTs to the reconstructed shoreline, which extends laterally over thousands of kilometres. The latter scenario is unlikely, but the former may be possible if the local topographic gradient of the entire region decreases abruptly. We note that most of the valleys in these areas terminate at sharp jumps in the local topographic gradient that are suggestive of cliffs. Beyond these cliffs, for $\sim$ 100 km towards the northern plains, the topographic gradients are comparable to those directly south of the cliffs (and VNTs), and they ultimately transition into the flat, smooth topography characteristic of the northern plains. One would thus expect at least some incisions in the area in front (i.e., northward) of the cliffs. We conclude that the di Achille & Hynek [2010] reconstruction of palaeo-sea level is inconsistent with the location of the VNTs.

Overlain on Figure 6.2 are the Arabia and Deuteronilus contacts. Our shoreline reconstruction traces the Arabia shoreline quite well along its eastern section. On the western flank of Arabia Terra, the Arabia shoreline traces the VNTs well, but both reconstructed shorelines would place these features under water. Neither present day topography nor any topography constructed by correcting for TPW would fit the location of VNTs in this section of Arabia Terra without significantly misfitting the location of VNTs along the western edge of Chryse Planitia, Elysium Planitia, or both.

Our data base of VNTs excludes some valley networks even tough they are located in areas identified as Noachian terrains and they appear to form a coherent 'front'. Their exclusion is almost always due to the presence of other valleys that are in close proximity and that show similar trends but that are located on younger (i.e., Hesperian or Amazonian) terrains. The fact that these VNTs are within regions where our reconstructed shoreline misfits the subset of VNTs adopted in our inference of TPW suggests that the reconstructed shoreline may be of Hesperian age. To illustrate this possibility, Figure 6.6 distinguishes VNTs that exist on Hesperian and Noachian terrains. The map shows a geographic consistency between the location of Hesperian-age VNTs and re-

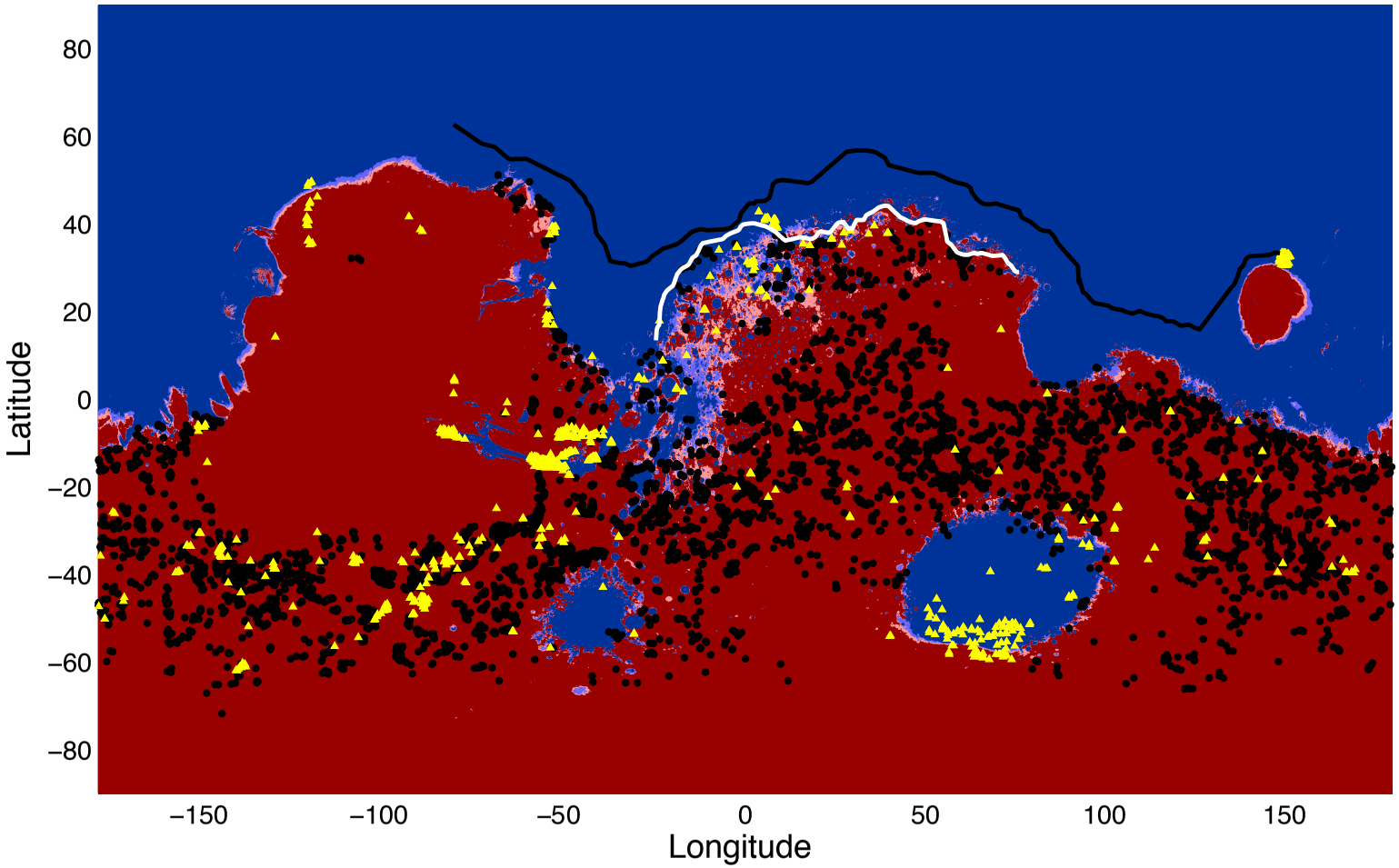

Figure 6.6: Map of Mars with the colours delineating the (un-smoothed) contour shorelines inferred by the present study (i.e., the orange contour in Figure 6.2). Areas in red have topography higher than shore, blue are areas below, whilst the pink and light blue are the areas $\pm$200 m around the contour. The VNTs of Noachian valley networks are shown as black dots, whereas the Hesperian ones are represented by yellow triangles. Also plotted for reference are the Arabia shoreline (white) and Deuteronilus shoreline (black) used by Perron et al. [2007] in their analysis.

constructed shoreline position, both around Hecates Tholus volcano (north of Elysium Mons) and along Valles Marineris even though these VNTs were not included in the Monte Carlo analysis discussed above. We note, however, that the location of VNTs along Valles Marineris could be fit by correcting for a wide range of palaeopole locations due to depth and steep edge of the topography in this region.

6.3 Future Work

Given the age uncertainties of some Noachian valley networks discussed above, future work should include Hesperian networks in the Monte Carlo analysis and examine any differences in both palaeopole predictions and the reconstructed shorelines. Furthermore, just as there are Hesperian valley networks that suggest some VNTs on Noachian terrains may have been active or have formed during the Hesperian, there are regions containing Amazonian-age VNTs that suggest that VNTs on Noachian and Hesperian terrains may be significantly younger than these terrains. A particularly problematic area is the northern rim of Arabia Terra (roughly between 10°W to 50°E), where there is a large number of valley networks on Amazonian terrains. Although most of the associated VNTs appear to drain into the craters that dot the entire region, a number of them could impact the age interpretation of neighbouring valley networks on Noachian and Hesperian terrains that appear to drain into the northern plains. We note, in this regard, that there is growing evidence suggesting that valleys from the Amazonian period may be glacial in origin [e.g. Fassett et al., 2010; Hobley et al., 2014].

Summary

This thesis has been concerned with the time-dependent stability of true polar wander (TPW) on terrestrial planets. In Chapter 2, we derived a linearised rotational stability theory that permits predictions of time-dependent TPW on a Maxwell viscoelastic Earth with a load-induced perturbation in the inertia tensor. The theoretical formalism, which is based on recent advances in ice-age rotation theory, incorporates the stabilising effects of a remnant rotational bulge associated with non-zero elastic strength in the lithosphere, as well as an excess ellipticity of the planet's background strength that is stable over the timescale of the forcing. We demonstrated that this linearised theory can, in the cases of loading at mid-latitudes, predict TPW of over 20° to better than 5% accuracy.

We then applied this new theory to investigate two recent, palaeomagnetically-derived inferences of TPW on Earth. In Chapter 2, we showed that suggestions of quasi-cyclical TPW with amplitude of 10°–20° and timescale $\mathcal{O}(1\,\mathrm{Myr})$ during the Late Cretaceous are physically implausible. We also argued, in Chapter 3, that the excess ellipticity of the Earth's figure driven by plate subduction and deep mantle superplumes is responsible for the muted polar wander over the last 100 Myr, a period in which the rotation axis has remained within 6° of its present location. Specifically, we showed that TPW during this time window is consistent with convection-induced perturbations to the Earth's inertia tensor of order 20 per cent or less of the perturbation associated with the present-day excess ellipticity; this upper bound would be higher if the Earth's lithosphere retains any significant elastic strength over such long timescales.

In Chapter 4, we revisited the prediction, made by previous studies of ice-age Earth rotation, of a long-term drift in the orientation of the rotation axis (of order several degrees) over the Plio-

Pleistocene. These studies, based on a traditional theoretical treatment, have argued that this drift may be responsible for transitioning the Earth System out of the ice age. We noted that revised theories of Earth rotation that incorporate a more accurate treatment of the Earth's background ellipticity [Mitrovica et al., 2005; Cambiotti et al., 2010; Mitrovica & Wahr, 2011] do not include the permanent shift in the orientation of the rotation axis, known as unidirectional TPW, that is predicted by traditional treatments. We also developed the first physical and mathematical framework for understanding both the appearance of this term in the traditional theory and its absence in the revised theory. Furthermore, using the revised theory to predict ice-age induced TPW over several time intervals, we demonstrated that the net displacement of the pole predicted by earlier studies disappears. Therefore, we concluded that the cause(s) that drove the Earth out of the ice age must be sought elsewhere.

Returning to TPW over longer timescales, we extended in Chapter 5 a treatment of TPW that has been widely adopted in studies of convection-driven TPW [Ricard et al., 1993] to derive a non-linear, time-dependent rotational stability theory that incorporates the impact of both a remnant rotational bulge and stable excess ellipticity. We illustrated the theory using a suite of idealised surface-loading scenarios applied to models of both Earth and Mars. These calculations demonstrate that remnant bulge stabilisation reduces both the amplitude and timescale of TPW compared to traditional treatments in which this physics is omitted. Furthermore, given current estimates of mantle viscosity in both planets, our calculations indicate that departures from the equilibrium (i.e., infinite-time) orientation of the rotation pole in response to forcings with timescale of 1 Myr or longer are significant for the Earth, but negligible for Mars.

The final chapter of the thesis revisited a different aspect of TPW. Using topography data from the Mars Orbiter Laser Altimeter, a global map of valley networks by Hynek et al. [2010], and the Mars Global Geologic Map M-1082 A, B, and C [Skinner et al., 2006], we revisited the question of whether TPW deformed geological markers of an ancient ocean on Mars. Two recent studies have argued in support of the existence of an ancient ocean on early Mars, but have reached dif-

ferent conclusions in regard to the possible role of TPW in perturbing the elevation of ancient sea-level markers. Perron et al. [2007] examined long, continuous topographic benches, or contacts, that had been interpreted (somewhat controversially) as putative shorelines. They concluded that a post-depositional TPW event, characterised by a pole path consistent with dynamic constraints imposed by the location of the Tharsis volcanic province, explains the long-wavelength topography observed along the strike of these contacts. In contrast, di Achille & Hynek [2010] analysed the elevations of ancient deltaic deposits and concluded that they lie close to a present-day equipotential. They concluded that these markers of an ancient ocean have been subject to little post-depositional deflection. Chapter 6 showed, using valley-network termini as possible markers of ancient sea level, that the present-day topography of these features suggests a TPW event of $\sim 10^{\circ}$ after the (Noachian-age) valley networks formed, along a path consistent with the geometry inferred by Perron et al. [2007]. A number of aspects of this study would benefit from further analysis, and we leave these issues for future work.

A

Inversion of Liouville Equation

The Revised Theory

Adopting a parallel approach to Wu & Peltier [1984] (for direct comparison), we start by substituting equations (4.6) and (4.3) into (4.1), giving

$$\mathbf{m}(s) = \frac{\mathbf{I}^L(s)}{C-A} \frac{l_s(\mathrm{LT}) - s\displaystyle\sum_{k=1}^{K} \frac{r'_k/s_k}{s+s_k}}{1 - \dfrac{k_2^T(s=0;\mathrm{LT}) - s\sum_{k=1}^{K} \frac{r''_k/s_k}{s+s_k}}{k_f}}. \tag{A.1}$$

If we define

$$g_k \equiv \frac{\dfrac{r''_k}{s_k}}{\displaystyle\sum_{k=1}^{K} \frac{r''_k}{s_k}}, \tag{A.2}$$

then

$$\sum_{k=1}^{K} \frac{r''_k/s_k}{s+s_k} = \left[\sum_{\mathcal{K}=1}^{K} \frac{r''_{\mathcal{K}}}{s_{\mathcal{K}}}\right] \cdot \sum_{k=1}^{K} \frac{g_k}{s+s_k}.$$

Substitution into equation (A.1) gives

$$\mathbf{m}(s) = \frac{\mathbf{I}^L(s)}{C-A} \frac{l_s(\mathrm{LT}) - s\sum_{k=1}^{K} \frac{r'_k/s_k}{s+s_k}}{1 - \frac{k_2^T(s=0;\mathrm{LT}) - s\left[\sum_{\mathcal{K}=1}^{K} r''_{\mathcal{K}}/s_{\mathcal{K}}\right]\sum_{k=1}^{K} g_k/(s+s_k)}{k_f}}. \tag{A.3}$$

Now, we also define the Chandler wobble frequency (of a deformable, stratified planet)

$$\sigma_0 \equiv \frac{k_2^T(s=0;\mathrm{LT}) - k_2^{T,E}}{k_2^T(s=0;\mathrm{LT})}\sigma_r\,, \tag{A.4}$$

where

$$\sigma_r = \frac{C-A}{A}\Omega\,, \tag{A.5}$$

in which Ω is the angular velocity of the planet's rotation. Using equation (4.5) in (A.4), we can write

$$\sum_{k=1}^{K} \frac{r''_k}{s_k} = k_2^T(s=0;\mathrm{LT})\frac{\sigma_0}{\sigma_r}\,.$$

Substituting the above expression into equation (A.3) gives

$$\mathbf{m}(s) = \frac{\mathbf{I}^L(s)}{C-A} \frac{l_s(\mathrm{LT}) - s\sum_{k=1}^{K} \frac{r'_k/s_k}{s+s_k}}{1 - \frac{k_2^T(s=0;\mathrm{LT})\left[1 - \frac{\sigma_0}{\sigma_r} s\sum_{k=1}^{K} g_k/(s+s_k)\right]}{k_f}}\,. \tag{A.6}$$

We henceforth proceed under the excess ellipticity assumption (4.12). After some algebra, equation (A.6) becomes

$$\mathbf{m}(s) = \frac{\Omega}{A\sigma_0}\mathbf{I}^L(s) \frac{l_s(\mathrm{LT}) - s\sum_{k=1}^{K} \frac{r'_k/s_k}{s+s_k}}{\frac{k_2^T(s=0;\mathrm{LT})}{\sum_{k=1}^{K}\frac{r''_k}{s_k}}\varepsilon(\mathrm{LT}) + [1-\varepsilon(\mathrm{LT})]\, s\sum_{k=1}^{K}\frac{g_k}{s+s_k}}\,, \tag{A.7}$$

where we have used equation (4.11) to simplify the expression. Mimicking Wu & Peltier [1984], we define a polynomial

$$Q_{K-1}(s) = \prod_{i=1}^{K-1}(s+\lambda_i)\ ,$$

where the subscript of $K-1$ indicates the degree of $Q(s)$. Then, we can rewrite the summation

$$\sum_{k=1}^{K}\frac{g_k}{s+s_k} = \frac{\displaystyle\sum_{k=1}^{K} g_k \prod_{\substack{i=1\\ i\neq k}}^{K}(s+s_i)}{\displaystyle\prod_{i=1}^{K}(s+s_i)} = \frac{Q_{K-1}(s)}{\displaystyle\prod_{i=1}^{K}(s+s_i)}\ .$$

Now, equation (A.7) becomes

$$\mathbf{m}(s) = \frac{\Omega}{A\sigma_0}\mathbf{I}^L(s)\frac{l_s(\mathrm{LT})\displaystyle\prod_{i=1}^{K}(s+s_i) - s\sum_{k=1}^{K}\frac{r'_k}{s_k}\prod_{\substack{i=1\\ i\neq k}}^{K}(s+s_i)}{\varepsilon(\mathrm{LT})\dfrac{k_2^T(s=0;\mathrm{LT})}{\sum_{k=1}^{K}\frac{r''_k}{s_k}}\displaystyle\prod_{i=1}^{K}(s+s_i) + [1-\varepsilon(\mathrm{LT})]\,s\,Q_{K-1}(s)}\ . \tag{A.8}$$

Rewriting the denominator of the right-hand-most fraction in equation (A.8) as a polynomial of s would be helpful:

$$\prod_{i=1}^{K}(s+\kappa_i) = \frac{\varepsilon(\mathrm{LT})\dfrac{k_2^T(s=0;\mathrm{LT})}{\sum_{k=1}^{K}\frac{r''_k}{s_k}}\displaystyle\prod_{i=1}^{K}(s+s_i) + [1-\varepsilon(\mathrm{LT})]\,s\,Q_{K-1}(s)}{1-\varepsilon(\mathrm{LT})+\varepsilon(\mathrm{LT})\dfrac{k_2^T(s=0;\mathrm{LT})}{\sum_{k=1}^{K}\frac{r''_k}{s_k}}}$$

(Note that the scaling is such that the leading degree term has a coefficient of unity.) Therefore,

equation (A.8) becomes

$$\mathbf{m}(s) = \frac{\Omega}{A\sigma_0}\mathbf{I}^L(s)\left[\frac{l_s(\mathrm{LT})}{1-\varepsilon(\mathrm{LT})+\varepsilon(\mathrm{LT})\dfrac{k_2^T(s=0;\mathrm{LT})}{\sum_{k=1}^{K}\frac{r_k''}{s_k}}}\frac{\prod_{i=1}^{K}(s+s_i)}{\prod_{i=1}^{K}(s+\kappa_i)}\right.$$
$$\left.-\frac{s\sum_{k=1}^{K}\dfrac{r_k'}{s_k}}{1-\varepsilon(\mathrm{LT})+\varepsilon(\mathrm{LT})\dfrac{k_2^T(s=0;\mathrm{LT})}{\sum_{k=1}^{K}\frac{r_k''}{s_k}}}\frac{\prod_{\substack{i=1\\i\neq k}}^{K}(s+s_i)}{\prod_{i=1}^{K}(s+\kappa_i)}\right] . \quad \text{(A.9)}$$

This expression cannot be easily inverted, since both numerator and denominator have the same degree in s (which is K). To recast equation (A.9) such that its numerator contains only polynomials with degree $K-1$, we further define a pair of polynomials

$$q'(s) \equiv \prod_{i=1}^{K}(s+\kappa_i) - \prod_{i=1}^{K}(s+s_i) , \quad \text{(A.10)}$$

and

$$R_k'(s) \equiv \prod_{i=1}^{K}(s+\kappa_i) - s\prod_{\substack{i=1\\i\neq k}}^{K}(s+s_i) . \quad \text{(A.11)}$$

Then, we can rewrite the ratio of products in equation (A.9) as

$$\frac{\prod_{i=1}^{K}(s+s_i)}{\prod_{i=1}^{K}(s+\kappa_i)} = 1 - \frac{q'(s)}{\prod_{i=1}^{K}(s+\kappa_i)} , \quad \text{(A.12)}$$

and

$$\frac{s\prod_{\substack{i=1\\i\neq k}}^{K}(s+s_i)}{\prod_{i=1}^{K}(s+\kappa_i)} = 1 - \frac{R_k'(s)}{\prod_{i=1}^{K}(s+\kappa_i)} . \quad \text{(A.13)}$$

Liouville equation (A.9) now becomes

$$\mathbf{m}(s) = \frac{\Omega}{A\sigma_0} \frac{\mathbf{I}^L(s)}{1-\varepsilon(\mathrm{LT})+\varepsilon(\mathrm{LT})\dfrac{k_2^T(s=0;\mathrm{LT})}{\sum_{k=1}^{K}\frac{r_k''}{s_k}}} \left\{ l_s(\mathrm{LT}) \left[1 - \frac{q'(s)}{\prod_{i=1}^{K}(s+\kappa_i)} \right] - \sum_{k=1}^{K} \frac{r_k'}{s_k} \left[1 - \frac{R_k'(s)}{\prod_{i=1}^{K}(s+\kappa_i)} \right] \right\}, \quad \text{(A.14)}$$

which is ready to be inverted.

Using standard tables for Laplace transformations, we invert the terms inside the curly brackets in equation (A.14) as follows:

$$\mathscr{L}^{-1}\left\{ l_s(\mathrm{LT}) \left[1 - \frac{q'(s)}{\prod_{i=1}^{K}(s+\kappa_i)} \right] \right\} = l_s(\mathrm{LT})\delta(t) + l_s(\mathrm{LT}) \sum_{k=1}^{K} \frac{\prod_{i=1}^{K}(s_i-\kappa_k)}{\prod_{\substack{i=1 \\ i\neq k}}^{K}(\kappa_i-\kappa_k)} e^{-\kappa_k t},$$

and

$$\mathscr{L}^{-1}\left\{ -\sum_{k=1}^{K} \frac{r_k'}{s_k} \left[1 - \frac{R_k'(s)}{\prod_{i=1}^{K}(s+\kappa_i)} \right] \right\} = -\sum_{k=1}^{K} \frac{r_k'}{s_k}\delta(t) + \sum_{j=1}^{K} \frac{r_j'}{s_j} \sum_{k=1}^{K} \frac{\kappa_k \prod_{\substack{i=1 \\ i\neq j}}^{K}(s_i-\kappa_k)}{\prod_{\substack{i=1 \\ i\neq k}}^{K}(\kappa_i-\kappa_k)} e^{-\kappa_k t}.$$

Collecting like terms, we have

$$\left[l_s(\mathrm{LT}) - \sum_{k=1}^{K} \frac{r_k'}{s_k} \right] \delta(t) = D_1\delta(t),$$

where we have used the definition (4.8), and

$$\sum_{k=1}^{K}\left[l_s(\mathrm{LT})\frac{\prod_{i=1}^{K}(s_i-\kappa_k)}{\prod_{\substack{i=1\\i\neq k}}^{K}(\kappa_i-\kappa_k)}+\sum_{j=1}^{K}\frac{r'_j}{s_j}\frac{\kappa_k\prod_{\substack{i=1\\i\neq j}}^{K}(s_i-\kappa_k)}{\prod_{\substack{i=1\\i\neq k}}^{K}(\kappa_i-\kappa_k)}\right]e^{-\kappa_k t}=\sum_{k=1}^{K}E'_k e^{-\kappa_k t},$$

where we have used the definition (4.14).

As a final step, we note that

$$\mathscr{L}^{-1}\left\{\mathbf{I}^L(s)f(s)\right\}=\mathbf{I}^L(t)*\mathcal{F}(t)$$

for a Laplace-domain function, $f(s)$, and its corresponding time-domain form, $\mathcal{F}(t)$.

Applying this to our results above, we arrive at equation (4.13):

$$\mathbf{m}(t)=\frac{\Omega}{A\sigma_0}\frac{1}{1-\varepsilon(\mathrm{LT})+\varepsilon(\mathrm{LT})\frac{k_2^T(s=0;\mathrm{LT})}{\sum_{k=1}^{K}\frac{r''_k}{s_k}}}\left[\mathbf{I}(t)D_1+\sum_{k=1}^{K}E'_k\left(\mathbf{I}(t)*e^{-\kappa_k t}\right)\right],\qquad(A.15)$$

which is the time domain form of Liouville equation under the excess ellipticity assumption.

Bibliography

Aster, R. C., Thurber, C. H., & Borchers, B., 2005. *Parameter Estimation and Inverse Problems*, Elsevier Academic Press, Boston.

Besse, J. & Courtillot, V., 2002. Apparent and true polar wander and the geometry of the geomagnetic field over the last 200 Myr, *J. Geophys. Res. Solid Earth*, **107**, 2300.

Bills, B. G. & James, T. S., 1999. Moments of inertia and rotational stability of Mars: Lithospheric support of subhydrostatic rotational flattening, *J. Geophys. Res*, **104**, 9081–9096.

Breuer, D. & Spohn, T., 2006. Viscosity of the Martian mantle and its initial temperature: Constraints from crust formation history and the evolution of the magnetic field, *Planetary and Space Science*, **54**, 153–169.

Cambiotti, G., Ricard, Y., & Sabadini, R., 2010. Ice age True Polar Wander in a compressible and non-hydrostatic Earth, *Geophys. J. Int.*, **183**, 1248–1264.

Cambiotti, G., Ricard, Y., & Sabadini, R., 2011. New insights into mantle convection true polar wander and rotational bulge readjustment, *Earth Planet. Sci. Lett.*, **310**, 538–543.

Carr, M. H., 1995. The Martain drainage system and the origin of valley networks and fretted channels, *J. Geophys. Res*, **100**, 7479–7507.

Chambat, F., Ricard, Y., & Valette, B., 2010. Flattening of the Earth: further from hydrostaticity than previously estimated, *Geophys. J. Int.*, **183**, 727–732.

Chan, N.-H., Mitrovica, J. X., Matsuyama, I., Creveling, J. R., & Stanley, S., 2011a. The rotational stability of a convecting earth: assessing inferences of rapid TPW in the late cretaceous, *Geophys. J. Int.*, **187**, 1319–1333.

Chan, N.-H., Mitrovica, J. X., Matsuyama, I., Latychev, K., Creveling, J. R., Stanley, S., & Morrow, E., 2011b. The rotational stability of a convecting Earth: the Earth's figure and TPW over the last 100 Myr, *Geophys. J. Int.*, **187**, 773–782.

Chan, N.-H., Mitrovica, J. X., Daradich, A., Creveling, J. R., Matsuyama, I., & Stanley, S., 2014. Time-dependent rotational stability of dynamic planets with elastic lithospheres, *J. Geophys. Res. Planets*, **119**, 169–188.

Clifford, S. M. & Parker, T. J., 2001. The Evolution of the Martian Hydrosphere: Implications for the Fate of a Primordial Ocean and the Current State of the Northern Plains, *Icarus*, **154**, 40–79.

Cottrell, R. D. & Tarduno, J. A., 2000. Late Cretaceous True Polar Wander: Not So Fast, *Science*, **288**, 2283–2283.

Creveling, J. R., Mitrovica, J. X., Chan, N.-H., Latychev, K., & Matsuyama, I., 2012. Mechanisms for oscillatory true polar wander, *Nature*, **491**, 244–248.

Dahlen, F. A., 1976. The Passive Influence of the Oceans upon the Rotation of the Earth, *Geophy. J. R. astr. Soc.*, **46**, 363–406.

Daradich, A., 2007. *Dynamic topography of continents and rotational stability of planets with lithospheres*, Ph.D. Thesis, University of Toronto.

Daradich, A., Mitrovica, J. X., Matsuyama, I., & Perron, J. T., 2008. Equilibrium rotational stability and figure of Mars, *Icarus*, **194**, 463–475.

de Boer, B., van de Wal, R. S. W., Bintanja, R., Lourens, L. J., & Tuenter, E., 2010. Cenozoic global ice-volume and temperature simulations with 1-D ice-sheet models forced by benthic δ^{18}O records, in *Annals of Glaciology*, 23–33.

di Achille, G. & Hynek, B. M., 2010. Ancient ocean on Mars supported by global distribution of deltas and valleys, *Nature Geoscience*, **3**, 459–463.

Dziewonski, A. M. & Anderson, D. L., 1981. Preliminary Reference Earth Model, *Phys. Earth planet. Inter.*, **25**, 297–356.

Erkeling, G., Reiss, D., Hiesinger, H., Poulet, F., Carter, J., Ivanov, M. A., Hauber, E., & Jaumann, R., 2012. Valleys, paleolakes and possible shorelines at the Libya Montes/Isidis boundary: Implications for the hydrologic evolution of Mars, *Icarus*, **219**, 393–413.

Evans, D. A., 1998. True polar wander, a supercontinental legacy, *Earth Planet. Sci. Lett.*, **157**, 1–8.

Fairén, A. G., 2010. A cold and wet Mars, *Icarus*, **208**, 165–175.

Fassett, C. I. & Head, III, J. W., 2008. Valley network-fed, open-basin lakes on Mars: Distribution and implications for Noachian surface and subsurface hydrology, *Icarus*, **198**, 37–56.

Fassett, C. I., Dickson, J. L., Head, J. W., Levy, J. S., & Marchant, D. R., 2010. Supraglacial and proglacial valleys on Amazonian Mars, *Icarus*, **208**, 86–100.

Forte, A. M. & Mitrovica, J. X., 1997. A resonance in the Earth's obliquity and precession overthe past 20 Myr driven by mantle convection, *Nature*, **390**, 676–680.

Forte, A. M. & Mitrovica, J. X., 2001. Deep-mantle high-viscosity ow and thermochemical structure inferred from seismic and geodynamic data, *Nature*, **410**, 1049–1056.

Ghatan, G. J. & Zimbelman, J. R., 2006. Paucity of candidate coastal constructional landforms along proposed shorelines on Mars: Implications for a northern lowlands-filling ocean, *Icarus*, **185**, 171–196.

Gold, T., 1955. Instability of the Earth's axis of rotation, *Nature*, **175**, 526–529.

Goldreich, P. & Toomre, A., 1969. Some remarks on polar wandering., *J. Geophys. Res*, **74**, 2555–2567.

Greff-Lefftz, M., 2004. Upwelling plumes, superswells and true polar wander, *Geophys. J. Int.*, **159**, 1125–1137.

Gross, R. S., 2000. the excitation of the Chandler wobble, *Geophys. Res. Lett*, **27**, 2329–2332.

Gross, R. S., 2007. Earth Rotation Variations - Long Period, *Treatise on geophysics*, **3**, 239–294.

Hauck, S. A. & Phillips, R. J., 2002. Thermal and crustal evolution of Mars, *J. Geophys. Res. Planets*, **107**, 5052–5070.

Hobley, D. E. J., Howard, A. D., & Moore, J. M., 2014. Fresh shallow valleys in the Martian midlatitudes as features formed by meltwater flow beneath ice, *J. Geophys. Res. Planets*, **119**, 128–153.

Hood, L. L., Young, C. N., Richmond, N. C., & Harrison, K. P., 2005. Modeling of major martian magnetic anomalies: Further evidence for polar reorientations during the Noachian, *Icarus*, **177**, 144–173.

Hynek, B. M. & Phillips, R. J., 2003. New data reveal mature, integrated drainage systems on Mars indicative of past precipitation, *Geology*, **31**, 757–760.

Hynek, B. M., Beach, M., & Hoke, M. R. T., 2010. Updated global map of Martian valley networks and implications for climate and hydrologic processes, *J. Geophys. Res*, **115**, E09008.

James, T. S. & Ivins, E. R., 1997. Global geodetic signatures of the Antarctic Ice Sheet, *J. Geophys. Res. Solid Earth*, **102**, 605–633.

Johnston, P. & Lambeck, K., 1999. Postglacial rebound and sea level contributions to changes in the geoid and the Earth's rotation axis, *Geophys. J. Int.*, **136**, 537–558.

Kirschvink, J. L., Ripperdan, R. L., & Evans, D. A., 1997. Evidence for a large-scale reorganization of Early Cambrian continental masses by inertial interchange true polar wander, *Science*, **277**, 541–545.

Lambeck, K., 1980. *The Earth's Variable Rotation: Geophysical Causes and Consequences*, Cambridge University Press, London.

Lambeck, K., Smither, C., & Johnston, P., 1998. Sea-level change, glacial rebound and mantle viscosity fornorthern Europe, *Geophys. J. Int.*, **134**, 102–144.

Latychev, K., Mitrovica, J. X., Tromp, J., Tamisiea, M. E., Komatitsch, D., & Christara, C. C., 2005. Glacial isostatic adjustment on 3-D Earth models: a finite-volume formulation, *Geophys. J. Int.*, **161**, 421–444.

Lefftz, M., 1991. *Aspects théoriques de la rotation de la Terre et de son noyau: influence de la viscosité*, Ph.D. thesis, University of Strasbourg.

Leverington, D. W., 2011. A volcanic origin for the outflow channels of Mars: Key evidence and major implications, *Geomorphology*, **132**, 51–75.

Lewis, K. W., Aharonson, O., Grotzinger, J. P., Kirk, R. L., McEwen, A. S., & Suer, T.-A., 2008. Quasi-Periodic Bedding in the Sedimentary Rock Record of Mars, *Science*, **322**, 1532–1535.

Lithgow-Bertelloni, C. & Silver, P. G., 1998. Dynamic topography, plate driving forces and the African superswell, *Nature*, **395**, 269–272.

Malin, M. C. & Edgett, K. S., 2000. Sedimentary Rocks of Early Mars, *Science*, **290**, 1927–1937.

Maloof, A. C., Halverson, G. P., Kirschvink, J. L., Schrag, D. P., Weiss, B. P., & Hoffman, P. F., 2006. Combined paleomagnetic, isotopic, and stratigraphic evidence for true polar wander from the Neoproterozoic Akademikerbreen Group, Svalbard, Norway, *Geological Society of America Bulletin*, **118**, 1099–1124.

Matsubara, Y., Howard, A. D., & Gochenour, J. P., 2013. Hydrology of early Mars: Valley network incision, *J. Geophys. Res. Planets*, **118**, 1365–1387.

Matsuyama, I. & Manga, M., 2010. Mars without the equilibrium rotational figure, Tharsis, and the remnant rotational figure, *J. Geophys. Res*, **115**, E12020.

Matsuyama, I. & Nimmo, F., 2011. Reorientation of Vesta: Gravity and tectonic predictions, *Geophys. Res. Lett*, **38**, L14205.

Matsuyama, I., Mitrovica, J. X., Manga, M., Perron, J. T., & Richards, M. A., 2006. Rotational stability of dynamic planets with elastic lithospheres, *J. Geophys. Res*, **111**, E02003.

Matsuyama, I., Mitrovica, J. X., Daradich, A., & Gomez, N., 2010. The rotational stability of a triaxial ice-age Earth, *J. Geophys. Res. Solid Earth*, **115**, B05401.

Matsuyama, I., Nimmo, F., & Mitrovica, J. X., 2014. Planetary Reorientation, *Annu. Rev. Earth planet. Sci.*, **42**, 605–634.

Melosh, H. J., 1980. Tectonic patterns on a reoriented planet - Mars, *Icarus*, **44**, 745–751.

Mitrovica, J. X., 1996. Haskell [1935] revisited, *J. Geophys. Res. Solid Earth*, **101**, 555–569.

Mitrovica, J. X. & Forte, A. M., 2004. A new inference of mantle viscosity based upon joint inversion of convection and glacial isostatic adjustment data, *Earth Planet. Sci. Lett.*, **225**, 177–189.

Mitrovica, J. X. & Milne, G. A., 1998. Glaciation-induced perturbations in the Earth's rotation: a new appraisal, *J. Geophys. Res. Solid Earth*, **103**, 985–1005.

Mitrovica, J. X. & Wahr, J. M., 2011. Ice Age Earth Rotation, *Annu. Rev. Earth planet. Sci.*, **39**, 577–616.

Mitrovica, J. X., Milne, G. A., & Davis, J. L., 2001. Glacial isostatic adjustment on a rotating earth, *Geophys. J. Int.*, **147**, 562–578.

Mitrovica, J. X., Wahr, J. M., Matsuyama, I., & Paulson, A., 2005. The rotational stability of an ice-age Earth, *Geophys. J. Int.*, **161**, 491–506.

Mitrovica, J. X., Wahr, J. M., Matsuyama, I., & Paulson, A., 2006. Reanalysis of ancient eclipse, astronomic and geodetic data: A possible route to resolving the enigma of global sea-level rise, *Earth Planet. Sci. Lett.*, **243**, 390–399.

Morrow, E., Mitrovica, J. X., Forte, A. M., Glišović, P., & Huybers, P., 2012. An enigma in estimates of the Earth's dynamic ellipticity, *Geophys. J. Int.*, **191**, 1129–1134.

Moscardelli, L., 2014. Boulders of the Vastitas Borealis Formation: Potential origin and implications for an ancient martian ocean, *GSA Today*, **24**, 4–10.

Mound, J. E. & Mitrovica, J. X., 1998. True polar wander as a mechanism for second-order sea-level variations, *Science*, **279**, 534–537.

Munk, W., 2002. Twentieth century sea level: An enigma, *Proceedings of the National Academy of Science*, **99**, 6550–6555.

Munk, W. H. & MacDonald, G. J. F., 1960. *The rotation of the Earth: A geophysical discussion*, Cambridge University Press, New York.

Nakada, M., 2002. Polar wander caused by the Quaternary glacial cycles and fluid Love number, *Earth Planet. Sci. Lett.*, **200**, 159–166.

Nakada, M. & Lambeck, K., 1989. Late Pleistocene and Holocene sea-level change in the Australian region and mantle rheology, *Geophys. J. Int.*, **96**, 497–517.

Nakiboglu, S. M., 1982. Hydrostatic theory of the Earth and its mechanical implications, *Phys. Earth planet. Inter.*, **28**, 302–311.

Parker, T. J., Saunders, R. S., & Schneeberger, D. M., 1989. Transitional morphology in west Deuteronilus Mensae, Mars - Implications for modification of the lowland/upland boundary, *Icarus*, **82**, 111–145.

Parker, T. J., Gorsline, D. S., Saunders, R. S., Pieri, D. C., & Schneeberger, D. M., 1993. Coastal geomorphology of the Martian northern plains, *J. Geophys. Res*, **98**, 11061–11078.

Peltier, W. R., 1974. The impulse response of a Maxwell Earth, *Reviews of Geophysics and Space Physics*, **12**, 649–669.

Peltier, W. R., 1976. Glacial-isostatic adjustment—II. The inverse problem, *Geophy. J. R. astr. Soc.*, **46**, 669–705.

Peltier, W. R., 2004. Global Glacial Isostasy and the Surface of the Ice-Age Earth: The ICE-5G (VM2) Model and GRACE, *Annu. Rev. Earth planet. Sci.*, **32**, 111–149.

Perron, J. T., Mitrovica, J. X., Manga, M., Matsuyama, I., & Richards, M. A., 2007. Evidence for an ancient martian ocean in the topography of deformed shorelines, *Nature*, **447**, 840–843.

Phillips, R. J., Zuber, M. T., Solomon, S. C., Golombek, M. P., Jakosky, B. M., Banerdt, W. B., Smith, D. E., Williams, R. M. E., Hynek, B. M., Aharonson, O., & Hauck, II, S. A., 2001. Ancient Geodynamics and Global-Scale Hydrology on Mars, *Science*, **291**, 2587–2591.

Raymo, M. E., Mitrovica, J. X., O'Leary, M. J., Deconto, R. M., & Hearty, P. J., 2011. Departures from eustasy in Pliocene sea-level records, *Nature Geoscience*, **4**, 328–332.

Ricard, Y., Spada, G., & Sabadini, R., 1993. Polar wandering of a dynamic earth, *Geophys. J. Int.*, **113**, 284–298.

Richards, M. A., Ricard, Y., Lithgow-Bertelloni, C., Spada, G., & Sabadini, R., 1997. An explanation for Earth's long-term rotational stability, *Science*, **275**, 372–375.

Richards, M. A., Bunge, H.-P., Ricard, Y., & Baumgardner, J. R., 1999. Polar wandering in mantle convection models, *Geophys. Res. Lett*, **26**, 1777–1780.

Rouby, H., Greff-Lefftz, M., & Besse, J., 2010. Mantle dynamics, geoid, inertia and TPW since 120 Myr, *Earth Planet. Sci. Lett.*, **292**, 301–311.

Sabadini, R. & Peltier, W. R., 1981. Pleistocene deglaciation and the Earth's rotation: implications for mantle viscosity, *Geophysical Journal of the Royal Astronomical Society*, **66**, 553–578.

Sabadini, R., Yuen, D. A., & Boschi, E., 1982. Interaction of cryospheric forcings with rotational dynamics has consequences for ice ages, *Nature*, **296**, 338–341.

Sabadini, R., Yuen, D. A., & Boschi, E., 1983. Dynamic effects from mantle phase transitions on true polar wander during ice ages, *Nature*, **303**, 694–696.

Sager, W. W. & Koppers, A. A. P., 2000. Late Cretaceous Polar Wander of the Pacific Plate: Evidence of a Rapid True Polar Wander Event, *Science*, **287**, 455–459.

Schaber, K., Bunge, H.-P., Schuberth, B. S. A., Malservisi, R., & Horbach, A., 2009. Stability of the rotation axis in high-resolution mantle circulation models: Weak polar wander despite strong core heating, *Geochem. Geophys. Geosyst.*, **10**, Q11W04.

Schenk, P., Matsuyama, I., & Nimmo, F., 2008. True polar wander on Europa from global-scale small-circle depressions, *Nature*, **453**, 368–371.

Schultz, P. H. & Lutz, A. B., 1988. Polar wandering of Mars, *Icarus*, **73**, 91–141.

Simmons, N. A., Forte, A. M., & Grand, S. P., 2009. Joint seismic, geodynamic and mineral physical constraints on three-dimensional mantle heterogeneity: Implications for the relative importance of thermal versus compositional heterogeneity, *Geophys. J. Int.*, **177**, 1284–1304.

Skinner, Jr., J. A., Hare, T. M., & Tanaka, K. L., 2006. Digital Renovation of the Atlas of Mars 1:15,000,000-Scale Global Geologic Series Maps, in *37th Annual Lunar and Planetary Science Conference*, no. 2331.

Smith, D. E., Sjogren, W. L., Tyler, G. L., Balmino, G., Lemoine, F. G., & Konopliv, A. S., 1999. The Gravity Field of Mars: Results from Mars Global Surveyor, *Science*, **286**, 94–97.

Smith, D. E., Zuber, M. T., Neumann, G. A., Guinness, E. A., & Slavney, S., 2003. Mars Global Surveyor Laser Altimeter Mission Experiment Gridded Data Record, *NASA Planetary Data System*, MGS-M-MOLA-5-MEGDR-L3-V1.0.

Smith, M. L., 1977. Wobble and nutation of the earth., *Geophys. J. Int.*, **50**, 103–140.

Sohl, F. & Spohn, T., 1997. The interior structure of Mars: Implications from SNC meteorites, *J. Geophys. Res. Planets*, **102**, 1613–1635.

Steinberger, B. & O'Connell, R. J., 1997. Changes of the Earth's rotation axis owing to advection of mantle density heterogeneities, *Nature*, **387**, 169–173.

Steinberger, B. & O'Connell, R. J., 2002. The convective mantle flow signal in rates of true polar wander, *Ice Sheets, Sea Level and the Dynamic Earth, Geodynamics Series 29*, pp. 233–256, American Geophysical Union, Washington, D.C.

Steinberger, B. & Torsvik, T. H., 2008. Absolute plate motions and true polar wander in the absence of hotspot tracks, *Nature*, **452**, 620–624.

Steinberger, B. & Torsvik, T. H., 2010. Toward an explanation for the present and past locations of the poles, *Geochem. Geophys. Geosyst.*, **11**, Q06W06.

Thissen, C., Mitchell, R. N., Kirschvink, J. L., Evans, D. A., Montanari, A., Coccioni, R., Hinnov, L. A., & Tsai, V. C., 2010. True Polar Wobbles: Cretaceous Magnetostratigraphy Provides Continuous Age-Calibration and Paleogeography, in *American Geophysical Union, Fall Meeting 2010*, no. GP13A-0758.

Torsvik, T. H., Burke, K., Steinberger, B., Webb, S. J., & Ashwal, L. D., 2010. Diamonds sampled by plumes from the core-mantle boundary, *Nature*, **466**, 352–355.

Tosi, N., Sabadini, R., Marotta, A. M., & Vermeersen, L. L. A., 2005. Simultaneous inversion for the Earth's mantle viscosity and ice mass imbalance in Antarctica and Greenland, *J. Geophys. Res. Solid Earth*, **110**, B07402.

Tromp, J. & Mitrovica, J. X., 1999. Surface loading of a viscoelastic earth—I. General theory, *Geophys. J. Int.*, **137**, 847–855.

Tsai, V. C. & Stevenson, D. J., 2007. Theoretical constraints on true polar wander, *J. Geophys. Res*, **112**, B05415.

Tushingham, A. M. & Peltier, W. R., 1991. Ice-3G: a new global model of Late Pleistocene deglaciation based upon geophysical predictions of post-glacial relative sea level change, *J. Geophys. Res*, **96**, 4497–4523.

Vermeersen, L. L. A., Fournier, A., & Sabadini, R., 1997. Changes in rotation induced by Pleistocene ice masses with stratified analytical Earth models, *J. Geophys. Res*, **102**, 27689–27702.

Wahr, J. M., 1982. The effects of the atmosphere and oceans on the earth's wobble. - I. Theory., *Geophys. J. Int.*, **70**, 349–372.

Watts, A. B., 2001. *Isostasy and Flexure of the Lithosphere*, Cambridge University Press, New York.

Willemann, R. J., 1984. Reorientation of planets with elastic lithospheres, *Icarus*, **60**, 701–709.

Williams, J.-P. & Nimmo, F., 2004. Thermal evolution of the Martian core: Implications for an early dynamo, *Geology*, **32**, 97–100.

Wordsworth, R., Forget, F., Millour, E., Head, J. W., Madeleine, J. B., & Charnay, B., 2013. Global modelling of the early martian climate under a denser CO2 atmosphere: Water cycle and ice evolution, *Icarus*, **222**, 1–19.

Wu, P., 1978. The response of a Maxwell Earth to applied surface mass loads, *M.Sc. Thesis*, University of Toronto.

Wu, P. & Peltier, W. R., 1984. Pleistocene deglaciation and the Earth's rotation: a new analysis, *Geophy. J. R. astr. Soc.*, **76**, 753–791.

Zhang, N., Zhong, S., Leng, W., & Li, Z.-X., 2010. A model for the evolution of the Earth's mantle structure since the Early Paleozoic, *J. Geophys. Res*, **115**, B06401.

Zharkov, V. & Gudkova, T., 2005. Construction of Martian interior model, *Solar Syst Res+*, **39**, 343–373.

Zuber, M. T. & Smith, D. E., 1997. Mars without Tharsis, *J. Geophys. Res*, **102**, 28673–28685.

Если жизнь тебя обманет,
Не печалься, не сердись!
В день уныния смирись:
День веселья, верь, настанет.

Сердце в будущем живет;
Настоящее уныло:
Все мгновенно, все пройдет;
Что пройдет, то будет мило.

Александр Пушкин (1825)

This thesis was typeset using LaTeX, originally developed by Leslie Lamport and based on Donald Knuth's TeX. The body text is set in 12 point TeX Gyre Termes, a loose decedent of the famous Times font. The above poem, without a title, was originally written in 1825 by Alexander Sergeyevich Pushkin (1799–1837). My translation, preserving the rhyme structure, reads: *If life were to cast you down, Don't be saddened, don't resent! On the day of gloom, relent: Believe, day of joy'll come around. In the future resides the heart; in the present, misery: All is fleeting, all will depart; That departure will be lovely.* A template that can be used to format a PhD thesis with this look and feel has been released under the permissive MIT (X11) license, and can be found online at github.com/suchow/Dissertate or from its author, Jordan Suchow, at suchow@post.harvard.edu.